STRUCTURAL STUDIES OF $[(PbSe)_{0.99}]_m[WSe_2]_n$, $[(PbSe)_{1.00}]_m[MoSe_2]_n$, AND $[(SnSe)_{1.03}]_m[MoSe_2]_n$ MISFIT LAYERED COMPOUNDS

by

MARY MAGADALENE SMELLER

A DISSERTATION

Presented to the Department of Chemistry
and the Graduate School of the University of Oregon
in partial fulfillment of the requirements
for the degree of
Doctor of Philosophy

June 2011

DISSERTATION APPROVAL PAGE

Student: Mary Magdalene Smeller

Title: Structural Studies of $[(PbSe)_{0.99}]_m[WSe_2]n$, $[(PbSe)_{1.00}]_m[MoSe_2]_n$, and $[(SnSe)_{1.03}]_m[MoSe_2]_n$ Misfit Layered Compounds

This dissertation has been accepted and approved in partial fulfillment of the requirements for the Doctor of Philosophy degree in the Department of Chemistry by:

Dr. Thomas R. Dyke, Ph.D.	Chairperson
Dr. David C. Johnson, Ph.D.	Advisor
Dr. Catherine J. Page, Ph.D.	Member
Dr. Andrew H. Marcus, Ph.D.	Member
Dr. John L. Hardwick, Ph.D.	Member
Dr. Richard Taylor, Ph.D.	Outside Member
And Richard Linton	Vice President for Research and Graduate Studies/Dean of the Graduate School

Original approval signatures are on file with the University of Oregon Graduate School.

Degree awarded June 2011

DISSERTATION ABSTRACT

Mary Magdalene Smeller

Doctor of Philosophy

Department of Chemistry

June 2011

Title: Structural Studies of $[(PbSe)_{0.99}]_m[WSe_2]_n$, $[(PbSe)_{1.00}]_m[MoSe_2]_n$, and $[(SnSe)_{1.03}]_m[MoSe_2]_n$ Misfit Layered Compounds

Approved: _____

Dr. David C. Johnson, Ph.D.

The structures of several compounds in the $[(PbSe)_{0.99}]_m[WSe_2]_n$, $[(PbSe)_{1.00}]_1[MoSe_2]_1$, and $[(SnSe)_{1.03}]_1[MoSe_2]_1$ systems were determined using x-ray data. The structural determination using Rietveld methods was complicated by the strong preferred orientation of the samples, which resulted in x-ray diffraction scans with either 00*l* or *hk*0 reflections depending on the orientation of the sample in the diffractometer.

Rietveld refinements of the $[(PbSe)_{0.99}]_1[WSe_2]_1$, $[(PbSe)_{1.00}]_1[MoSe_2]_1$, and $[(SnSe)_{1.03}]_1[MoSe_2]_1$ samples were compared to single crystal sample refinement results for $[(MX)_{1+\delta}]_1[TX_2]_1$, where M is a metal, T is a transition, X is a chalcogen, and δ is the misfit parameter. The structural refinement yielded rock salt layer puckering values of 25 pm, 23 pm, and 36 pm for $[(PbSe)_{0.99}]_1[WSe_2]_1$, $[(PbSe)_{1.00}]_1[MoSe_2]_1$, and $[(SnSe)_{1.03}]_1[MoSe_2]_1$, respectively, which are all within the established literature range of 20 pm to 60 pm. The refinement of the *hk*0 reflections confirmed that the in plane structures were consistent with the dichalcogenide ($P6_3mmc$) and rock salt ($Fm3m$) structure types.

Structures for the $[(PbSe)_{0.99}]_m[WSe_2]_m$ isomer series where m = 1 to 5 were determined, and a systematic trend in structure as a function of the thickness of the constituent layers was discovered. The structure of the rock salt constituent was found to distort into pairs, forming alternating long and short distances along the c axis. This distortion decreases as the number of rock salt planes increases from 4 to 6 to 8 and is either absent or nearly so in compounds with a larger number of rock salt planes. The puckering distortion at the interface between the rock salt and the dichalcogenide is also observed in the inner rock salt layers but decreases in magnitude moving away from the rock salt – dichalcogenide interface.

Structures of $[(PbSe)_{0.99}]_m[WSe_2]_n$ where m = 1 or 2 and n = 1 or 2 were also determined. The degree of structural distortion is a function of the ratio of rock salt to dichalcogenide layers.

This dissertation includes unpublished co-authored material.

CURRICULUM VITAE

NAME OF AUTHOR: Mary Magdalene Smeller

GRADUATE AND UNDERGRADUATE SCHOOLS ATTENDED:

University of Oregon, Eugene
Rosemont College, Bryn Mawr, PA

DEGREES AWARDED:

Doctor of Philosophy, Chemistry, 2011, University of Oregon
Master of Science, Chemistry, 2006, University of Oregon
Bachelor of Arts, Chemistry, 2001, Rosemont College
Bachelor of Arts, Mathematics, 2001, Rosemont College

AREAS OF SPECIAL INTEREST:

Rietveld refinement of turbostratically disordered compounds

PROFESSIONAL EXPERIENCE:

Chemistry Intern, Stevenson University, Stevenson, MD, Fall 2008
GK-12 Fellow, University of Oregon, 2005-2008
Graduate Teaching Fellow, Research Assistant, University of Oregon, 2004-2005
Graduate Teaching Fellow, Teaching Assistant, University of Oregon, 2003-2004
Laboratory Preparator, Organic Chemistry Teaching Lab, University of Pennsylvania, 2001-2003
Physical Science Aide, National Institute of Standards and Technology, Gaithersburg, MD, Summer and breaks 1997-1999

GRANTS, AWARDS, AND HONORS:

Fellow, GK-12 Science Outreach Program, University of Oregon, 2007
Fellow, GK-12 Science Outreach Program, University of Oregon, 2006
Fellow, GK-12 Science Outreach Program, University of Oregon, 2005
Graduate Teaching Fellow, University of Oregon, 2004
Graduate Teaching Fellow, University of Oregon, 2003

PUBLICATIONS:

Lin, Q.; Smeller, M.; Heideman, C. L.; Zschack, P.; Koyano, M.; Anderson, M. D.; Kykyneshi, R.; Keszler, D. A.; Anderson, I. M.; Johnson, D. C. Rational Synthesis and Characterization of a New Family of Low Thermal Conductivity Misfit Layer Compounds $[(PbSe)_{0.99}]_m(WSe_2)_n$. Chemistry of Materials 2010, 22, 1002-1009.

Zschack, P.; Heideman, C.; Mortensen, C.; Nguyen, N.; Smeller, M.; Lin, Q.; Johnson, D. C., X-Ray Characterization of Low-Thermal-Conductivity Thin-Film Materials. Journal of Electronic Materials 2009, 38(7), 1402-1406.

Kamunde, M., Johnson, D. C., Smeller, M., Li, S., Synthesis and characterization of $(Bi_2Te_3)_x(TiTe_2)_y$ superlattices. Abstracts of Papers, 231st ACS National Meeting, Atlanta, GA, United States, March 26-30, 2006, CHED-955.

Smeller, M. M., Harris, F. R. et al., "Synthesis of $(Bi_2Te_3)_x(TiTe_2)_x$ and $(Bi_2Te_3)_x(TiTe_2)_3$ superlattices." Materials Research Society Symposium Proceedings 886 (Materials and Technologies for Direct Thermal-to-Electric Energy Conversion) 2006, 91-96.

Smeller, M.M.; Harris, F.R.; Johnson, D.C., Repeatable synthesis of $(Bi_2Te_3)_5(TiTe_2)_4$ superlattices using modulated elemental reactants. International Conference on Thermoelectrics Proceedings, 2005, 24, 268-269.

Li, S.L.; Smeller, M.; Johnson, D.C., Attempted synthesis of $(Bi_2Te_3)_X$ $(SnTe)_Y$ misfit layer compounds. International Conference on Thermoelectrics Proceedings, 2005, 24, 299-300.

ACKNOWLEDGMENTS

I would like to thank my advisor, David Johnson, for agreeing to le me join his lab as well as his support and suggestions through the duration of this study. I would like to thank my committee for their wiliness to extend me the time necessary to complete this project as well as their belief that I could succeed. There were many people who contributed to the data and ideas in this work. Qiyin Lin, Colby Heideman, Ryan Atkins, Logan LaRossa, Paul Hansen, Johnathan Hanni, and Ryan Atkins provided the samples studied in this work. Qiyin Lin, Colby Heideman, Ryan Atkins, Mike Anderson, Clay Mortenson, Raimar Rostek, and Ngoc Nguyen took x-ray diffraction measurments on many of these samples. I would like to thank Dr. Paul Zschack and Dr. Evguenia Karapetrova for their help in using beamlines 33 and 34 at APS as well as many fruitful conversations about how to manipulate the raw data and understand the nuances of using a synchrotron to collect data. Dr. Brian H. Toby and Dr. Robert von Dreele provided valuable conversations about the functioning of the GSAS program. Sander van Smaalen helped me to understand how to refine the *hk*0 data. Dr. Arwyn Smalley, Dr. Fred Harris, and Dr. Angus Wilkinson established a way to refine 1-D x-ray diffraction data. Mike Anderson and Ian Anderson provided many inciteful STEM-HAADF pictures of these samples. Robert Kykyneshi and Dr. Douglas Kezsler completed modeling on the m = 1 to 5 system in order to help explain the unique results of that study.

I would also like to thank my friends and family for listening to me talk about my work as well as their wiliness to provide emotional support when I hit snags in my work. I would especially like to thank my husband for his patience with this process as well as his formatting help with this document.

To my husband, who has had an infinite amount of patience with me through this process.

TABLE OF CONTENTS

Chapter Page

Chapter Page

LIST OF FIGURES

Figure Page

LIST OF TABLES

CHAPTER I

INTRODUCTION

1.1: Misfit Layered Compounds

Misfit layered compounds (MLCs) have a unique structure that can be tuned to a wide range of physical properties. The minerals franckeite and cylindrite,[1] both sulfosalts, are naturally occurring MLCs. The existence of these minerals demonstrates the inherent stability of their structure. Structurally these compounds consist of a rock salt intercalated into a dichalcogenide. The structure of MLCs allows for a variety of physical properties depending on the component elements; these properties include superconductivity,[2-8] anisotropic magnetic properties,[7,8] or ultra-low thermal conductivity.[9] These properties are also susceptible to change via intercalation by another molecule, hydrazine, within the host structure.[10]

The general chemical formula for these compounds is $(MX_{1+\delta})_m(TX_2)_n$, where M is a transition or rare earth metal, X is a chalcogen, T is a group III, IV, V or VI transition metal, n and m are integers, and δ represents the magnitude of the misfit between the a and b parameters of the rock salt and dichalcogenide. The general structures of a rock salt and dichalcogenide are represented in Figure 1. When these two crystal types combine in an MLC they do so as a distorted rock salt composed of a bilayer of atoms and a dichalcogenide composed of a trilayer of atoms.

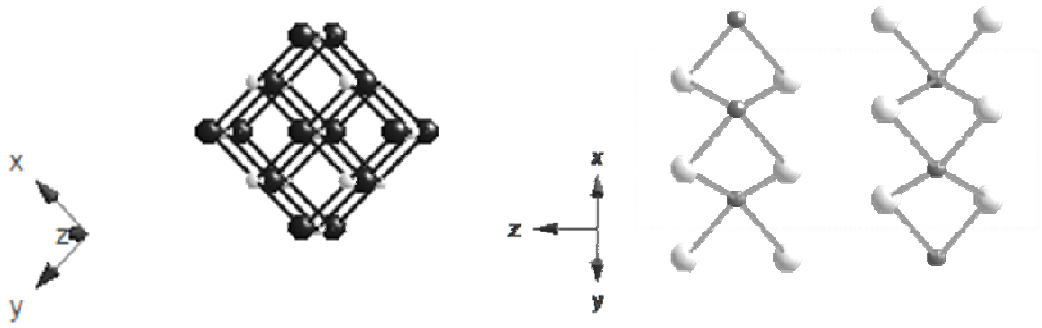

Figure 1: Representative bulk dichalcogenide and rock salt structures. The rock salt is on the left and the dichalcogenide on the right.

The misfit can be better understood by considering children's stacking blocks. If square blocks were stacked in one layer, rectangular on the next, then the repeated pattern will have the mismatch between the shape of the square and rectangular blocks. As seen in Figure 2, the tower would require more of the smaller blocks in order to provide structural stability to the stack. This compensating amount needed in a layer is represented by δ. The δ value is normally between 0.07 and 0.29.[10-16] Table 1 contains a list of some select compounds and their misfit parameters. The selenide based MLCs in these examples have nearly identical misfits compared to their

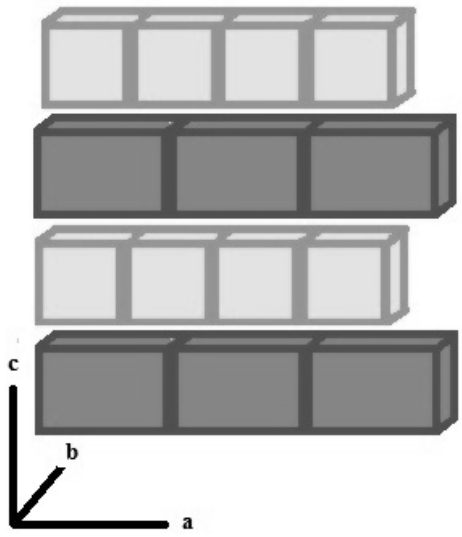

Figure 2: The stacking of MLCs as represented by children's blocks with the addition of unit cell parameters to clarify the analogy.

sulfide analogs. This implies that , the anions in the rock salt and the anions in the dichalcogenide must densely pack.

Table 1: Misfit parameters of a selection of compounds from literature

Compound	Delta	Reference
$(BiS)_{1.07}TaS_2$	0.07	[17]
$(BiS)_{1.08}TaS_2$	0.08	[18]
$(LaS)_{1.14}NbS_2$	0.14	[19]
$(LaS)_{1.14}NbS_2$	0.14	[18]
$(LaSe)_{1.14}(NbSe_2)_2$	0.14	[5]
$(PbS)_{1.14}NbS_2$	0.14	[19]
$(PbS)_{1.14}NbS_2$	0.14	[6]
$(PbS)_{1.14}NbS_2$	0.14	[18]
$(PbSe)_{1.14}(NbSe_2)_2$	0.14	[6]
$(PbSe)_{1.14}(NbSe_2)_3$	0.14	[6]
$(PbSe)_{1.14}NbSe_2$	0.14	[6]
$(SnSe)_{1.16}NbSe_2$	0.16	[20]
$(SnS)_{1.17}NbS_2$	0.17	[18]
$(La_{0.95}Se)_{1.12}VSe_2$	0.21	[21]
$(YS)_{1.28}CrS_2$	0.28	[22]

1.2: Literature Structural Studies

These materials were first documented in the late 1960s with the form of ABX_3, where A and B are metals and X is a chalcogen.[23] X-ray diffraction and electron diffraction images taken from single crystal studies were initially quite confusing to researchers because the patterns did not match any known compounds. As a consequence, many of the structural refinements that have been published about MLCs over the years include only refined unit cell parameters using either separate parameters for the rock salt and dichalcogenide[6,18,24-28 29] or of a poorly defined, all-encompassing unit cell.[4,9,30-33]

The first refinements of these materials to include position parameters for the atoms were of powder samples that were refined as perovskites[23,34] but were later shown to be MLCs using single crystal refinements.[10,35] Numerous attempts were made to define a unit cell that was appropriate for these compounds. Engelsman et. al. tried an orthorhombic cell for their fit.[36] They also noted an inflated isothermal parameter and relatively high residual values, but theirs was the best fit that had been reported to that point. Leleiveld et al. tried using a primitive space group, Pnma, with a series of compounds which resulted in an inflated isothermal parameter, with low residuals.[37]

Part of the difficulty in finding the appropriate structure for these compounds was their shape. Like franckeite and cylindrite, the naturally occurring forms of these compounds, some of the synthetic materials would form in cylindrical or curved shapes which were believed to be composed of many layers of crystals instead of a single crystal so single crystal x-ray refinement of the crystals was considered an impossibility.[1,38] That was later found to not always be the case, but the appearance of these crystals does not lend itself to that conclusion.[38] Cylindrical shapes were not an issue in electron diffraction studies due to the use of thin films of material. Consequently electron microscopy measurements were used in many structural refinements reported in the late 80s and early 90s .[1,18,22,25,29,39] There are several examples of x-ray structural refinement of these samples using powders instead of single crystals.[6,28 20]

A few studies combined x-ray and electron diffraction on powders in order to more rigorously determine structure by using both sets of data in a single refinement.[39] The final refinements split the MLC into two subunits in order to adequately describe both data sets.[4,18] Subunit notation involves determining and reporting the parameters of

the rock salt separately from the dichalcogenide, then reporting the structure using the language that the two components were interleaved or intercalated. Subunit notation was also adopted when single crystal samples were used.[24,27,35,40-42] Another similar approach was combining the information from subunit refinements directly into a larger unit cell.[43,44 5,43,45] This led to high error values, both residuals and χ^2, and the subsequently dubious quality of the structural determination. Refinements of this type are approximations because most of these samples have an irrational misfit, so it is not possible to establish any number of subunits placed together in order to make a full unit cell.

In order to describe the interaction between the subunits of MLCs, researchers used superspace refinement techniques. Superspace techniques involve the addition of one or more "modulation" vectors to fully describe the stacking at the interface between the samples.[17,35,46-50] The refinements produce a range of bond lengths for each type of bond, which is difficult to visualize. Therefore, the average positions for the atoms were used to make graphics of and define the bond lengths in these refinements. Relatively few materials have been classified in this way because very few crystallographers have had the intensive training needed to master this technique. Also, the addition of the extra vectors needed for these refinements requires an x-ray spectra with a signal to noise ratio great enough that weak satellite peaks can be discerned, step sizes between 0.001˚ and 0.02˚ 2-θ, and non-overlapping peaks, which is available primarily from single crystal data.[51] All the currently known examples of superspace refinements for these systems are of single crystals.

1.3: General Structural Trends

There are general trends that can be observed in all of these refinements, no matter the subunit or superspace approach. When going from the binary component materials to the MLC there are predictable changes to the structure of the components. Normally, the rock salt c parameter becomes smaller and the dichalcogenide c parameter a little larger. This is illustrated in Table 2, the rock salt comparison and Table 3, the dichalcogenide comparison. The materials were chosen to give a broad sampling of the possible values. There is some evidence of charge transfer from the rock salt layer to the dichalcogenide which might account for this difference.[16,52-54]

Table 2: Bulk binary rock salt parameters vs. MLC rock salt subunit parameters for layer to layer thicknesses. The rock salt components are getting smaller when placed into an MLC with one exception.

Compound	spacegroup	Binary 00*l* Δ (nm)	MLC 00*l* Δ (nm)	Diff (Binary-MLC) (nm)
CeS	Fm3m	0.2889[55]	0.285[42]	-0.004
ErS	Fm3m	0.2703[56]	0.270[24]	-0.000
GdS	Fm3m	0.2773[57]	0.275[24]	-0.002
LaS	Fm3m	0.2927[58]	0.290[24]	-0.003
NdS	Fm3m	0.2844[59]	0.285[24]	0.001
PbS	Fm3m	0.2962[60]	0.285[25]	-0.011
SmS	Fm3m	0.2981[61]	0.280[61]	-0.018

Table 3: Bulk binary dichalcogenide parameters vs. MLC dichalcogenide subunit parameters for layer to layer thicknesses. The dichalcogenide components show no significant change.

Compound	spacegroup	Bulk 00*l* Δ (nm)	MLC 00*l* Δ (nm)	Difference (nm)
NbS_2	R3m	0.1489[62]	0.280[25]	+0.131
$NbSe_2$	P63/mmc	0.3036[63]	0.304[6]	-0.009
TaS_2	P -3 m 1	0.1475[64]	0.193[18]	+0.045
TiS_2	P -3 m 1	0.1423[65]	0.194[27]	+0.052
VS_2	P -3 m 1	0.1438[66]	0.200[27]	+0.056

A universal trend in these structures is a distortion of the rock salt within the MLC structure so that the cation is closer to the dichalcogenide layer and the anion further away. This distortion from planarity ranges from 20 pm to 60 pm in the c direction.[17,46 18,19,26,35,47] This range is further highlighted in Table 4.

Table 4: Select literature rock salt disortion values determined by using the average distance in the c direction between the cation and anion of the rock salt at the interface between the rock salt and dichalcogenide.

Compound	MX Distortion (pm)	Reference
$(PbS)_{1.14}(NbS_2)_2$	20.7	[45]
$(SnSe)_{1.16}NbSe_2$	24.6	[20]
$(LaS)_{1.13}TaS_2$	34.7	[46]
$(CeS)_{1.15}TaS_2$	36.2	[46]
$(PbS)_{1.13}TaS_2$	40.0	[42]
$(BiS)_{1.07}TaS_2$	41.6	[17]
$(PbS)_{1.18}TiS_2$	44.1	[47]
$(PbS)_{1.14}NbS_2$	52.1	[19]
$(SnS)_{1.20}TiS_2$	55.4	[35]
$(LaS)_{1.14}NbS_2$	60.6	[19]

1.4: Literature Synthesis Techniques

In some studies, powder and single crystal x-ray scans of these materials produce differing results. [29,67] The powder samples and single crystal samples in each case were made using vapor transport. For single crystal refinements one crystal was chosen to be "representative" of the whole while the powder case the crystals were ground together to form a fine powder. In vapor transport, reagent powders are mixed and placed in an ampoule. The side of the ampoule containing reagent is heated to >700˚C and a transport agent, usually iodine, is introduced to help vaporize the reagents. The gas fills the entire

ampoule and the target material deposits on the cool side. Sometimes there are two annealing steps used, one at a lower temperature, applied to the elemental powder and then the second at a higher temperature with transport gas for a couple of days until single crystals of sufficient size for x-ray diffraction form. Vapor transport usually produces single crystals of sufficient quality for x-ray analysis; however, with misfit layer compounds, sometimes the crystals formed with this technique were not large enough for single crystal techniques.

The vast majority of published structures are $(MX)_{1+\delta}TX_2$ samples. This is due to the fact that they are the easiest to synthesize.[1,10] The naturally occurring minerals found with MLC structure have all been this form. Traditional solid state techniques involving grinding precursors into fine powder and combining them with large amounts of heat (>800˚C) produce $(MX)_{1+\delta}TX_2$ samples as well. Therefore, it can be inferred that these are the thermodynamic products of these types of systems. More rarely, full $(MX_{1+\delta})_1(TX_2)_2$ structures are published.[43,68,69] These papers document the distortion of the rock salt persisting into each layer of rock salt and no change occurring in the dichalcogenide.

1.5: Exceptions to General Trends

A few structural papers fall outside of the norms of the structures mentioned above. One exception describes MLCs with 1.5 layers of rock salt (equivalent to a three atom-thick layer); the compounds that were made include $(Pb_2FeS_3)_{0.58}NbS_2$.[70] $[SrGd_{0.5}S_{1.5}]_{1.16}NbS_2$ and $[Sr(Fe,Nb)_{0.5}S_{1.5}]_{1.13}NbS_2$.[71] In these compounds, the outer atomic layers of rock salt are composed of the cation metal in majority and the inner atomic layer is composed of the cation metal in minority. This gives a unique chemical

environment to the atoms in the center resulting in unique magnetic properties. Another anomalous structure reported is of $[(Pb,Sb)S]_{2.28}NbS_2$, in which there are two rock salt layers.[43] The bilayer of atoms in the second rock salt layer is offset from the first bilayer of atoms, aligning between the M and X in the layer above. This is the only report of such a phenomenon in this literature at this time. Finally, there is a report of a material, $[(Pb,Sn)S]_{1+x}[(Nb,Ti)S_2]_m$, which was found via an EPMA study to have cation mixing within the rock salt layers.[72]

1.6: Samples in this Study

This work will include the structural refinement of new MLCs which have the general form $[(MX)_{1+\delta}]_m[(TX_2)]_n$, where $1 > n$, $m > 5$. These materials had not been previously synthesized because of the limitations outlined in the section 1.4. By using the modulated elemental reactant (MER) synthesis technique it was possible to create a wider variety of structures. MER involves the deposition of a precursor composed of the elements needed to create the desired product in the correct stoichiometric ratio and thickness. The precursor is then gently annealed (< 600˚C) to produce the desired product. Most of the products synthesized in this manner are kinetic instead of thermodynamic compounds.

Using this technique it was possible to create compounds of the following series, $[(PbSe)_{0.99}]_m[WSe_2]_m$, m = 1 to 8. The compounds have the same stoichiometry but varying structure. Samples were also made of $[(PbSe)_{1.00}]_m[MoSe_2]_m$ where m = 1 to 5.[9] These samples have extremely low cross plane thermal conductivity, 0.06 – 0.2 W/mK, which is 5 times lower than the lowest thermal conductivity of PbSe.[9] The unit cell parameters of these compounds are known but the specifics of atom placement are not.

This information is valuable to a great number of modeling experiments where the structure of these materials is integral to the outcome of the model including: electronic band calculations, STEM predictions, and thermal conductivity models. Obtaining structural information on these systems was complicated by their turbostratic disorder and the strong texture of the samples. Turbostratic disorder is a stacking disorder defined by a loss of rotational or translational coherence between layers. The existence of this disorder in our samples was not entirely surprising as other samples formed using MER[73-76] have exhibited similar behavior. Also, in 1990 a group looking at electron microscopy of $SnTaS_3$, $PbTaS_3$ and $BiTaS_3$, all of which were later shown to be MLCs, suggested that MLCs would likely have a stacking disorder though they did not observe one.[25] The end result is that no *hkl*, *h*0*l*, or *k*0*l* reflections for the superstructure exist in x-ray or electron diffraction scans. The *hkl*, *h*0*l*, or *k*0*l* reflections that do appear are those belonging to the rock salt or the dichalcogenide layers.[77,78] They are broad peaks because their grain size is limited by the turbostratic disorder of the samples as well as the average size of the crystal.

Since the samples align with the 00*l* orientation perpendicular to the substrate, the Bragg-Brentano x-ray scans needed for refinement include either the 00*l* or *hk*0 peaks but never both. Therefore, the structure of the c positions was refined independently of the a/b positions of the atoms. This information could not be combined into a full unit cell because the materials have incommensurate parameters. An incommensurate, or superspace, refinement requires more data than is available in these systems in order to be completed with any reliability. The existence of turbostratic disorder makes it

unlikely that, if more data were obtained on any single sample, a corresponding incommensurate refinement could be completed.

Despite this limitation, the structural information obtained from these studies represents an opportunity never before realized. It allows the study of isomeric materials and of layer thickness dependent trends. These studies will have implications as to how these materials are stabilized. The study of isomeric materials will give an indication of how layer thickness affects the interface as well as the transition in the structure from thin film properties to bulk. The layer thickness-dependent trends will help elucidate the affects of changing the ratio of rock salt to dichalcogenide.

All samples in this study were made by various Johnson lab group memebers. The $[(PbSe)_{0.99}]_1[WSe_2]_1$ sample was synthesized and annealed by Dr. Qiyin Lin. The $[(PbSe)_{1.00}]_1[MoSe_2]_1$ sample was synthesized and annealed by Dr. Colby Heideman. The $[(SnSe)_{1.03}]_1[MoSe_2]_1$ sample was made by Ryan Atkins with the supervision of Dr. Colby Hiedeman. All other samples in this study were made by Dr. Qiyin Lin with the assistance of Benjamin Silver, Logan LaRossa, Paul Hansen, and Johnathan Hanni. The Bruker X-ray diffraction scans were taken by the person who synthesized the sample being studied.

X-ray diffraction data taken at the advanced photon source were done in collaboration with Dr. Paul Zschack and Dr. Evguenia Karapetrova who administer beamlines 33 and 34. The samples were run by myself, Dr. Colby Heideman, Dr. Qiyin Lin, Dr. Ngoc Nguyen, Raimar Rostek, and Dr. Clay Mortenson. The space group used for the 00*l* refinements was first used for this purpose by Dr. Arwyn Smalley and Fred Harris for $[(Bi_2Te_3)_{1.36}]_x[TiTe_2]_y$ superlattice samples. Dr. Angus Wilkinson helped them

to develop this method of refining 00*l* data. The use of LeBail fits was suggested by Dr. Brian H. Toby. The modifications needed to apply this to MLCs were determined during conversations with Dr. Qiyin Lin.

I wrote Chapter 3, but it has been heavily edited by David C. Johnson and lightly edited by Qiyin Lin and Colby Hiedeman. Chapter 5 was written primarily by Michael D. Anderson and edited for detail by myself, David C. Johnson, Ian Anderson, Qiyin Lin, and Robert Kykyneshi for details concerning our individual contributions.

CHAPTER II

EXPERIMENTAL

2.1: Data Collection

The majority of the structural data contained in this thesis was generated using data taken at the Advanced Photon Source (APS). Several different types of scans were performed on the samples; cross-plane scans using a θ-2θ scan in parallel beam optical geometry, in-plane scans using grazing incidence geometry, and area detector scans (for k-space mapping). Anomalous scattering experiments were performed using data from below and on the Pb L_3 absorption edge or the Se K_β absorption edge.

APS is a third generation synchrotron source which utilizes a top down insertion method to deliver stable high-intensity x-rays to users. The 33-BM, a bend magnet device, and 33-ID, a type A undulator insertion device, beamlines were used to collect the data used in this dissertation. The bend magnet provides lower flux than the insertion device by a factor of about 100. Energies were tuned using a Si(III) double-crystal monochromator. Dynamically bent mirrors were used for harmonic rejection and vertical focusing; while sagitally bent Si crystals provided monochromatic x-rays with narrow band-width and horizontal focusing. Slits, ion chambers, and beam position monitors permit dynamic feedback control and x-ray beam monitoring to produce brilliant, stable x-ray beams suitable for diffraction, scattering, or imaging applications.[1]

For cross plane scans which probed the 00*l* reflections and area detector scans which probed reciprocal space the incidence slits and detector slits were optimized for

each sample, at each energy in order to be slightly larger than the spot size of the focused x-ray beam. The spot size was determined using x-ray sensitive paper mounted on a pinpoint. For grazing incidence scans which probed *hk*0 reflections the vertical was set to a height of 3 mm and the horizontal slits were set as large as possible, with a width of 10 mm, in order to capture the signal as the geometry causes the beam to diffract away from the detector slits and toward the gear mounts for the detector.

When doing area detector scans, otherwise known as k-space mapping, a MAR 345 image plate detector was placed as close to the sample as was physically possible in order to the largest possible portion of reciprocal space. The incidence slits were optimized for the energy of the incoming beam by taking several images of the incoming beam until the signal to noise was optimized. Although using a high energy beam would have resulted in a larger slice of k-space being represented in the area detector scans, the energy of the beam was set to the same one that would be used for anomalous scattering on that particular visit. This was a time saving measure, as changing energies over large ranges costs a significant amount of time, which is at a premium when using an APS beamline. Each sample was placed parallel to the incident beam with χ equal to 0° and optically aligned using a laser alignment system. Each sample was run for a variety of exposure times in order to get the best possible signal to noise ratio, usually between 1 and 5 seconds. Times that were too short resulted in too few photons being collected and times that were too long resulted in oversaturation of the detector. The NIST 660b[2] LaB_6 standard reference material was used to determine the tilt of the detector, its distance from the sample, and the exact wavelength of the incoming beam by using the Fit2D software calibration algorithms to calibrate the images based on the known positions of

the standard peaks.[3] The sample generated peaks were then indexed as either MLC peaks, rock salt peaks, or dichalcogenide peaks.

Some data in this thesis were taken using a lab diffractometer, which has significantly lower flux than a synchrotron and only provides one wavelength. These data were taken using the Bruker D8 Discovery system with a Cu K_α source, 0.1540562 Å, arranged in a parallel beam geometry using a Göbel mirror a 0.001˚ step size and a 1 sec count time. The soller slits were 1 mm incidence and detector slits to focus the beam and a 0.6 mm anti-scatter slit. In order to elucidate the preferred orientation of the samples rocking curves were run on the 00*l* peaks from $l = 2$ to 8 for the $[(PbSe)_{1.00}]_1[MoSe_2]_1$ system.

2.2: The Rietveld Method

In order to derive as much structural information as possible from these x-ray diffraction studies, Rietveld refinement was used. Rietveld refinement was originally developed as a technique to deal with structural solutions for powder diffraction. Powder diffraction results in many overlapping peaks, which complicate the determination of the underlying crystal structure. Hugo Rietveld realized that by comparing a calculated diffractogram based on a model to the experimental diffractogram it should be possible to match the two and thereby determine the structure of powder samples accurately.[4] In fact, Rietveld showed that his technique produced refinement results for powders that were comparable to single crystal refinements for a variety of systems.[5] This powerful concept is now used for both powder samples and single crystal samples.

In order to determine structure using Rietveld refinement, a model of the proposed structure is incrementally refined using a non-linear least squares fit between

the calculated diffractogram and the experimental data. At each step of the refinement the model parameters are altered slightly, an x-ray diffractogram is generated for the new model, and then the diffractogram is compared to the experimental data with a non-linear least squares fit, quantified by the goodness of fit parameter χ^2. If the change reduces χ^2, equation 4, the change is accepted; if not it is rejected.

A starting model for a refinement has instrumental parameters and a unit cell representation containing symmetry (space group), dimensions, and atom identity and placement within the cell. Without a good starting model, one the same space group and unit cell size and similar locations (exact same for special positions) and occupancies for the component atoms when compared to the final refined structure, the Rietveld technique does not converge to a refined structure. For example, if you are trying to refine a structure that is in reality cubic using an orthorhombic cell you will are very unlikely to get an acceptable result as you will not be able to generate the appropriate reflections using the wrong symmetry. Theoretically, the unit cell might refine to a = b = c if given enough time but in practice this generally results in a the values in the matrix diverging. The reverse is also true, a cubic cell cannot be refined using orthorhombic conditions. Additionally, a Rietveld refinement will not work if the atoms specified are not in the correct proportion or if they have the incorrect Z. Basic structural and composition knowledge about a sample is a necessity in using this technique, but once those parameters are determined Rietveld can be used to gain much more specific and accurate information about both structure and composition of the compounds present in the diffraction data. False minima are also possible but are often physically impossible solutions. For example, a solution in which the occupancy of an atom is negative.

In order to generate a diffractogram a string of equations is used, each representing a specific aspect of the measurement. The sample itself is represented using the structure factor, *F*, preferred alignment parameters where appropriate, and profile broadening which is usually caused by microstrain or grain size. Instrument effects that are modeled include, instrumental broadening, sample alignment corrections, x-ray wavelength, and beam profile. Background radiation is also modeled as a single polynomial function though it has contributions from both the sample and the instrumentation. Many of these components are broken down further into contributions from more specific aspects of the general cases above.

The central equation used in structural determination is the structure factor. The general structure factor for a single phase, F_{ph}, can be represented using Equation 1:

Equation 1

$$F_{ph} = A_{ph} + iB_{ph}.^{6}$$

There is a separate structure factor for each phase in the sample, each with a real, A_{ph} and imaginary component iB_{ph}. The observed intensity from Bragg scattering in the sample, Equation 2, is the sum of the squares of the structure factors of each phase present in the sample.[6]

Equation 2

$$F_c^2 = \sum_{ph=1}^{x} A_x^2 - B_x^2$$

The structure can be further broken down into contributions from x-ray form factors, atomic site fraction, and thermal motion parameters.

The IUCr sponsored a series of Rietveld round robins and general studies on Rietveld refinement in order to determine the best strategies for obtaining accurate

refinement results for a variety of applications.[7-15] The studies relevant to this thesis deal with instrumental effects on spectra,[14] error analysis,[15] grain size vs. strain line broadening,[7] and general refinement methodology.[9, 14] They demonstrate that refinement strategies are dependent on the type of sample being modeled and on what type of instrument it is measured. Where applicable to multi-layer thin film samples, the recommendations made in those papers were used to guide this inquiry. For example, the instrumental corrections that are based on geometry, zero and shift, were used only the appropriate geometry.

The samples in this study are unique in many ways and require a modified approach from those presented in the studies mentioned in the above paragraph. The first difference is that the samples are textured thin films on smooth substrates. The degree of texturing is strong enough that, depending on the sample geometry, different reflections are observed. Analysis normal to the plane of the substrate results in reflections from the 00*l* family, while analysis parallel to the substrate results in *hk*0 reflections. There is turbostratic disorder, a random stacking of the layers along the c axis, which further complicates structural determination because it cannot be modeled using most traditional techniques. As a result, the refinements in this dissertation are done using two separate refinements, one for the 00*l* data and one for *hk*0 data where available.

The cross-plane histograms were refined using models in which the space group was $P\bar{3}m1$ with unit cell dimensions such that only the z coordinates were refined. The initial unit cell c parameter was determined by using Bragg's Law $n\lambda = 2d\sin\theta$, where n is the 00*l* index of the peak, λ is the wavelength of the x-ray beam, d is the d-spacing, and θ is the angle of the reflection. The d-spacing represents the c value for 00*l* scans. This

calculation was done with each reflection and the average value was used. The atom positions in the initial model were determined using the spacing between the atom planes in the c-direction based on literature examples of the component substances where available and best guess approximations based on the literature of similar materials where not available (SnSe is not stable as a rock salt when not in an MLC). The fractional occupancy of each position was determined by the tiling factor, δ, between the two layers. The δ value was determined by indexing the area detector scans or *hk*0 scans of sample and using Bragg's Law to determine the a and b parameters for each subunit of the MLC, then applying them to the following equation:

Equation 3

$$\delta = \frac{Z_{rs} A_D}{Z_D A_{rs}},$$

where Z_{rs} is the number of atoms in the rock salt unit cell, A_D is the area of the dichalcogenide in the a/b plane, Z_D is the number of atoms in the dichalcogenide unit cell, and A_{rs} is the area of the rock salt in the a/b plane. Each rock salt plane was represented as 50% cation and 50% anion.

The *hk*0 data was refined as a compound containing two subunits, one for the rock salt and one for the dichalcogenide. The a and b parameters were determined to be equal for both the dichalcogenide and rock salt components of each sample. The c parameter was the same used in the 00*l* refinement. Both the rock salt and dichalcogenide were given a preferred orientation in order to eliminate the presence of the 00*l* and *hkl* peaks. The rock salt space group was solved presuming plane group symmetry, which in practical terms was the P 2 3 space group. The cell was given 8 edge atoms in 4 positions. At each position the atoms were represented as ½ M and ½ X atoms for a total

Z of 1. The space group of the dichalcogenide material component was based on literature value, with atoms placed in the special positions required by that space group. The fractional occupancy was not refined because there were not enough peaks to refine those extra parameters with any accuracy. Therefore, the a and b parameters and U_{iso} were the only structural parameters refined in these refinements.

For the data in this thesis, simultaneous refinements were done of the anomalous scattering scans. If no anomalous data was available, the refinement was completed using the wavelength available. Models refined using anomalous scattering data are more accurate than those using a single wavelength in large part because there is a contrast in peak intensity due to taking measurements above and below the absorption edge of a given element, but also because there are two times as many points available for analysis when using two wavelengths. Refinements with one APS wavelength are more accurate than those done using Bruker data because of the increased flux available at APS which contributes to a greater signal to noise in the final data set. The best refinement strategy for these samples is to refine the unit cell, background, profile, and instrument parameters using a LeBail fit, a fitting algorithm which automatically matches the peak height of the data while allowing the aforementioned parameters to refine. LeBail fits represent the best possible outcome of a refinement. The synchrotron based corrections (zero correction and instrument parameters) were used for synchrotron data and the lab diffractometer settings (shift correction and instrument parameters) were used for Bruker data. LeBail fits were employed as a method of reducing the error of the refinement by helping to deconvolve the instrument parameters from the model parameters in the fit, as well as providing a stopping point to each refinement.[16]

The instrumental and profile parameters derived from the LeBail calculations were used in the Rietveld refinement as a starting point. The remaining model parameters were refined in the following order: the position of the heaviest atoms, the position of the lighter atoms simultaneously with the heaviest atoms, U_{iso}, and finally in some instances the fractional occupancy. Uiso was constrained in every refinement to be a single value for all of the atoms in the model. This was a soft constraint and required that all the Uiso values of the atoms be refined simultaneously in order for the constraint to apply. Various other soft constraints were used at different points in the refinements whenever an unrestrained least squares run resulted in divergence of the parameters, incalculable values caused by dividing by zero, going to infinity, or values outside the allowed data range. These included constraining the step size change allowed in the value being refined, refining first the components due to the rock salt then the dichalcogenide (pertinent when dealing with Se coordinates), constraining the position variables for the dichalcogenide layer to fluctuate in proportion to one another, and constraining the rock salt cation to be closer to the Se layer of the dichalcogenide layer than the rock salt anion. This technique is in general agreement with the strategies described in the Rietveld round robin papers.

The round robins also indicate that because Rietveld uses a least squares technique, it is essential to avoid simultaneously refining parameters that are statistically correlated. Because of this all refinement programs allow the choice of which variables are refined for a given set of iterations. There are several such parameters in any given refinement. For example the structure factor and the isothermal parameter are interdependent as their calculation includes many of the same variables including the *hkl*

matrix that represents the symmetry and location of all the atoms in the unit cell with the model. The profile contributions from the sample and the instrument cannot be deconvolved without significant standardization of the instrument. Finally, the x-ray wavelength and unit cell dimensions have a dependent relationship based on Bragg's law. There are a variety of Rietveld refinement programs available on that cater to a variety of refinement needs. The General Structure Analysis System[17] (GSAS) with experimental graphical user interface[18] (EXPGUI) was used for the refinements contained in this work. It is a versatile program with ongoing technical support provided by Robert von Dreele, Alan C. Larson, and Brian H. Toby. There is a series of informative lectures on most aspects of GSAS and Rietveld refinement in general that was produced by Brian H. Toby.[19] These lectures include information on theory and its implementation using various aspects of the GSAS program.

2.3: Experimental Methods and Modeling

The refinements in this study were completed by using multiple starting models converging to the same point in order to explore the possible parameter space more thoroughly. In order to determine the positions of each atom in the unit cell, similar examples found in the literature were used along with several assumptions. It is well documented that in MLCs the rock salt distorts. The rock salt cation is closer to the anion in the dichalcogenide than the anion in the rock salt is, with the magnitude of 20 pm to 60 pm according to the literature. [20-26] This distortion is not usually accompanied by a concurrent distortion in the value of the a and b parameters. It was also found that the dichalcogenide layer does not change significantly in any structural detail when placed in an MLC in both m = n = 1 samples and m = 1, n = 2 or 3.[27, 28]

There is no literature precedent on how the layering structure of an MLC would change as both component layers get thicker than those examples above. In order to create models which would evolve with the number of layers, it was therefore necessary to posit several hypotheses about how the isomer system would change. The stability of these compounds and the distortion of the rock salt are attributed to charge transfer between the layers, rock salt donating electron density to dichalcogenide.[29-35] It is believed that the major changes in the structure will be in the electron donating layers. The rock salt distortion could decrease toward the center of the each rock salt layer as the energy cost of distorting each successive layer is larger than the previous layer and the amount of charge transfer in an isomeric system should not change significantly from sample to sample, so models were given gradual tapering of the distortion parameter. Concurrently, the magnitude of the rock salt distortion could decrease with an increasing number of layers so it was modeled as 0 pm, 20 pm, 40 pm and 60 pm. It is also possible that there would be slight changes in the dichalcogenide layer as a result of increasing the number of layers. This was likely to be a small effect and the T-X bond was modeled as 0.15 nm or 0.16 nm. Finally, the average distance between the rock salt and dichalcogenide layers was estimated by using the van der Waals gap of the dichalcogenide and subtracting ½ the rock salt distortion magnitude used in a given model. From these general parameters multiple models were generated combining the possibilities generated by the assumptions above.

The results of these various refinements yielded a variety of results for each sample. Some of the results were contained non-physical values and those models were discarded. The models resulting in reasonable values were combined and the values a

given refined sample are the average positions, fractional occupancies and isothermal values from this combination. In general these averages were of 6 refinements; though details concerning how many models were used are found in each refinement summary. The number of starting models employed to get to those six refinements was determined by the number of parameters needed to complete the model. The first starting models refined were always of the simplest MLC in each system, an $[(MX)_{1-\delta}]_1[TX_2]_1$ sample. If this simple MLC model did give a satisfactory fit (as determined by closeness of the wrp, rp, and χ^2 values to the corresponding LeBail fit values), additional variables were used. The first additional variable was cation mixing, a phenomenon previously reported for a $[(Pb,Sn)S]_{1+\delta}[(Nb,Ti)S_2]_m$ system,[36] using three scenarios, where the dichalcogenide has rock salt cation in some of the positions, where the rock salt has some dichalcogenide cation in some of the positions and finally where both the rock salt and dichalcogenide cations exchange to some degree. If this option did not help, and the sample had multiple dichalcogenide layers, the simple model was used with intercalated cations in the van der Waal gap. The details of these starting models can be found in Appendix B.

The package includes an error analysis suite with parameters meant to elucidate a variety of refinement problems. The most important of these analysis functions was defined by Hugo Rietveld as goodness of fit, χ^2, which is used for the least squares acceptance criteria.[5] Though it is known as a goodness of fit parameter the underlying statistical concept is of a probability distribution. As it is applied here, the parameter describes provides a numerical standard for the entire data set and should approach 1 ideally. Tolerances placed on changes in this number determine the acceptance or rejection of changes made to a given parameter. For a powder or set of powder

diffractograms (thin films behave analogously to powder diffraction), it is represented within GSAS as Equation 4:[37]

Equation 4

$$\chi^2 = \frac{\sum_{p=1}^{n} f_p \sum w(I_o - I_c)^2}{N_{obs} - N_{\text{var}}};$$

where p is a diffractogram, f_p is a scaling factor for the diffractogram, w is a factor determined by error propagation during the refinement, I_o is the observed intensity, I_c is the calculated intensity, N_{obs} is the number of observations from all of the diffractograms, and N_{var} is the number of variables in the refinement.

The most important parameters for determination of quality of fit are the Fitted w_{rp}, Equation 5, and r_p, Equation 6, and the Background w_{rp}, Equation 7, and r_p, Equation 8. These are represented in the following equations[37]:

Equation 5

$$w_{rp} = \sqrt{\frac{\sum w(I_o - I_c)^2}{\sum w I_o^2}}$$

Equation 6

$$R_p = \frac{\sum |I_o - I_c|}{\sum I_o}$$

Equation 7

$$w_{rp} = \sqrt{\frac{\sum w\left(\frac{(I_o - I_c)(I_o - I_b)}{I_o}\right)^2}{\sum w(I_o - I_b)^2}}$$

Equation 8

$$r_p = \frac{\sum \frac{|I_o - I_c| \cdot |I_o - I_b|}{I_o}}{\sum |I_o - I_b|},$$

where w is a weighting factor derived using the standard deviation value calculated for each parameter during the least squares procedure, I_o is the observed intensity, I_c is the calculated intensity, and I_b is the background intensity. The fitted w_{rp} and r_p give a good indication of how good the fit actually is. Unlike, χ^2 these values reflect more closely on the match between the calculated and experimental histogram. The background w_{rp} and r_p are weighted by the residuals left by the difference between the experimental data and the background function and are generally higher than the fitted parameters as a result. The background function is calculated using a Chebyshev polynomial.[37] The wrp values give the best indication of how well the off peak positions are fit because they are weighted which dampens the effect of the most intense peaks in the error analysis so that each peak is contributing approximately equivalently. Finally, GSAS calculates an error value, D_{wd} which is associated with the degree of serial correlation in the powder pattern differences, called the Durbin-Watson statistic.[38, 39] This is calculated using Equation 9:

Equation 9

$$D_{wd} = \frac{\sum \Delta_i / \sigma_i - \Delta_{i-1} / \sigma_{i-1}}{\sum_{i=1}^{N} (\Delta_i / \sigma_i)^2},$$

where Δ_i is the difference between the observed and calculated values for a given point, σ_i is the error values associated with that point, Δ_{i-1} is the difference between the next consecutive observed and calculated values in the histogram, and σ_{i-1} is the error values associated with that next consecutive point. In a completely uncorrelated data set the D_{wd} should be 2, values below 1 or greater than 3 are generally considered to indicate serial correlation in the sample.[39] The samples in this study have highly correlated data because of the Kiessig fringing which is not included in the model, so their values are

usually ~2 pm.

Using all of these statistical values it is possible to get a complete picture of how well the model fits to the data. There is also the additional inclusion of the standard deviation on each refined parameter. The error on the data in these refinements was calculated using a weighted standard deviation. Because the reported values are the average result from multiple refinements, the error is calculated by weighting using the standard deviation reported on each included parameter from every included model. This gives a value that is slightly higher than can be calculated from the standard deviation of the model values. The true error in the positional data based on this average is still low when compared to the range of possible solutions to each refinement. The lower limit for the accuracy of the reinments was determined by the quality of the data available which was based on the time constraints for data collection at APS.

CHAPTER III

THE STRUCTURE OF TURBOSTRATICALLY DISORDERED MISFIT LAYERED COMPOUNDS $[(PbSe)_{0.99}]_1[WSe_2]_1$, $[(PbSe)_{1.00}]_1[MoSe_2]_1$, AND $[(SnSe)_{1.03}]_1[MoSe_2]_1$

The $[(PbSe)_{0.99}]_1[WSe_2]_1$ sample was synthesized and annealed by Dr. Qiyin Lin. The $[(PbSe)_{1.00}]_1[MoSe_2]_1$ sample was synthesized and annealed by Dr. Colby Heideman. The $[(SnSe)_{1.03}]_1[MoSe_2]_1$ sample was made by Ryan Atkins with the supervision of Dr. Colby Hiedeman. X-ray diffraction data taken at the advanced photon source were done in collaboration with Dr. Paul Zschack and Dr. Evguenia Karapetrova who administer beamlines 33 and 34. The samples were run by myself, Dr. Colby Heideman, Dr. Qiyin Lin, Dr. Ngoc Nguyen, and Dr. Clay Mortenson. The space group used for the 00*l* refinements was first used for this purpose by Dr. Arwyn Smalley and Fred Harris for $[(Bi_2Te_3)_{1.36}]_x[TiTe_2]_y$ superlattice samples. Dr. Angus Wilkinson helped them to develop this method of refining 00*l* data. The use of LeBail fits was suggested by Dr. Brian H. Toby. The STEM-HAADF image was measured by Michael D. Anderson in collaboration with Ian M. Anderson at NIST. I completed all of the Rietveld refinements found in this chapter as well as the subsequent data analysis. I am primary author of this chapter but it has been heavily edited by my advisor, David C. Johnson as well as edited for detail by Qiyin Lin, Mike Anderson, and Colby Hiedeman. This chapter will be submitted for publication pending approval by the co-authors listed above.

3.1: Introduction

Misfit layered compounds are a large class of naturally nanostructured compounds that occur for a variety of different structure types.[1-3] The largest family of man-made misfit compounds, prepared by direct reaction of the elements at temperatures around 1000°C, are built from transition metal dichalcogenide layers interleaved with rock salt layers. There is an incommensurate structural relationship between these layers, leading to the general formula $[(MX)_{1+\delta}]_m[TX_2]_n$, where M = Y, Pb, Sn, Bi, Sb and the rare earth metals; T is a group IVA, VA or VIA metal; and X = S or Se. δ reflects the difference between the density of atoms in the MX and TX_2 structures in the common a-b plane and is referred to as the mismatch parameter. The known compounds in this class have electrical properties ranging from semiconducting[4-7] to metallic,[8-13] including low temperature superconductivity.[8, 14-18] Their incommensurate structure can lead to other unusual physical properties, including low lattice thermal conductivity[19] and two-dimensional magnetism.[10, 20, 21] While first prepared in the 1970's, there is still debate on why these compounds form, what stabilizes their unique structures, and the extent of charge transfer between the constituents.[22-28] These questions remain, in part, due to the difficulties in the synthesis of misfit layered compounds and to the challenges in determining the structures of these compounds, which typically require four or higher dimensional space to solve due to the structural mismatch between constituents.

These compounds have historically been prepared as powders by direct high temperature solid-state reaction of the elements.[29] Vapor phase transport in a temperature gradient is typically used to prepare single crystals.[2, 29] The majority of the misfit layered compounds prepared using this technique are composed of two distorted 100 rock salt

planes (m = 1) and one to three layers of the transition metal dichalcogenide (n = 1-3). As shown in

Figure 3, the dichalcogenide layer is composed of a hexagonal sheet of transition metal atoms sandwiched between hexagonal sheets of chalcogen atoms, forming a X-T-X trilayer. The MX component when m equals one consists of two 100 distorted planes with rock salt structure, where the metal cation in the rock salt is displaced towards the chalcogen in the dichalcogenide layer and the chalcogen in the rock salt displaced away from the layer of chalcogen atoms in the dichalcogenide. The magnitude of the rock salt distortion is from 20 pm to 60 pm in the relatively few atomic

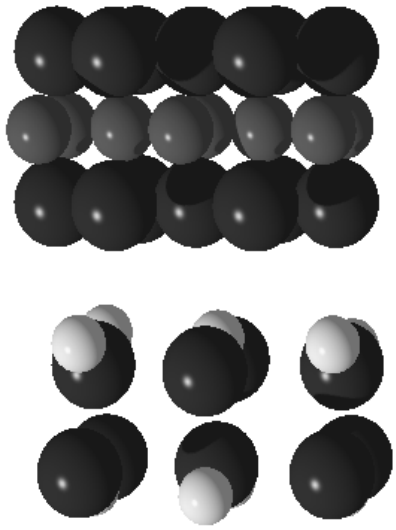

Figure 3: A schematic representation of the structure of $[(MX)_{1+\delta}]_1[TX_2]_1$, where M is medium grey, X is dark grey, and T is light grey. In the conventional formulism for these misfit compounds, the subscript 1 for the rock salt constituent, MX, represents a bilayer that consists of two 100 planes of a distorted rock salt structure. The M atoms are displaced towards the chalcogen plane of the TX_2 component (exaggerated in the schematic above). The dichalcogenide consists of a trilayer with a hexagonal layer of transition metal T in the center with hexagonal sheets of chalcogen on either side of the transition metal layer.

level structures that have been determined.[12, 30-36] There is a lattice mismatch between the rock salt and the dichalcogenides constituents along one or both of the in-plane lattice

parameters. This difference ranges between 205 pm and 259 pm.[6, 8, 10, 11, 29, 31, 33, 34, 37-48] The value of δ, which reflects the difference between the density of atoms in the MX and TX_2 structures in the common a-b plane, ranges between 0.07 and 0.29.[6, 8, 10, 11, 29, 31, 33, 34, 37-48] Solving the detailed atomic structure of these compounds from diffraction data was a significant challenge for conventional crystallography due to the mismatch in these intergrowth crystal systems.[41] In the 1990's, van Smaalen used superspace crystal theory, incorporating additional dimensions into the lattice refinement to account for the mutual modulation of the two sub-structures, to provide the first detailed crystal data on this class of compounds.[30-32]

This chapter discusses the structure of three new misfit layer compounds, $[(PbSe)_{0.99}]_1[WSe_2]_1$, $[(PbSe)_{1.00}]_1[MoSe_2]_1$, and $[(SnSe)_{1.03}]_1[MoSe_2]_1$, made using modulated elemental reactants.[49] There are currently no reports of these compounds prepared using conventional synthetic approaches, presumably because they are only kinetically stable. In the modulated elemental synthesis approach, elements are sequentially deposited creating sub nanometer diffusion distances that can be adjusted to control the kinetics of solid-state reactions, enabling kinetically stable compounds to be prepared. X-ray diffraction and transmission electron microscopy results presented here show that misfit layered compounds prepared from modulated elemental reactants differ from those prepared using high temperature synthesis in having both incommensurate a- and b-axis lattice parameters, the smallest values for δ, including the first negative value reported, and turbostratic disorder (a random translation or rotation from one layer to the next) between the constituent layers. We believe that this is the first report of extensive turbostratic disorder within misfit layer compounds, which was theorized to be the cause

of extremely low thermal conductivity in WSe_2 prepared using modulated elemental reactants.[50] This turbostratic disorder is consistent with the extremely low thermal conductivities of $[(PbSe)_{0.99}]_1[WSe_2]_1$ and $[(PbSe)_{1.00}]_1[MoSe_2]_1$ previously reported.[19]

3.2: Experimental

All samples in this study were prepared using a custom high vacuum deposition chamber (~10^{-7} Torr) which is described elsewhere.[51] Lead, tungsten, tin, and molybdenum were deposited using electron beam guns and Se was deposited with a Knudsen evaporation cell. Precursors were prepared by sequentially depositing each element to prepare a repeating unit with a composition profile similar to the desired final product and then this sequence of elemental layers was repeated to obtain the desired total thickness of the film. The relative thickness of the pair of elements to form each binary constituent was calibrated to obtain the composition that corresponds to the stoichiometry of the desired constituent. The thickness of each elemental pair was adjusted to yield layers with the number of atoms required to form a discrete crystalline MSe bilayer or a TSe_2 trilayer respectively. The deposition produces a mostly amorphous precursor, which is then gently annealed to form the desired product. This process is described in detail elsewhere.[52] Samples were annealed at 400°C in a nitrogen atmosphere, with the $[(PbSe)_{0.99}]_1[WSe_2]_1$ samples annealed for an hour and the $[(PbSe)_{1.00}]_1[MoSe_2]_1$ and $[(SnSe)_{1.03}]_1[MoSe_2]_1$ samples annealed for 30 min.

X-ray diffraction patterns of $[(PbSe)_{0.99}]_1[WSe_2]_1$ and $[(PbSe)_{1.00}]_1[MoSe_2]_1$ were measured in the high resolution 33ID beam line and $[(SnSe)_{1.03}]_1[MoSe_2]_1$ was measured on the 33-BM beam line of the Advanced Photon Source (APS) at Argonne National Laboratory (ANL). Due to the strong texturing of these systems, only *00l* peaks are

present in Bragg-Brentano scans (cross-plane) and only *hk0* peaks are present in grazing incidence 2-theta scans (in-plane). Anomalous scattering experiments measured the cross plane scattering of each sample in the Bragg-Brentano optical geometry. The anomalous scans of $[(PbSe)_{0.99}]_1[WSe_2]_1$ were done above and below the Pb emission line with wavelengths of 95.78 pm and 94.29 pm. Points were taken every 0.005˚ with a count time of 1 second from 12˚ to 50˚ (2θ). The $[(PbSe)_{1.00}]_1[MoSe_2]_1$ sample was measured above and below the Se emission line with wavelengths of 98.19 pm and 98.55 pm with a 0.01˚ step size and 1 second count time from 10˚ to 39˚ (2θ). The $[(SnSe)_{1.03}]_1[MoSe_2]_1$ sample was damaged in the beam and reliable data could not be obtained from the anomalous scattering scans. A cross plane scan was taken for this sample using a Bruker D8 discover diffractometer with Cu K_α radiation and a Göbel mirror in Bragg-Brentano optical geometry with a step size of 0.01˚ and a count time of 1 second. 2-dimensional k-space mapping was obtained on all samples using a MAR345 image plate at a grazing incidence angle of 1.0º. Rocking curve scans were collected on *00l* reflections of each compound using the Bruker D8 Discover diffractometer with Cu K_α radiation.

Rietveld refinement was completed using the General Structural Analysis System (GSAS)[53] with EXPGUI.[54] The 00*l* scans contain Kiessig fringes, interference patterns between the front and back of the sample, which overlap the Bragg reflections out to as high as 30˚ 2θ in some samples. GSAS does not include algorithms to model this phenomenon. At the beginning of each refinement, LeBail fits were performed on each scan and used as a starting point for the model refinement in order to help reduce the error due to correlation caused by overlapping peaks and to refine profile parameters, background, unit cell size and zero offset corrections. The LeBail fit represents the best

possible refinement for a given model and was compared to each refinement of atomic coordinates to gauge the quality of the fit because the presence of Kiessig fringes results in abnormally high error values. The anomalous diffraction data collected along the c-axis was used to refine the z coordinates of the atomic planes using all energies simultaneously. Initial models that extended beyond the known range of distortions in misfit-layered compounds were used to explore parameter space to make sure the refinement did not converge to local minima. Cation mixing was also explored in several models, as this phenomenon has been reported previously in misfit layered compounds.[55] The *hk0* data obtained on $[(PbSe)_{1.00}]_1[MoSe_2]_1$ was used to refine the x and y coordinates of a projection of the structure onto the a-b plane. The sample was treated as two subunits, PbSe and $MoSe_2$. The 00*l* plane was entered as the direction of the preferred orientation and the degree of preferred orientation was refined.

The $[(PbSe)_{0.99}]_1[WSe_2]_1$ and $[(PbSe)_{1.00}]_1[MoSe_2]_1$ samples were also studied using transmission electron microscopy. Cross section specimens for scanning (STEM) and conventional (TEM) transmission electron microscopy analysis were prepared using the small angle cleavage technique (SACT),[56] followed by cleaning and thinning using a FEI NOVA NanoLab DualBeam FIB equipped with a Sidewinder ion column. Samples were thinned to approximately 300 nm using 30 kV accelerating voltage on the ion source followed by a polishing step at 5 kV and final endpointing at 2 kV. Samples were plasma cleaned using a Fischione Instruments model 1020 plasma cleaner for five minutes prior to analysis to remove any organic contamination. Analytical electron microscopy measurements were performed using an FEI Titan STEM/TEM equipped with a double-hexapole spherical aberration (C_s) corrector on the probe forming lens and

operating at 300 kV. Images were collected using a condenser beam convergence semi-angle α = 18 mrad and a high angle annular dark-field (HAADF) detector with an inner semi-angle of β = 60 mrad. Imaging was conducted by first orienting the specimen to the silicon [110] zone axis followed by a lateral stage shift to the site of interest. Orientation at the [110] zone axis of silicon places the cross section of the film normal to the optic axis of the microscope. Image analysis was conducted using the ImageJ for Microscopy suite of plug-ins.[57, 58] Distances were measured using the line tool and the plot profile feature on the calibrated image. A large line width was chosen to provide an average distance over many atomic columns. Special care was taken to ensure that the line was perpendicular to the film cross section during the measurement.

3.3: Results and Discussion

A number of different diffraction experiments were used to unravel the structure of the title compounds. Bragg-Brentano scans of each of the samples, shown in Figure 4, contain a series of Bragg diffraction maxima that can be indexed as *00l* reflections of the indicated misfit layered compounds. The positions of the *00l* reflections were used to determine the c-axis lattice parameter of each sample, which are summarized in Table 5. In the literature, the c-axis lattice parameter of misfit layered selenide compounds range from 14.1 pm larger to 25.0 pm smaller than the sum of the lattice parameters of the bulk components as a result of creating the interface between the constituents and changes in the bonding as a result of charge transfer between constituents.[6, 17] For $[(PbSe)_{0.99}]_{1.0}[WSe_2]_1$ the c lattice parameter is 9.4 pm larger and for $[(PbSe)_{1.00}]_{1.0}[MoSe_2]_1$ the c lattice parameter is 7.0 pm larger than the sum of the bulk components. Both these values are well within the previously reported range. No value

can be provided for this difference for $[(SnSe)_{1.03}]_{1.0}[MoSe_2]_1$, as SnSe alone does not crystallize with a rock salt structure. Rocking curve scans confirmed the textured nature of the samples. The FWHM for rocking curves collected on each of the *00l* reflections measured less than 1.3˚.

Table 5: Lattice parameters for the misfit compounds $[(MSe)_{1+\delta}]_1[TSe_2]_1$ obtained from refinements of the Bragg-Brentano and grazing incident diffraction scans.

Compound	c-axis lattice parameter	a-axis lattice parameter of the TSe_2 constituent	a-axis lattice parameter of the MSe constituent	Calculated value of δ
$[(PbSe)_{0.99}]_{1.0}[WSe_2]_1$	1.2697(3) nm	0.331(1) nm	0.618(2) nm	-0.01
$[(PbSe)_{1.00}]_{1.0}[MoSe_2]_1$	1.2658(2) nm	0.3308(4) nm	0.6182(2) nm	0.00
$[(SnSe)_{1.03}]_{1.0}[MoSe_2]_1$	1.2425(6) nm	0.3308(4) nm	0.608(2) nm	0.03
PbSe	0.6118 nm		0.6125 nm	
WSe_2	0.665 nm	0.3286nm		
$MoSe_2$	0.651 nm	0.3287nm		

Grazing incident scans yielded diffraction patterns (Figure 4) in which all of the diffraction maxima could be indexed as *hk*0 reflections of either the rock salt or dichalcogenides component of the misfit layered compound. The positions of the diffraction maxima in each of the grazing incidence scans are consistent with an undistorted square lattice in the a-b plane for the rock salt constituent and a hexagonal lattice for the dichalcogenide constituent. The a-axis lattice parameters for the rock salt and dichalcogenide components in each compound were calculated from the positions of the *hk*0 reflections and are contained in Table 5. For both $[(PbSe)_{1.00}]_{1.0}[MoSe_2]_1$ and $[(PbSe)_{0.99}]_{1.0}[WSe_2]_1$, the refined a-axis lattice parameter of the PbSe constituent was larger than the value of 0.61246 nm observed in the binary compound, but were within the range of values that have been reported in the past in misfit layered compounds.[59, 60] For $[(SnSe)_{1.03}]_{1.0}[MoSe_2]_1$, an a-axis lattice parameter of 0.608 nm for SnSe was

obtained from the refinement. For all the compounds studied, the refined a-axis lattice parameter of the TSe_2 constituent was slightly larger than that observed for the binary compound (0.3287nm for $MoSe_2$ and 0.3286nm for WSe_2).[61, 62] The refined lattice parameters indicate that these compounds have misfits in both the a and b parameters, which has only been observed in two other compounds - $[(PbS)_{1.13}]_1[VS_2]_1$ and $[(SnS)_{1.17}]_1[NbS_2]_1$.[31, 35] The misfit parameter, δ, was calculated for each material from the refined lattice parameters, yielding $\delta = 0.03$ for $[(SnSe)_{1.03}]_1[MoSe_2]_1$,0.00 for $[(PbSe)_{1.00}]_1[MoSe_2]_1$ and -0.01 for $[(PbSe)_{0.99}]_1[WSe_2]_1$. These values for δ are, to the best of our knowledge, the smallest that have ever been observed in chalcogenide misfit compounds. For all three samples, the peak width of the *hk*0 reflections from the rock salt constituent is significantly narrower than the peak width of the *hk*0 reflections from the dichalcogenide constituent. Since each subunit is subject to the same instrumental parameters, the difference in the broadening reflects differences in the crystallite sizes of the constituents. This difference in a-b plane crystallite size has not been reported previously for other misfit-layered compounds and is probably a consequence of the synthesis technique.

The *00l* diffraction scans are consistent with a periodic structure along the c-axis, reflecting a regular stacking of dichalcogenide trilayers and bilayers of the rock salt constituent. Within the a-b plane, the *hk0* diffraction patterns are consistent with hexagonal symmetry of the dichalcogenide trilayers and square symmetry of the 001 planes of the rock salt. To gain information about the relative stacking of the planes, reciprocal space data were collected at the APS using image plates and a representative image plate for $[(PbSe)_{0.99}]_{1.0}[WSe_2]_1$ is shown in Figure 5. All of the reflections, which

can be indexed as *hkl* Bragg peaks of the constituent compounds, are significantly broadened into streaks along the c axis, reflecting an extremely short coherence length in

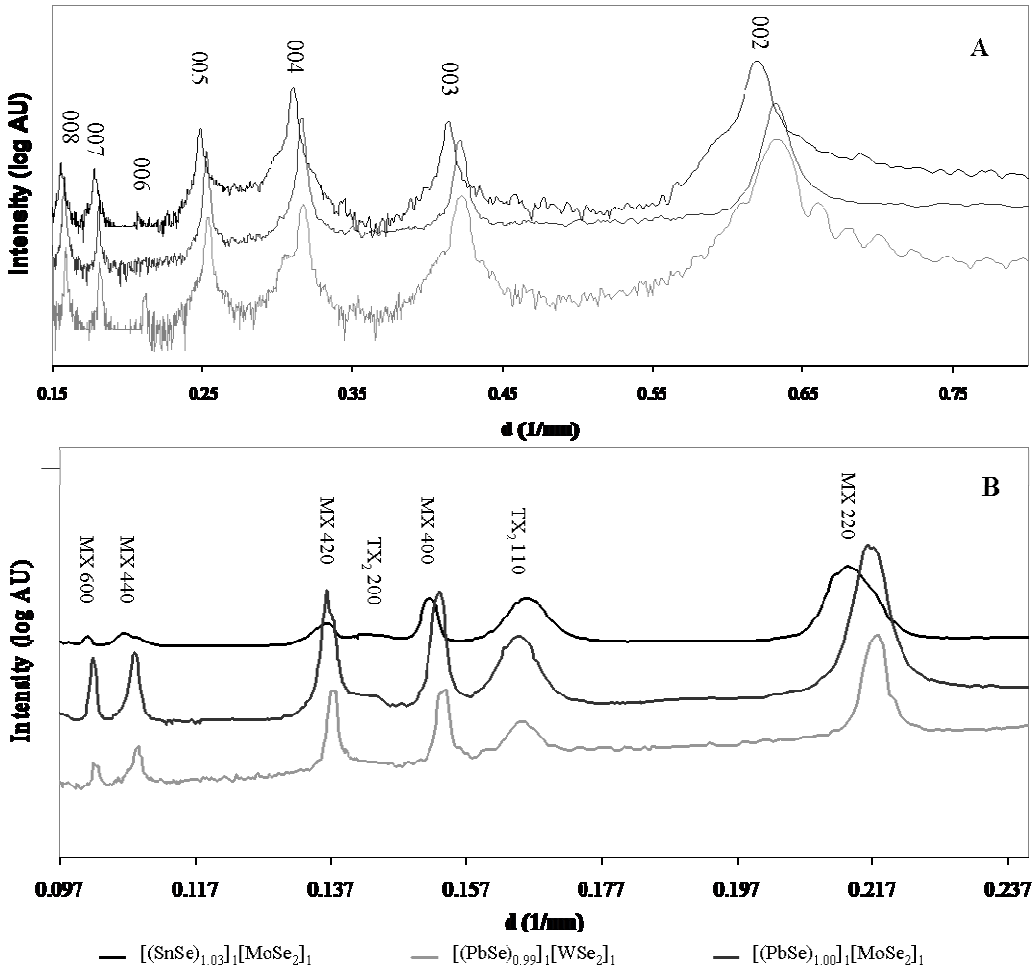

Figure 4: A. contains the Bragg-Brentano diffraction patterns for the three misfit compounds investigated plotted on a logarithmic scale to highlight the weak intensity peaks. All of the diffraction maxima can be indexed as *00l* reflections. B. contains the grazing incidence diffraction patterns for the title compounds. All of the diffraction maxima could be indexed as *hk0* reflections of the components of the misfit compounds.

this direction. There is no evidence of supercell reflections that correspond to the measured c-axis lattice parameter of the misfit compound. The lack of *hkl* supercell reflections and the asymmetry of the *hk0* reflections in the grazing incidence data sets are

consistent with the samples lacking rotational or translational symmetry between layers, which has been referred to as turbostratic disorder.[63]

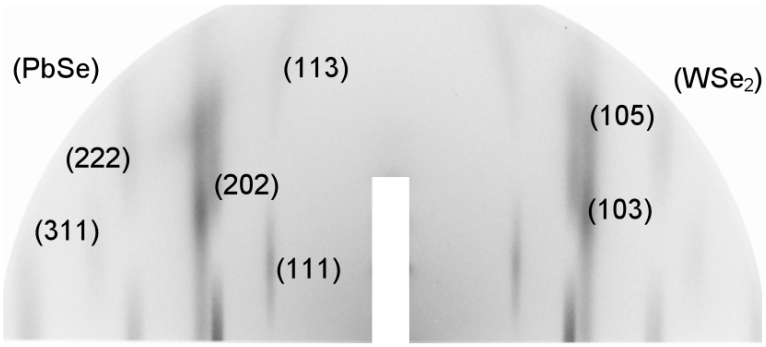

Figure 5: $[(PbSe)_{0.99}]_1[WSe_2]_1$, representative of all the compounds studied, showing the streaks of intensity near the expected reflections for the constituents of this misfit compound, which are labeled with appropriate indices.

Cross-section STEM images from $[(PbSe)_{0.99}]_1[WSe_2]_1$ and $[(PbSe)_{1.00}]_1[MoSe_2]_1$ samples were collected to gain additional insight as to the relative stacking of the layers. A representative STEM-HAADF image of an annealed $[(PbSe)_{1.00}]_1[MoSe_2]_1$ film is shown in Figure 6. The image is of limited quality due to the beam sensitivity of the specimen; nevertheless, the image corroborates the structural information yielded by x-ray diffraction. Individual structural units for both the PbSe and $MoSe_2$ layers are clearly resolved in the image. The parallel orientation of the layers, which coincide with the trace of the substrate in cross section, is consistent with the strong c-axis texturing of the XRD patterns. The regularity in the spacing of these planes is consistent with the remarkable smoothness of the annealed films and consistent with the extended angular range over which Kiessig fringes are evident in the low-angle XRR scans.47 The sporadic appearance of atomic columns in domains localized to within a single constituent layer and with a lateral extent of only a few nanometers, provides additional evidence of turbostratic disorder. The atomic columns of Pb and Se, which dominate the

contrast of the HAADF image, cannot be resolved at arbitrary grain orientations; however, the extent of regions exhibiting atomic columns, which indicate a grain orientation near a low-order zone axis, provide an indication of the grain size. Where they appear, these domains are localized to a single structural layer, consistent with the nanometer-scale coherence length measured by XRD peaks of mixed-plane indices, and with a lateral extent of only a few nanometers, consistent the intraplanar coherence length extracted from the rocking curves of *hk0*-type reflections. The atomic columns of the hexagonal molybdenum array within the dichalcogenide trilayers are barely resolvable. This is the first observation of extensive turbostratic disorder within misfit layer compounds, which probably is a consequence of the synthesis approach which relies on the self assembly of the title compounds from the modulated elemental precursors.

Rietveld refinements of both the *00l* and *hk0* data sets were used to obtain the z coordinate of planes of atoms along the c axis of the misfit compounds and the projection of the structures of each of the constituents on the a-b plane, respectively. The nature of the samples presented some challenges for the refinements. The presence of Kiessig fringes out to relatively high angles in the 00*l* data sets, which cannot be modeled by the Rietveld software, resulted in relatively high errors for the refinement. Lebail fits, which are the best fits possible irrespective of the refined atomic coordinates and thermal parameters, were compared with the fits from the model refinements to estimate the goodness of fits. The difference between the Lebail fit error and the model fit error in each refinement reflects the relative uncertainty of the refined parameters. In the *hk0* scans, the limited number of diffraction peaks for each of the constituents combined with their broadness due to small crystallite size reduced the number of parameters that could

be reliably refined. The structural models were based on prior misfit compound structures, the structures of the parent constituents, and constrained to limit the number of

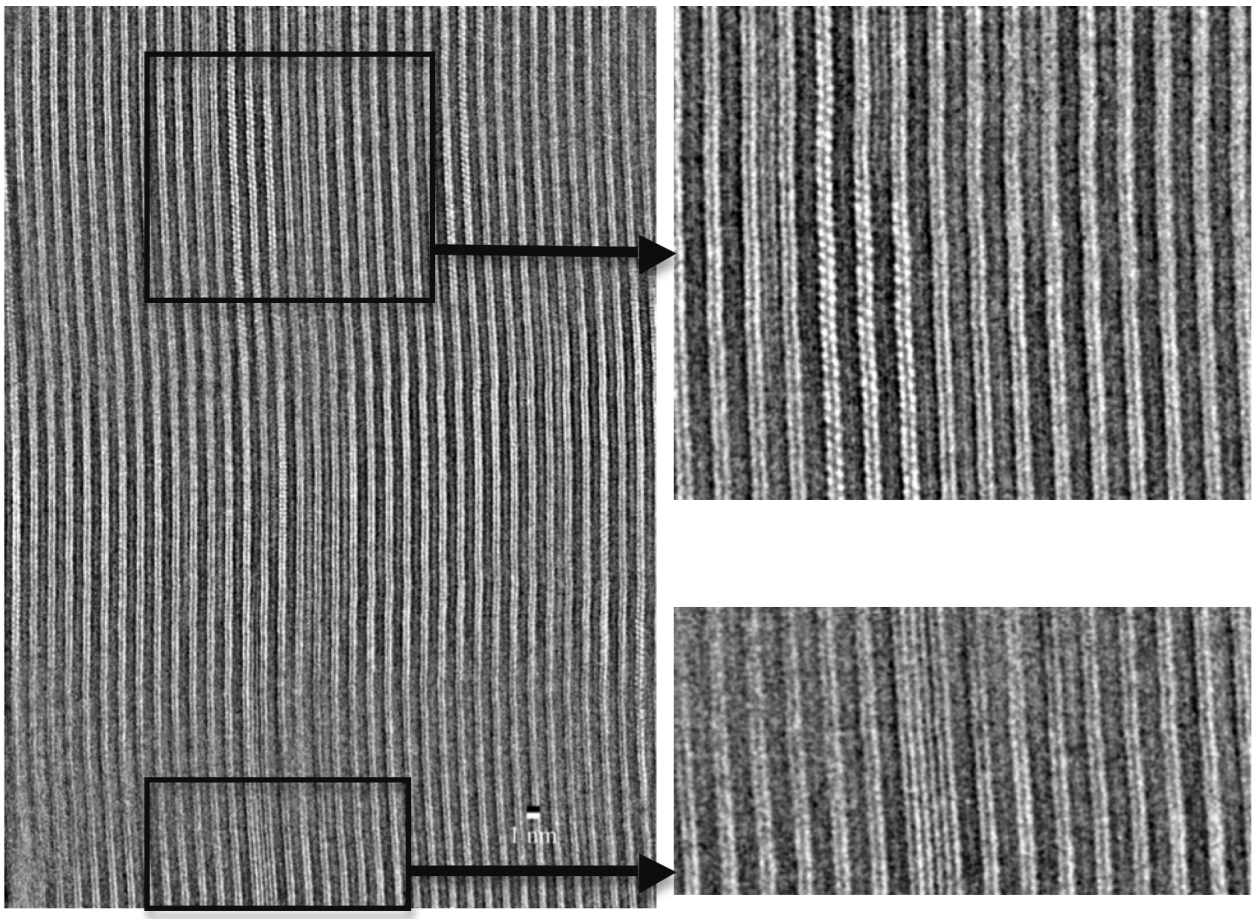

Figure 6: A STEM-HAADF cross-section image of an annealed $[(PbSe)_{1.00}]_1[MoSe_2]_1$ film. The slight waviness of the image is a result of instrument drift during the timescale of the data collection. The top expansion shows a region orientated down a zone axis of the PbSe constituent. The bottom expansion shows a defect where an $MoSe_2$ layer has been replaced by PbSe.

refined parameters. The 00*l* scans were used to define the position of atomic planes of atoms along the c-axis using the $P\bar{3}m1$ spaced group. This space group places a mirror plane in the unit cell which limits the number of planes required to effectively model the data to three; the position of the Se plane in the dichalcogenide, and the position of the M and Se planes in a distorted layer of the rock salt structure. Figure 7 contains a

representative example of the quality of the fits obtained using this structural model and a graphic of the refined $[(PbSe)_{1.00}]_1[MoSe_2]_1$ unit cell. The structural parameters obtained from the refinements for the different compounds and their associated errors are found in Table 6. The larger errors in the $[(SnSe)_{1.03}]_1[MoSe_2]_1$ refinement is a consequence of the smaller experimental data set because the sample was not stable in the beam at the APS.

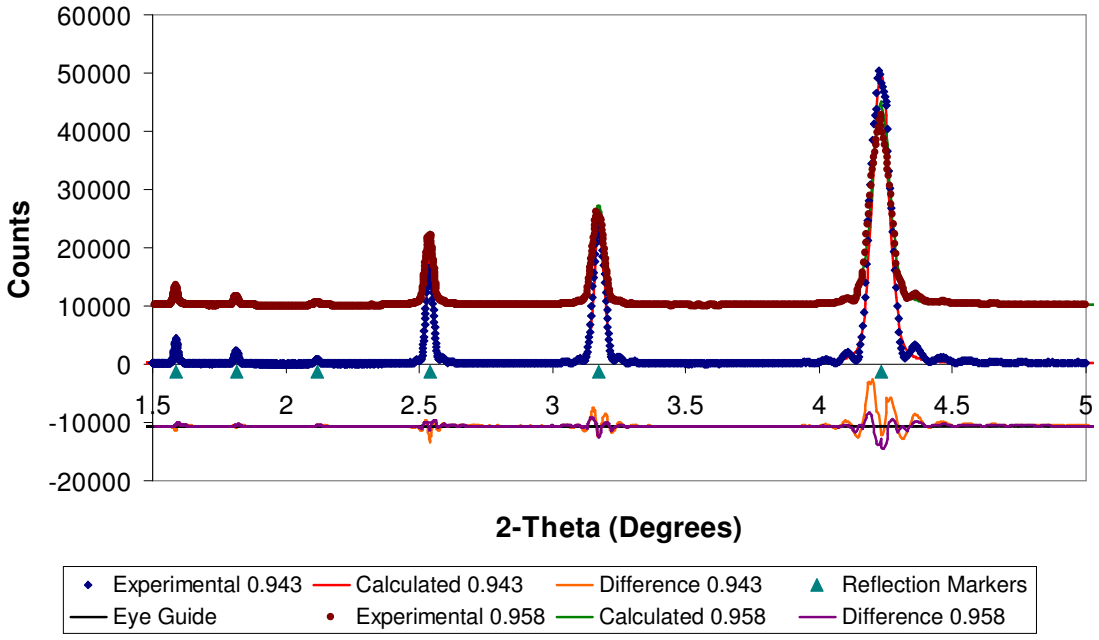

Figure 7: Diffraction data for $[(PbSe)_{1.00}]_1[MoSe_2]_1$ collected at two wavelengths, above and below the Pb absorption edge, is compared to the calculated intensity based on the structural model described in the text. Only the z coordinates are obtained from the refinement of the *00l* scans. The structural parameters that were refined along with their associated errors are contained in table 2.

The refinements quantify the extent of the structural changes from the binary constituents when they are incorporated into a misfit structure. Figure 8 contains a schematic showing the placement of planes of atoms along the c-axis of the misfit structure and defines distances between the different planes of atoms. The calculated distances between the different planes from the refinement for each compound contained in Table 7. The distortion in the rock salt structure, where the cations are attracted to the chalcogen

planes of the dichalcogenide and the selenium atoms are repelled, was found to be 0.023 nm for $[(PbSe)_{1.00}]_1[MoSe_2]_1$, 0.021 nm for $[(PbSe)_{0.99}]_1[WSe_2]_1$, and 0.03 nm

Table 6: The fitted parameters for all three 00*l* refinements are listed with their associated errors (given in parenthesizes). Criteria related to the quality of each structural refinement are compared to the values obtained from LeBail fits.

	$[(PbSe)_{1.00}]_1[MoSe_2]_1$	$[(PbSe)_{0.99}]_1[WSe_2]_1$	$[(SnSe)_{1.03}]_1[MoSe_2]_1$
c (nm)	1.2658(2)	1.2697(3)	1.2425(6)
T	0	0	0
Se1	0.1195(2)	0.1110(4)	0.127(15)
M	0.3813(4)	0.3892(5)	0.380(28)
Se2	0.4011(6)	0.4057(2)	0.409(53)
Uiso ($Å^2$)	0.125(2)	0.079(4)	0.117(2)
Occupancy T/M2	0.85(5)/0.17(5)	1.0	1.0
Occupancy Se1	1	1	1
Occupancy M	0.5	0.5	0.5
Occupancy Se3	0.5	0.5	0.5
Model Fitted wrp	0.154	0.179	0.263
Lebail Fitted wrp	0.147	0.178	0.237
Model Fitted Rp	0.097	0.116	0.176
Lebail Fitted Rp	0.084	0.115	0.147
Model Bknd wrp	0.132	0.158	0.278
Lebail Bknd wrp	0.123	0.156	0.246
Model Bknd rp	0.090	0.107	0.163
Lebail Bknd rp	0.075	0.106	0.133
Model Dwd	0.078	0.085	0.220
Lebail Dwd	0.085	0.089	0.252
Model χ^2	7.14	34.4	11.2
Lebail χ^2	6.53	33.9	8.89

for $[(SnSe)_{1.03}]_1[MoSe_2]_1$. These values are at the lower end of the magnitude of this distortion, 0.020 nm to 0.060 nm, in the relatively few atomic level structures that have been previously determined.[12, 30-36] The distance between the lead atom of one *00l* plane to the Se atom in the second *00l* plane of the bilayer of the distorted rock salt is 0.275 nm in $[(PbSe)_{1.00}]_1[MoSe_2]_1$ and 0.260 nm in $[(PbSe)_{0.99}]_1[WSe_2]_1$, which is considerably shorter than the 0.306 nm observed in PbSe. The distance from the tin atom of one *00l*

plane to the Se atom in the second *00l* plane of the bilayer is similar to the lead distances, 0.260 nm. The distances between the M cation of the rock salt layer and the Se anion of the dichalcogenide was found to be considerably longer, 0.346 nm in $[(PbSe)_{1.00}]_1[MoSe_2]_1$, 0.363 nm in $[(PbSe)_{0.99}]_1[WSe_2]_1$, and 0.33 nm in

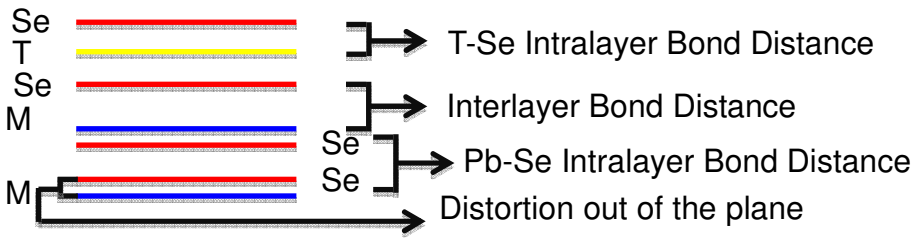

Figure 8: A schematic of the position of atomic planes along the c axis in the misfit compounds. The distances determined from the x-ray diffraction refinements for each of the compounds are given in Table 3. The half occupancy of the M and Se positions of the rock salt component in the refinements results from the correlated alternate occupancy of sites.

$[(SnSe)_{1.03}]_1[MoSe_2]_1$. The short M-Se distance in the rock salt constituent and the longer M-Se distance to the Se of the dichalcogenide is consistent with prior crystal structures of lead and tin containing misfit layered sulfides as summarized by Wiegers.[26] The distance

Table 7: **The distances between planes defined in Figure 8 are calculated from atomic coordinates resulting from the refinement of the *00l* diffraction scans. The uncertainty in the distances is given in parentheses**

	$[(PbSe)_{1.00}]_1[MoSe_2]_1$	**$[(PbSe)_{0.99}]_1[WSe_2]_1$**	**$[(SnSe)_{1.03}]_1[MoSe_2]_1$**
Distortion of rock salt structure out of the plane	0.023(1)	0.021(1)	0.036(5)
M-Se intralayer distance	0.275(8)	0.2583(9)	0.26(6)
MSe-TSe_2 interlayer distance (nm)	0.346(3)	0.364(1)	0.33(5)
T-Se intralayer distance	0.156(1)	0.141(1)	0.16(2)

between the metal layer and the selenium layers in the Se-T-Se trilayers are considerably shorter in the lead containing compounds than in the tin compound. They are also considerably shorter than observed in the binary compounds $MoSe_2$ and WSe_2. From the 00l data alone it is not possible to determine whether the coordination of the transition metal is trigonal prismatic as in the binary compounds or octahedral.

In $[(PbSe)_1]_{1.0}[MoSe_2]_1$ we observed that allowing Pb to substitute for Mo in the $MoSe_2$ layer to the amount of 17% +/- 5% improved the structural model. Such a large substitution seems unlikely because Pb and Mo have different coordination chemistries. The magnitude of this substitution, which can be thought of as an attempt of the refinement to increase the electron density within the $MoSe_2$ layer, may result from a substitution of PbSe into small sections of the $MoSe_2$ layer as seen in Figure 6, the STEM image of this material. Further investigations into the extent of these substitutions as a function of composition will be needed to understand this phenomenon.

Refinement of the projection of the constituent structures on the a-b plane using the intensities of the *hk*0 reflections was completed on a $[(PbSe)_{1.00}]_1[MoSe_2]_1$ sample. The data contains four reflections attributable to PbSe and three reflections attributable to $MoSe_2$ as shown in Figure 9. The refinement model used separate rock salt PbSe and dichalcogenide $MoSe_2$ constituents, with a preferred orientation parameter for both phases to account for the lack of reflections involving *l*. The rock salt phase was refined using planar symmetry. The dichalcogenide phase was refined with the same space groups as the bulk analog. The $MoSe_2$ refinement used the space group $P6_3/mmc$ with both Mo and Se on the special positions as found in the binary compound. The rock salt phase was refined as a P 2 3 space group in order to reflect the symmetry of the a and b

planes irrespective of the position of the atoms in the c plane. The unit cell was refined with 8 edge atoms in 4 positions with ½ Pb and ½ Se with a z = 1. Pb and Se were placed, both occupying the special position 0, 0, 0 each with half occupancy. The site occupancies and isothermal parameters were not refined, limiting parameter, which

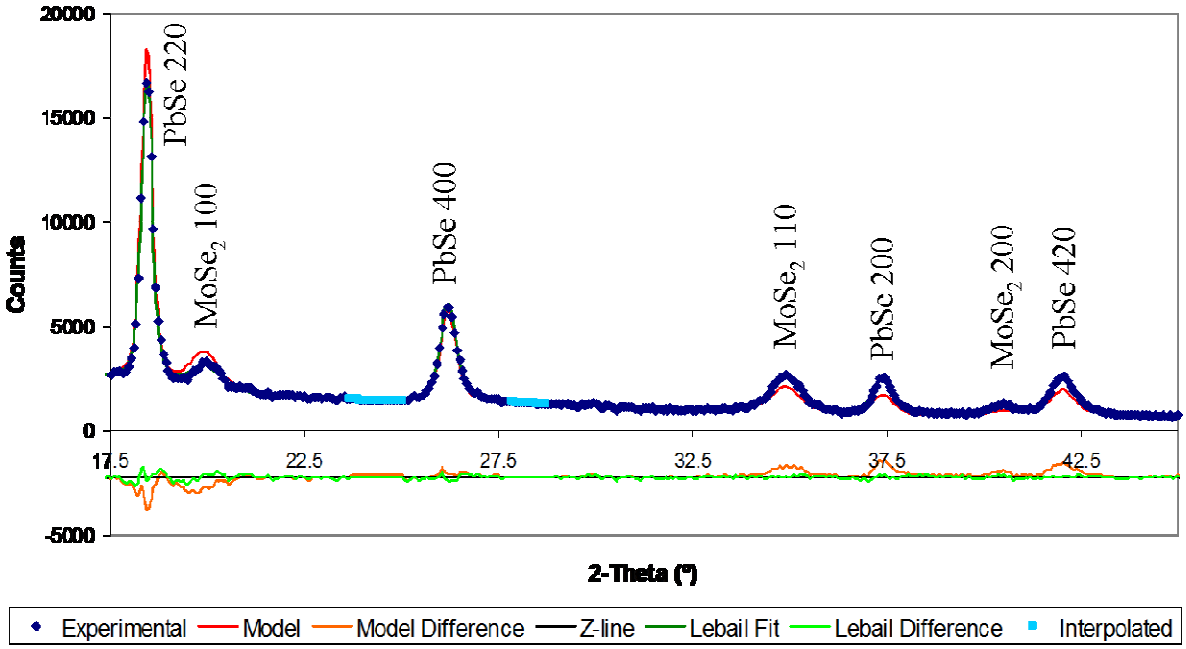

Figure 9: Rietveld refinement of $[(PbSe)_{1.00}]_1[MoSe_2]_1$ where PbSe and $MoSe_2$ were independently refined as described in the text. The scan also contained Al_2O_3 stage reflections, which were extracted and the base line data interpolated.

refined to the highest possible value indicating that the sample is oriented with layering perpendicular to the substrate. The agreement between this simple model and the data is consistent with lattice misfits in both the a- and b-axis lattice parameters, with both structures having the average symmetry and average fractional atom positions expected from the binary compounds.

3.4: Conclusions

All of the samples investigated showed a strong preferred orientation which enabled us to derive the position of atomic planes along the c axis for all of the compounds and the projection of the structures of the components onto the ab plane for $[(PbSe)_{1.00}]_1[MoSe_2]_1$. The two constituents are incommensurate in both a and b lattice parameters, but are crystallographically oriented with respect to one another, with the a-b plane of the rock salt structure parallel with the a-b plane of the dichalcogenide. The misfit parameters, δ, calculated for each material from the refined lattice parameters, are the smallest values ever reported, including the first negative value. The lack of *hkl* supercell reflections and the asymmetry of the *hk0* reflections in the grazing incidence data sets are consistent with turbostratic disorder, as the samples lack rotational or translational symmetry between layers. In this regard they differ from previous structural reports of misfit compounds, which have an orientational relationship between the constituents enabling the structure to be described using a modulation vector(s). The inter plane distances derived from the refinement of atomic planes along the c axis yield short M-Se distances within the rock salt constituent and longer M-Se distances to the Se of the dichalcogenide, consistent with prior crystal structures of lead and tin containing misfit layered sulfides.

3.5: Bridge

This chapter deals with establishing the one-dimensional refinement techniques used for this work. The refinements are of m = n = 1 compounds, the kind found most frequently in the structural literature. The following chapter deals with extending the techniques used here to a series of isomer samples, materials that could not have been

made prior to the use of MER to make MLCs. This should bring out effects caused by the interface between the two materials and the forces stabilizing the formation of these compounds.

CHAPTER IV

RIETVELD REFINEMENT OF $[(PbSe)_{0.99}]_m[WSe_2]_m$ ISOMER SERIES, m = 1 TO 5

Samples in this study were made by Dr. Qiyin Lin with the assistance of Benjamin Silver, Logan LaRossa, Paul Hansen, and Johnathan Hanni. X-ray diffraction data taken at the advanced photon source were done in collaboration with Dr. Paul Zschack and Dr. Evguenia Karapetrova who administer beamlines 33 and 34. The samples were run by myself, Dr. Colby Heideman, Dr. Qiyin Lin, Dr. Ngoc Nguyen, Raimar Rostek, and Dr. Clay Mortenson. The space group used for the 00*l* refinements was first used for this purpose by Dr. Arwyn Smalley and Fred Harris for $[(Bi_2Te_3)_{1.36}]_x[TiTe_2]_y$ superlattice samples. Dr. Angus Wilkinson helped them to develop this method of refining 00*l* data. The use of LeBail fits was suggested by Dr. Brian H. Toby. The STEM-HAADF image was measured by Michael D. Anderson in collaboration with Ian M. Anderson at NIST. I completed all of the Rietveld refinements found in this chapter as well as the subsequent data analysis. I wrote the text of this chapter.

4.1: Introduction

Theoretically it is possible to make misfit layered compounds (MLCs), $[(MX)_{1+\delta})]_m[TX_2]_n$, where M is a metal, X is a chalcogen, T is a group III, IV, or V transition metal, δ is the misfit parameter, and m and n are the number of layers of each component with any value of m and n. It was hypothesized that systematic changes to the structure of these compounds based on the number of m and n layers should occur.

Structural changes lead to changes in the physical properties of a given material, which is desirable for a variety of real world applications like thermal barriers,[1] computer chips,[2] and alternative power sources.[3-5] Using the traditional technique of vapor transport, samples have been made with varying numbers of layers and take the general form $[(MX)_{1+\delta}]_m[TX_2]_n$, where m = 1, 1.5, or 2 and n = 1 - 4 but m and n were never both > 1.[6-8] This limited selection does not approach the variety that is theoretically possible in these systems.

Instead, misfit layered compounds (MLCs) have primarily been made as samples with m = n = 1.[6, 8] Materials of this general form have exhibited a wide variety of physical properties; superconducting,[6-12] antiferromagnetic,[7] ferromagnetic,[6-8] paramagnetic,[8, 13] low thermal conductivity,[14, 15] semiconducting electrical conductivity,[6, 7] and metallic electrical conductivity.[6, 8] The properties of a material are the result of the structure and the composition. Most MLCs have the same basic structure, a distorted rock salt interleaved with an octahedrally coordinated dichalcogenide, with differences in misfit value, -0.1 to 0.28,[14, 16-22] arising from composition differences. The properties of a MLC are strongly compositionally dependent because composition determines the electrical bands of the resulting MLC.[7]

Synthesis of a series of MLCs with m, n = 1 to 8 became possible using the MER synthesis technique, and have been made and characterized by Qiyin Lin and Colby Heideman.[23-25] These families of MLCs have extremely low thermal conductivity[15] and exhibit metallic conducting behavior.[26] These samples have strong preferred orientation and are turbostratically disordered. These properties make them difficult to structurally characterize. This chapter will address the 00*l* Rietveld refinement of

isomeric $[(PbSe)_{0.99}]_m[WSe_2]_m$ samples. Because structural data on an isomeric series could not have been generated prior to this work, the refinements contained herein required the use of several approximations based on various hypotheses about their possible structure.

4.2: Experimental

The samples were made using the MER technique in a process described in detail elsewhere.[25] X-ray diffraction patterns of $[(PbSe)_{0.99}]_1[WSe_2]_1$, $[(PbSe)_{0.99}]_2[WSe_2]_2$, and $[(PbSe)_{0.99}]_4[WSe_2]_4$ were measured using the type A undulator source 33ID beam line of the Advanced Photon Source (APS) at Argonne National Laboratory (ANL). Samples were mounted for measurement on a 6-circle Huber goniometer in a Bragg-Brentano geometry with the sample aligned in the cross plane. The energy of the incoming beam was tuned using a Si(111) double-crystal monochromator. Dynamically bent mirrors were used for harmonic rejection and vertical focusing; while sagitally bent Si crystals provided monochromatic x-rays with narrow band-width and horizontal focusing. Slits, ion chambers, and beam position monitors permit dynamic feedback control and x-ray beam monitoring to produce brilliant, stable x-ray beams suitable for diffraction, scattering, or imaging applications.[27] Incidence slits were set to a height of 0.9 mm and a width of 0.5 mm. Anti-scatter slits were set to a width of 10 mm and a height of 3 mm. The detector slits were set to a width of 0.5 mm and height of 3 mm.

$[(PbSe)_{0.99}]_1[WSe_2]_1$ and $[(PbSe)_{0.99}]_2[WSe_2]_2$ were scanned above and below the Pb L_3 absorption line with wavelengths of 95.78 pm and 94.29 pm using 0.005˚ steps with a 1 second count time. $[(PbSe)_{0.99}]_4[WSe_2]_4$ was measured below the Pb L_3 absorption line with a wavelength of 95.24 pm using a 0.019˚ steps with a 1 second

count time. Data for the $[(PbSe)_{0.99}]_3[WSe_2]_3$ and $[(PbSe)_{0.99}]_5[WSe_2]_5$ samples were collected on a Bruker D8 Discovery system in a Bragg-Brentano geometry with a Cu K_α source, 154 pm, with 0.001˚ steps with a 1 sec count time. A 0.6 mm anti-scatter slit was used with 1 mm incidence and detector slits to focus the beam.

Due to the strong texturing of these systems as established in Chapter 3, only the 00*l* reflections are present in these scans. This means that these refinements are a partial structural solution for these materials. Further analysis using other scans and techniques, including scans of the *hk*0 reflections taken using an incident angle geometry, area detector scans, and STEM, is required to fully structurally characterize these samples but is beyond the scope of this current work. The cross-plane positional data was refined using the Rietveld refinement method as applied in the General Structure Analysis System (GSAS) program.[28, 29]

Refinements can be completed on multiple data sets at once, with various constraints both soft and hard depending on the users' needs. The software includes a comprehensive error analysis packaged for all refinable parameters. In the case of these data sets, the synchrotron based corrections (zero correction and instrument parameters) were used for synchrotron data and the lab diffractometer settings (shift correction and instrument parameters) were used for lab data. Simultaneous refinements were done of the anomalous scattering scans. Various soft constraints were used at different points in the refinement. Finally, LeBail fits were employed as a method of reducing the error of the systems as well as providing a stopping point for each refinement.

4.3: Refinement Procedures

The isomeric series $[(PbSe)_{0.99}]_m[WSe_2]_m$ where m = 1 to 5 was structurally refined in the 00*l* direction using Rietveld refinement. Each sample was treated using the $P\bar{3}m1$ space group, with the unit cell size increasing by 1.277 nm for each successive isomer and more atoms being added as more layers were added. Each reported refinement is the combination of multiple refined models that were obtained from refining various starting models. This technique was necessitated by the relatively sparse number of reflections available relative to the number of parameters refined. This tactic increased the quality of the final result and enabled more detailed error analysis for each refinement.

The thin films in this study are highly smooth, resulting in the presence of Kiessig fringes, a front to back reflection arising from the beam penetrating the entire thin film sample, at angles up to 30˚ 2-θ. The GSAS program does not model Kiessig fringing; therefore, LeBail fits were used to reduce the correlation effect of this peak overlap.[30] LeBail fits refine the following parameters; the unit cell size, instrument corrections, peak profile and background parameters. The peak shape, background, and unit cell size refined using the LeBail fit of each scan were used as a starting point in the subsequent Rietveld refinements of that scan. The fitted and background w_{rp} and r_p, as well as the Durban-Watson statistic and the χ^2 from the LeBail fits were compared to the error parameters of each Rietveld refinement in order to determine the relative quality of each refinement.

Figure 10 is representative example of the effect of Kiessig fringing on the overall fit of a peak. Notice the difference between the model and the experimental data

undulates at the same frequency as the Kiessig fringing. This illustrates that the model does not include Kiessig fringing. It also shows how Kiessig fringing causes the error values in these fits to be higher than in analogous refinements without Kiessig fringing. The Dwd parameter, which measures correlation between data points does not approach two as it should as a result. It is generally much lower in these samples.

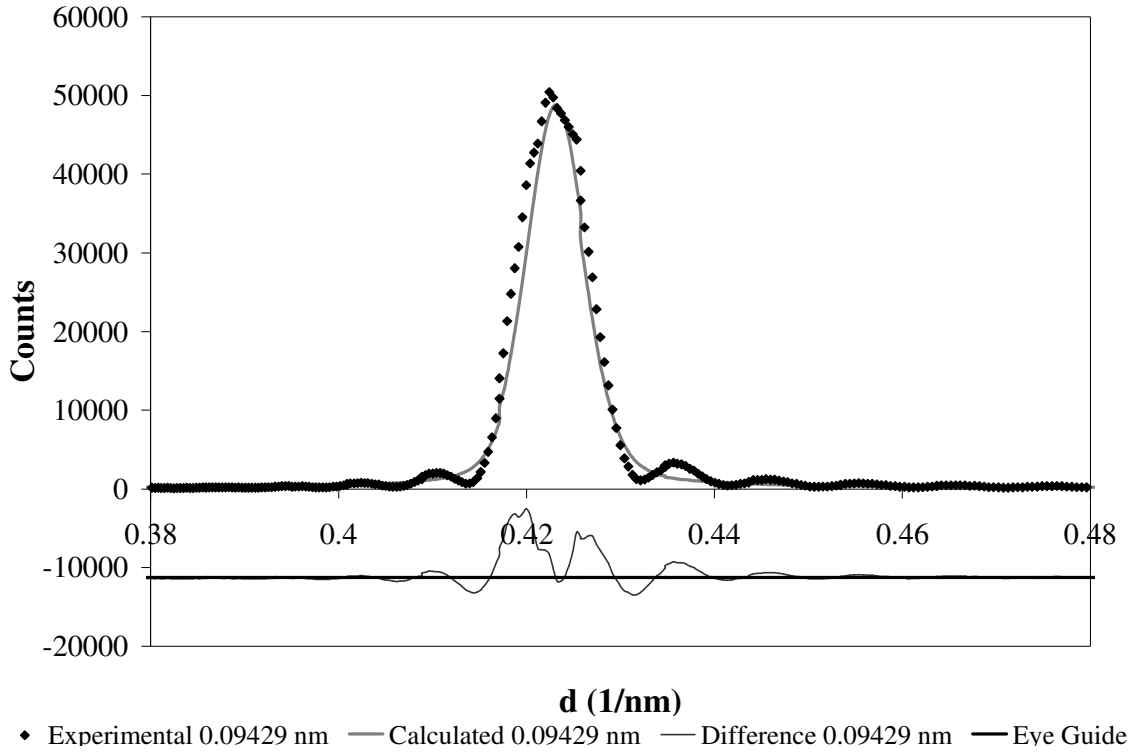

Figure 10: Graph highlighting the fit of a peak in the $[(PbSe)_{0.99}]_1[WSe_2]_1$ sample. This peak has Kiessig fringing on both sides. The model does not include the Kiessig fringing phenomenon, so the difference data undulates with the Kiessig fringing. Peak profiles were fit to give the best possible match in the system despite the interference of the fringing.

The misfit parameter of the MLC component layers was accounted for by setting the rock salt atom occupancies to 0.5 and the dichalcogenide atom values to 1.0, which within error represents the ratio of 0.99:1. This parameter was determined from *hk*0 reflections in scans taken using grazing incidence geometry to probe the structure parallel to the substrate at APS. A detailed explanation of this procedure is found in chapter 3.

Scans of a variety of layering systems were performed and no difference was seen in the position of the *hk*0 reflections as a function of layering.[25] Therefore, the same misfit value, 0.99 was used for all of the refinements in this study.

The number of refinable parameters in the models was reduced by setting the isothermal parameter for all atoms to the same value, a soft constraint. This approximation is used because, while the isothermal parameter is normally the summation of data for each atom in all directions, this determination is not possible with these data due to the strong preferred orientation. The simplification provided by making these values equal not only reduces the number of refinable parameters but also represents the condensation of the multi-directional data into one dimension that occurs when doing these refinements.

In order to determine the positions of each atom in the unit cell, the literature was combed for similar examples. The general structures of the component materials were found[31, 32] and used along with several assumptions to produce starting models. It is well documented that in MLCs the rock salt distorts with the magnitude of 20 pm to 60 pm. [17, 18, 20-22, 33, 34] It was also found that the dichalcogenide layer does not change significantly when placed in an MLC in both m = n = 1 samples and m = 1, n = 2 or 3.[6, 7] Because an isomeric series had never been made before these samples, there is no literature precedent on how the structure changes as both component layers get thicker. In order to create models which would evolve with the number of layers, it was therefore necessary to posit several hypotheses about how the isomer system would change.

The stability of these compounds and the distortion of the rock salt are attributed to charge transfer between the layers, rock salt donating electron density to

dichalcogenide.[16, 35-40] It is believed that the major changes in the structure will be in the electron donating layers. The rock salt distortion could decrease toward the center of the each rock salt layer as the energy cost of distorting each successive layer will increase for each additional layer and the amount of charge transfer in an isomeric system should not change significantly from sample to sample. Models were, therefore, given gradual tapering of the distortion parameter. Concurrently, the magnitude of the distortion could decrease with an increasing number of layers because of the same reason it was modeled as 0 pm, 20 pm, 40 pm, and 80pm. It is also possible that there would be slight changes in the dichalcogenide layer as a result of increasing the number of layers.[11, 41, 42] Based on the literature this was thought to be a small effect and was modeled as 0.15 nm or 0.16 nm. Finally, the average distance between the rock salt and dichalcogenide layers was estimated by using the van der Waals gap of the dichalcogenide and subtracting ½ the rock salt distortion magnitude used in a given model. From these general parameters multiple models were generated combining the possibilities based on the assumptions above.

Each refinement was completed by releasing the parameters for refinement in the following order, unit cell size, profile fit, instrument parameters, background fit, scaling factor, Pb positions, W and Se positions, and universal isothermal parameters (U_{iso}). The first four parameters released were done in the LeBail fit. The rest were completed in the Rietveld portion of the refinement. Releasing the parameters in any other order caused the system of equations used for refinement to diverge. Refinement equations diverge when too many parameters change simultaneously with equal weight in the refinement.

Some parameters affect the fit more than others and the order in which these variables are refined reflects that.

Refinements steps resulting in non-physical values for various parameters were reverted to a previous point in the refinement and forced into a new direction using soft constraints. For example, if U_{iso} became negative, which is physically impossible as it represents the overall thermal movement of the atoms with no directionality, the values were returned with in the program to the starting values and refined again using a high damping parameter in order to decrease the chance of the same problem recurring. This usually solved the problem. If not, the refinement was reset to a previous refinement stage. For the above example the previous refinement step is atom position. More damping parameters were added when refining the atom positions. If that did not work, the refinement from that particular starting model was rejected and not used in the average reported in the summary table for that refinement.

During the refinement process it became evident that the rock salt layers had not only had an interface distortion but a layer modulation. From this point forward, these phenomena will be referred to as the puckering distortion and the rock salt distortion. Both the puckering and rock salt distortion are represented in Figure 10. The image is the combination of x parameters obtained by taking educated guesses based on unit cell parameters of the unit cell and the z coordinates of the rock salt portion of the $[(PbSe)_{0.99}]_4[WSe_2]_4$ sample based on the 00*l* refinement. The rock salt puckering is apparent at the ends of the PbSe layer, at the interface with WSe_2, which is on either end of the presented rock salt layers in the z direction. The Se atoms, represented by the lighter grey spheres, are repulsed at the interface while the Pb, the darker grey spheres, is

attracted to it. The rock salt distortion is evident in how the rock salt layers seem to pair off so that every other bond distance is shorter than the next. This pattern appeared in all of the refinements where m > 1.

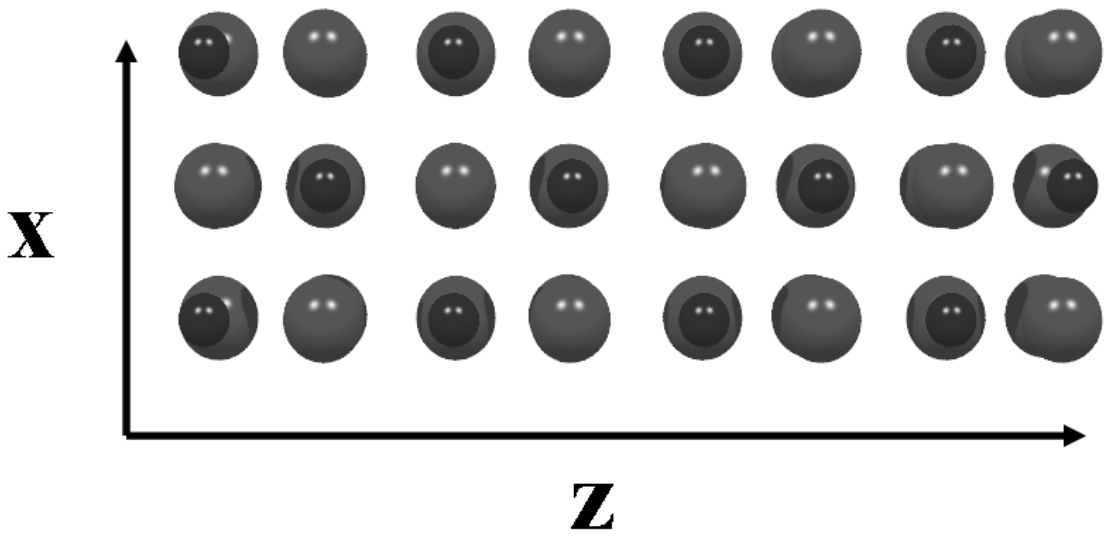

Figure 11: The PbSe portion of $[(PbSe)_{0.99}]_4[WSe_2]_4$ represented to scale in the z coordinate and with spacing similar to that found in the $[(PbSe)_{0.99}]_1[WSe_2]_1$ sample in the x and y directions. Pb is represented as dark grey and Se as light grey. The rock salt puckering is visible at the ends of the PbSe section, the interface with WSe_2 (not pictured). The Pb atoms are attracted to the WSe_2 layer while the Se atoms repelled by the WSe_2 layer. Also note another rock salt distortion; there are two different plane to plane distances which alternate.

New models were created for all of the samples, using the refined values of W-Se distance and WSe_2 van der Waal gap from the previous models but containing varying amounts of rock salt distortion, starting with a layer to layer distance discrepancy of 50 pm for the $[(PbSe)_{0.99}]_2[WSe_2]_2$ sample down to a discrepancy of 20 pm for the $[(PbSe)_{0.99}]_5[WSe_2]_5$ sample stepping down by 10 pm. The refinements from these models were combined with the refinements from previous starting models to give the final answer reported in this work. The summary of each of these refinements will be presented in a table that includes all the refinements that converged for a given sample. The error values reported are the estimated standard deviation values calculated by the

GSAS program. This error was propagated using a weighted average to give the error values on the average positions. The starting models used in these refinements can be identified by the label in the summary table. A collection of all of the starting models used for the refinements in this work is located in Appendix B.

4.4: Format of Refinement Results

Rietveld refinements are reported by crystallographers as a list of fractional coordinate values for each atom in the refinement and in some cases with full 3-D ball and stick representations. The results of these refinements will be given as fractional coordinate lists and with 2-D graphical representations. The difference between these two types of graphical representations is given in Figure 12. Figure 12A, on the right, was used in Chapter 3 to represent the data learned from both the 00*l* and *hk*0 refinements combined with literature precedent as to how the subunits might align along the a/b plane. The refinements in this chapter are all 00*l* and, therefore, represent only the location of the atom planes along the c axis of the structure. There is no literature data for isomer samples with which to predict the a and b positions of the atoms, or how they would align with each other so a ball and stick representation of the data would be misleading. Figure 12B uses lines to represent each atom plane, and will be used instead of the ball representation in Figure 12A in order to more clearly represent what is and isn't known from these data sets. The numbers on the image are the distances between the atom planes determined from Rietveld refinement. In the case of the Pb/Se layers, an average position for each layer was taken and used to determine the distance between that atom plane and other atom planes. The ε represents the magnitude of the puckering in the rock salt plane. This is graphically designated by the splitting of the dark gray line into

two lines, with the Se line black and the Pb line light gray. In the case of samples with many Pb/Se layers the ε is numbered with a subscript for ease of reference.

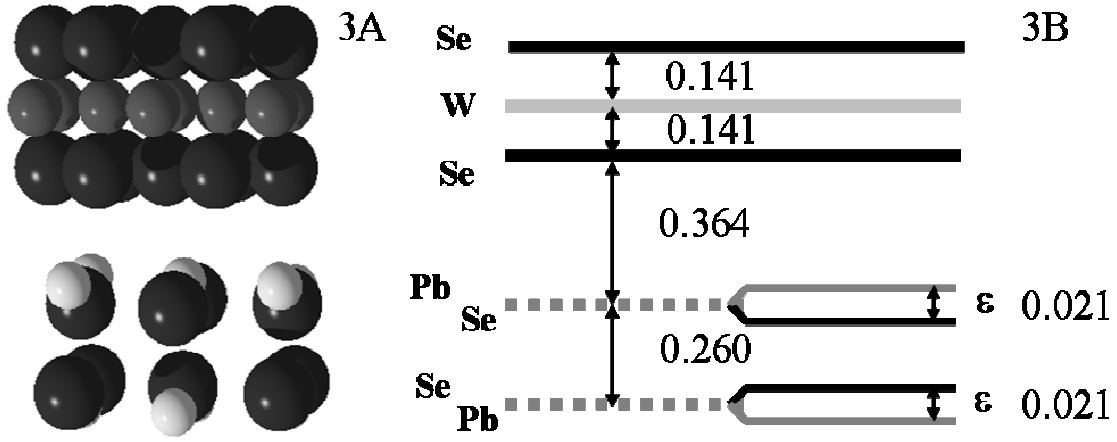

Figure 12: Two different representations of refinement results for the $[(PbSe)_{0.99}]_1[WSe_2]_1$ system. The representation on the right uses balls to represent the atoms and represents the 00l and hk0 refinements of the $[(PbSe)_{0.99}]_1[WSe_2]_1$ in the previous chapter. The representation on the right is a more accurate depiction of what is learned from an 00*l* refinement because the atoms are represented by planes. The distance between the planes (in nm) is labeled on the graph and in the case of the Pb/Se layer the difference from the average position of one layer of atoms to the average position of the next is given. The ε represents the amount of puckering in the rock salt layer, the magnitude of which is graphically represented by splitting the line into two with black representing Se and grey representing Pb. The depiction on the right will be used to report all structures refined in this chapter.

4.5: $[(PbSe)_{0.99}]_1[WSe_2]_1$ Refinement

Table 8 summarizes the refinements that contributed to the final result. There were six separate starting models that converged and were used to find the average positions reported in Figure 13. The values reported are fairly consistent from refinement to refinement. This result indicates that a variety of different refinement paths produce the same basic model fit when refined based on the same LeBail fit.

The error in the unit cell size is larger, in some cases, than in the position of the atom. The unit cell size is calculated from every peak and is described by more Fourier components than the individual atoms. The improved statistics should produce greater

accuracy and consequently lower estimated standard deviation values, but because they do not there must be something else limiting the accuracy of the calculation. This same phenomenon was observed in one of the Rietveld round robins done by the International Union of Crystallography.[43] It was attributed to the instrumental correction parameters and the signal to noise threshold used for the peak fitting both of which can alter the results of the refinement. The large peak widths in these data make discernment of the peak and background data difficult. The range of refined positional values possible was explored by completing the refinement procedure using more than one LeBail fit of this sample. With the same peak threshold parameters, the variation in the measurement is +/- 2 pm of a given value for APS refinements of this type.

The LeBail fit used in each refinement was chosen because it was the most probable answer. The fits chosen had the lowest instrumental correction, indicating good instrumental alignment. It was assumed that because the alignment procedure is a well established and studied technique, the alignment is reliable. Therefore, fits with extremely large correction parameters were deemed unlikely.

In high resolution instruments, the Lorentzian component from the sample tends to dominate the peak shape and requires a lower peak fitting threshold in order to accurately determine peak vs. background. In these samples the peak fitting threshold was set to 0.5% of the total peak height in order to improve accuracy. Sample broadening is the largest portion of peak broadening based on comparisons of reflections from Si vs. our samples (based off of substrate peaks which show themselves in certain sample orientations). The Si reflections are much narrower than the sample reflections. Sample peak broadening can be due to the finite size of the sample, the distribution of

Table 8: Summary of refinements for the $[(PbSe)_{0.99}]_1[WSe_2]_1$ sample. The sample converged for six different starting models. The error values reported for the overall refinement are given above the rest of the results.

		Lebail Fitted w_{rp} = 0.1801	Lebail Fitted rp = 0.1187	Lebail Background w_{rp} = 0.1599	Lebail Background rp = 0.1098	Lebail Dwd = 0.084	Lebail χ^2 = 34.88	
	c = 12.6968(3)	Fitted w_{rp} = 0.1799	Fitted rp = 0.1174	Background w_{rp} = 0.1580	Background rp = 0.1084	Dwd = 0.085	χ^2 = 34.37	
Atom	A	B	C	D	E	F	Average	Layer to Layer (nm)
W1	0(0)	0(0)	0(0)	0(0)	0(0)	0(0)	0(0)	0(0)
Se1	0.11097(16)	0.11097(16)	0.11097(16)	0.11097(16)	0.11097(16)	0.11097(16)	0.11097(4)	0.14089(3)
Pb1	0.3892(40)	0.3892(40)	0.3892(40)	0.3892(40)	0.3892(40)	0.3892(40)	0.3892(27)	0.3533(3)
Se2	0.4057(14)	0.40571(14)	0.4057(14)	0.40572(14)	0.4057(14)	0.4057(14)	0.4057(8)	0.3742(1)
Uiso	0.0788(11)	0.0788(11)	0.0788(11)	0.07967(110)	0.0788(11)	0.0788(11)	0.0789(2)	0.2604(5)

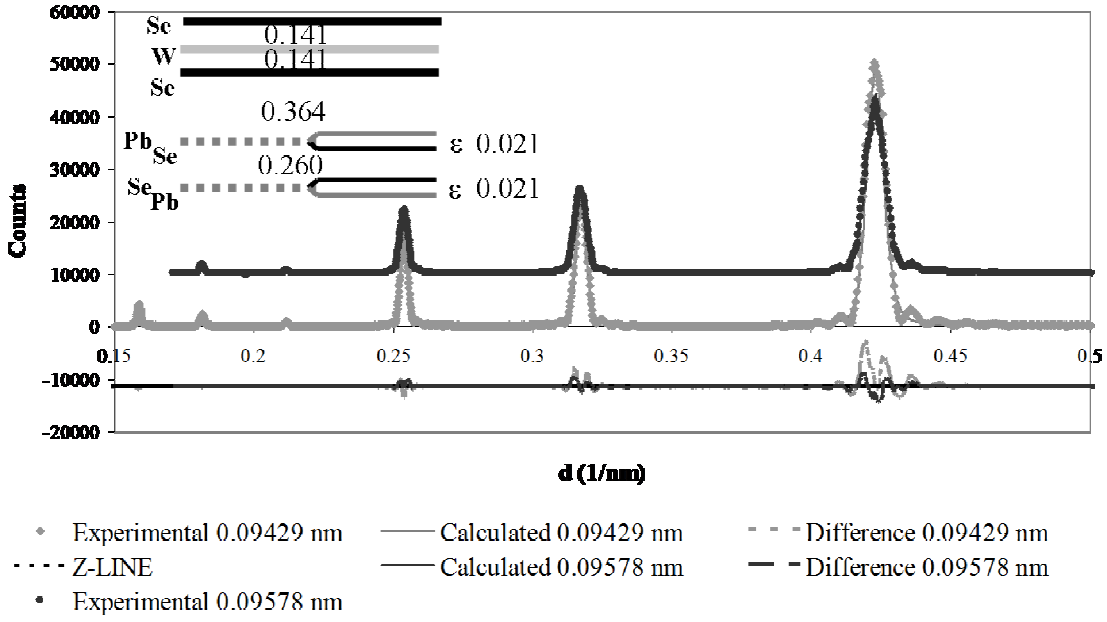

Figure 13: A line diagram of refinement results for $[(PbSe)_{0.99}]_1[WSe_2]_1$ was overlaid on the graph of the refinement fit. This is an anomalous scattering fit done using APS data above and below the Pb L_3 absorption edge.

grain sizes in the sample, strain broadening, and stress broadening. Most of these phenomena contribute to the Lorentzian terms to the line broadening and some contribute Gaussian terms. This information influenced the order of refinement for the Gaussian and Lorentzian parameters of the fit, but, ultimately, the LeBail fit with the lowest occurrence of systematic error in peak fitting as seen in the difference line was used for the subsequent refinements.

The refinement of $[(PbSe)_{0.99}]_1[WSe_2]_1$ is shown in Figure 13. This scan contained Kiessig fringing throughout the majority of the scan indicating the sample was quite smooth. The W-Se distance refined in this sample is lower that expected, however, it was a consistently lower value no matter the starting point of the refinement as can be see in Table 8. It can be inferred from the alteration in the W-Se distance and the large

interfacial distance of 0.364 nm implies that there is quite a bit of charge transfer between the rock salt and dichalcogenide layer in this sample. The puckering distortion of 21 pm is well within the expected values seen in literature. The 0.260 nm distance between the rock salt layers is a bit smaller than the ~0.32 nm that would be expected but this type of discrepancy is seen in a variety of other refinements in similar systems as can be observed in Table 9. Sometimes these differences result in larger rock salt layer to layer distances and sometimes smaller.

Table 9: Comparison of the layer to layer distance in other rock salt misfit layered compounds vs. bulk binary layer to layer distances

Compound	spacegroup	00l Δ	MLC 00l Δ	diff	References
CeS	Fm3m	0.2889	0.285	0.004	[44, 45]
GdS	Fm3m	0.2773	0.275	0.002	[46, 47]
LaS	Fm3m	0.2927	0.290	0.003	[33, 48]
NdS	Fm3m	0.2844	0.285	-0.001	[47, 49]
PbS	Fm3m	0.2962	0.285	0.011	[50, 51]
SmS	Fm3m	0.2981	0.280	0.018	[52, 53]

4.6: $[(PbSe)_{0.99}]_2[WSe_2]_2$ Refinement

The $[(PbSe)_{0.99}]_2[WSe_2]_2$ data is composed of the results from five refinements. This sample was not as smooth as the $[(PbSe)_{0.99}]_1[WSe_2]_1$ sample, so there was less Kiessig fringing contribution to the error of the overall fit, which shows itself in the D_{wd} term of the error reported because D_{wd} describes correlation between points. A representative refinement is shown with a simplified line diagram for the structure in Figure 14.

The summary values in Table 10 clearly show that this refinement is somewhat different from the previous one. The W-Se plane to plane distance, 0.156 pm, is ~10 pm larger than in the $[(PbSe)_{0.99}]_1[WSe_2]_1$ sample. The puckering at the interface is 91 pm,

which is quite large and the puckering in the next layer is 81 pm. These values are outside of literature precedent. The difference between the long and short plane to plane distances in between layers is also quite large.

4.7: $[(PbSe)_{0.99}]_3[WSe_2]_3$ Refinement

The copper refinement of $[(PbSe)_{0.99}]_3[WSe_2]_3$ includes seven component refinements, which are summarized in Table 11. As can be seen from the refinement graph in Figure 15, this scan has a lower signal to noise than the APS data discussed previously. The lower signal to noise results in the absence of well defined Kiessig fringing in the refined portion of the scan. This does not imply that the Cu scan results in better overall error values. The reverse is true because of the low signal to noise the background is harder to fit accurately as it contains more noise. The Cu scans are accurate to within +/- 5 pm based on refinements of three LeBail fits. This value fits with expectations. There is half the amount of data in this refinement compared to an anomalous scattering scan and it is of inferior resolution.

The W-Se plane to plane distances in this refinement are equal within the error expressed above. The average W-Se plane to plane distance is 0.162 nm. This is on par with the majority of the refinements in this series. The initial puckering of the rock salt layers in this sample is 10 pm, which is within the range of possible values but is much lower than the values obtained from the APS refinements. The puckering of the rock salt is the same throughout this sample within error. This result is not representative of a trend because of the high relative error in these values (~50%). The average long plane to plane distance in the rock salt is 0.336 nm and the average short plane to plane distance is 0.291 nm.

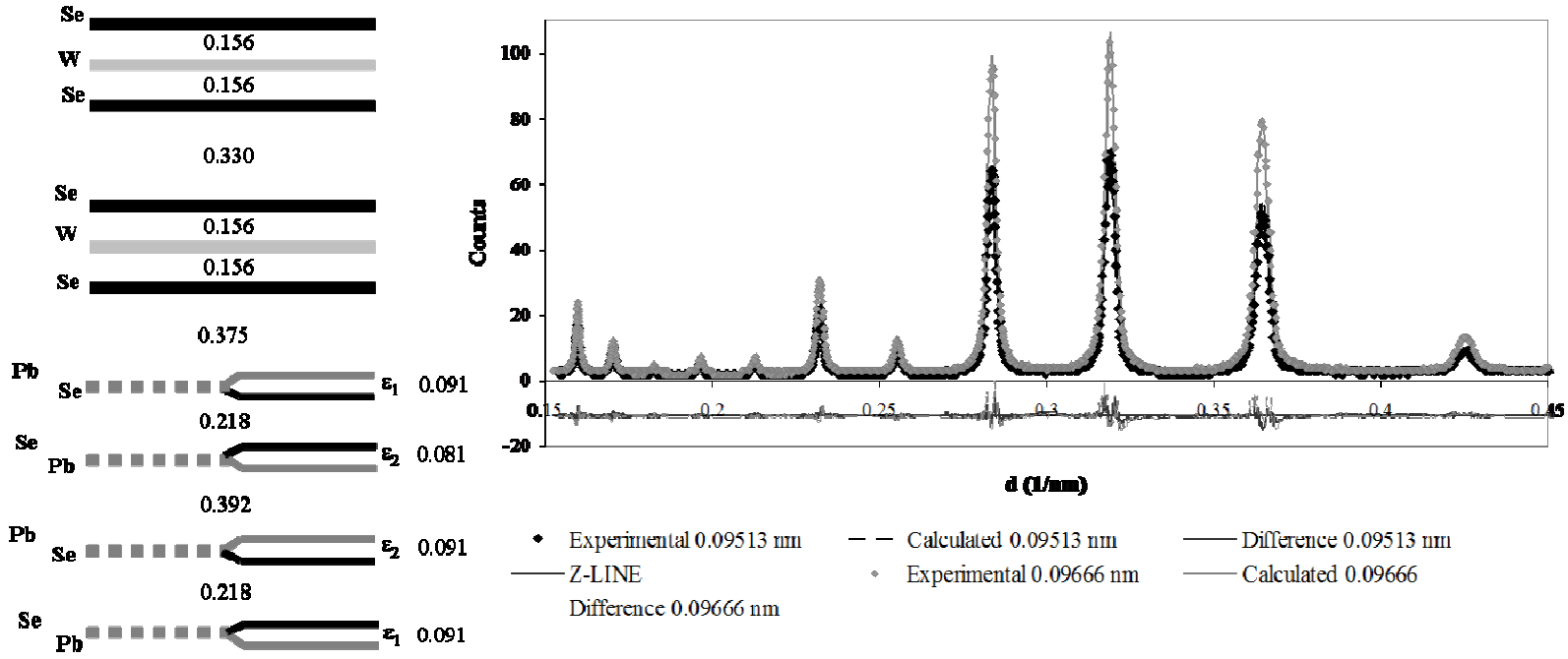

Figure 14: The line diagram representation of the data for the $[(PbSe)_{0.99}]_2[WSe_2]_2$ refinement is on the right and the Rietveld refinement fit of anomalous scattering data at the Pb L3 absorption edge is on the left.

Table 10: Summary of refinements for the $[(PbSe)_{0.99}]_2[WSe_2]_2$ sample. The sample converged five different starting models. The error values reported for the overall refinement are given above the rest of the results.

	c = 25.52856(4)	Lebail Fitted w_{rp} = 0.1051 Fitted wrp 0.1383	Lebail Fitted rp = 0.0808 Fitted rp = 0.1000	Lebail Background w_{rp} = 0.1118 Background wrp = 0.1181	Lebail Background rp = 0.0901 Background rp = 0.0918	Lebail Dwd = 0.328 Dwd = 0.141	Lebail χ^2 = 3.726 χ^2 = 7.212
Atom	A	C	D	E	F	Average	Layer to layer
SE1	0.06716(10)	0.06717(10)	0.06971(60)	0.06717(10)	0.06774(90)	0.06886(4)	0.1.758(0)
W1	0.12971(40)	0.12971(40)	0.129165(28)	0.12971(40)	0.12971(40)	0.12970(9)	0.1.5530(5)
SE2	0.1913(80)	0.1913(80)	0.1888(50)	0.1913(80)	0.19807(8)	0.19087(3)	0.1561(3)
PB1	0.31993(70)	0.31993(70)	0.32248(14)	0.31993(70)	0.32059(70)	0.3201(4)	0.3299(4)
SE3	0.35236(21)	0.35237(21)	0.35875(70)	0.35238(21)	0.35443(20)	0.3557(3)	0.4209(3)
PB2	0.44026(70)	0.44026(70)	0.43534(70)	0.44026(70)	0.4398(700)	0.4390(1)	0.2126(0)
SE4	0.41139(20)	0.41138(20)	0.39287(16)	0.41137(20)	0.40928(19)	0.4075(2)	0.2231(1)
Uiso	0.0946(60)	0.1370(9)	0.1654(13)	0.1008(11)	0.1008(11)	0.122(1)	

4.8: $[(PbSe)_{0.99}]_4[WSe_2]_4$ Refinement

The APS data in this refinement included only one energy and therefore produced less accurate results. Figure 16 shows the quality of the fit in this refinement. The Kiessig fringing in this sample was slight and only appears on the lower order reflections. The error on the refinement values is +/- 4 pm, larger than for the anomalous scattering refinements but smaller than the Cu refinements because the data has more favorable signal to noise. The starting models to this refinement converged four times as can be seen in Table 12.

The plane to plane distances in this refinement are consistent with the previous samples. The W-Se plane average distance is 0.163 nm. The individual values for the plane to plane distance of W-Se vary outside of the error expressed above. The higher values for the W-Se distance occur at the interface which may indicate an interface effect. The rock salt portion of the interface has a puckering of 20 pm at the interface, which is not outside of the expected value. In the inner rock salt layers ε_2, ε_3, and ε_4 is within error the same, virtually nonexistent. The rock salt distortion has a long Pb-Se distance is 0.315 nm and the short Pb-Se distance is 0.296 nm.

4.9: $[(PbSe)_{0.99}]_5[WSe_2]_5$ Refinement

This is another Cu refinement and therefore has an error of +/- 5 pm. It is composed of 5 contributing refinements as detailed in Table 13. As can be see in Figure 17, this sample does not have any Kiessig fringing in the refined portion of the data. This refinement is very similar to the one done on the $[(PbSe)_{0.99}]_3[WSe_2]_3$ system.

The refined parameters are somewhat inconsistent in this refinement. The average W-Se layer to layer distance is 0.162 nm, which is consistent with the other

Table 11: Refinement summary for the $[(PbSe)_{0.99}]_3[WSe_2]_3$ sample. There are seven contributing models presented. The error values for the overall refinement are located above the table.

		Lebail Fitted w_{rp} = 0.1116	Lebail Fitted rp = 0.0734	Lebail Background w_{rp} = 0.0977	Lebail Background rp = 0.0682	Lebail Dwd = 0.521	Lebail χ^2 = 4.052	
c = 38.2627(5)		Fitted w_{rp} = 0.2403	Fitted rp = 0.1724	Background w_{rp} = 0.2349	Background rp = 0.1699	Dwd = 0.111	χ^2 = 19.32	
Name	A	B	C	D	E	F	G	Average	Layer to Layer (nm)
W1	0	0	0	0	0	0	0	0	0
Se1	0.04278(6)	0.04253(5)	0.04246(5)	0.04248(5)	0.04232(6)	0.04253(5)	0.042595(5)	0.042519(6)	0.16266(5)
Se2	0.13059(6)	0.13075(5)	0.13076(5)	0.13081(6)	0.13088(5)	0.13076(5)	0.130727(5)	0.13075(17)	0.33766(5)
W2	0.172471(3)	0.17286(3)	0.172482(3)	0.172539(3)	0.172508(3)	0.172491(3)	0.172513(3)	0.172496(1)	0.15968(5)
Se3	0.21547(6)	0.21542(5)	0.21546(5)	0.21541(5)	0.21533(5)	0.21541(5)	0.21546(5)	0.21542(3)	0.16420(6)
Pb1	0.30151(3)	0.30127(2)	0.30195(4)	0.30082(1)	0.30046(9)	0.30122(2)	0.30119(4)	0.30106(3)	0.32767(5)
Se4	0.30246(8)	0.30341(56)	0.301484(5)	0.30488(3)	0.30589(2)	0.30358(5)	0.30347(5)	0.30350(4)	0.33750(5)
Pb2	0.37811(8)	0.37896(1)	0.37911(4)	0.37771(4)	0.38176(9)	0.37897(1)	0.377834(5)	0.37947(5)	0.29069(6)
Se5	0.37692(2)	0.37451(27)	0.37724(5)	0.3774(5)	0.37596(2)	0.37443(27)	0.37758(1)	0.3771(19)	0.29085(7)
Pb3	0.46064(4)	0.46023(4)	0.46244(4)	0.45929(4)	0.45911(4)	0.46009(4)	0.461781(4)	0.46030(45)	0.31844(5)
Se6	0.46168(1)	0.462875(5)	0.456374(5)	0.465671(5)	0.466225(5)	0.463253(5)	0.46247(4)	0.462525(4)	0.31774(5)
Uiso	0.0539(5)	0.0538(5)	0.0536(5)	0.0537(5)	0.0537(5)	0.0538(5)	0.0537(5)	0.05375(7)	

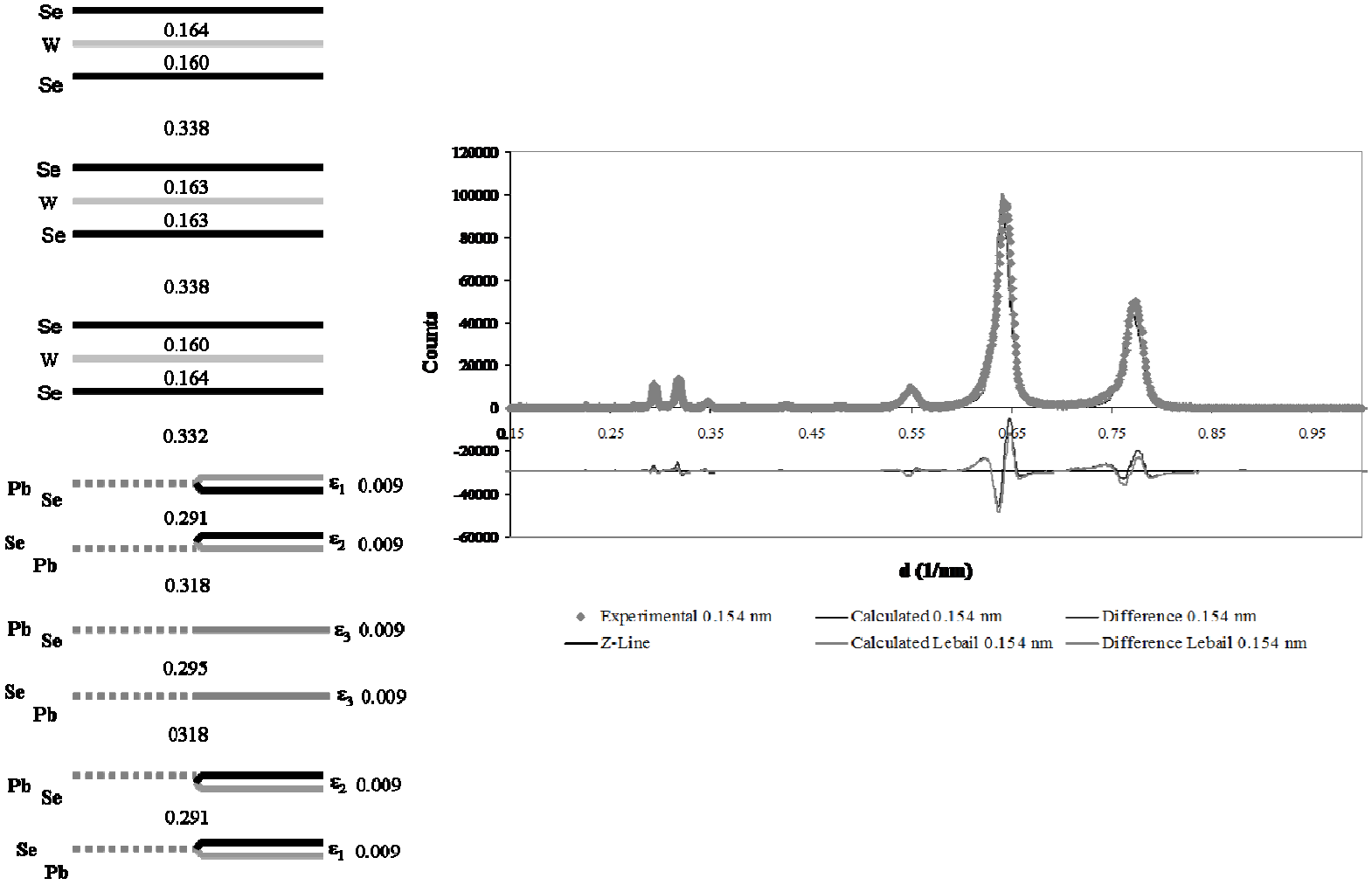

Figure 15: Line diagram of results of the $(PbSe)_{0.99}]_3[WSe_2]_3$ refinement and graph of the refinement fit to the Cu Kα data

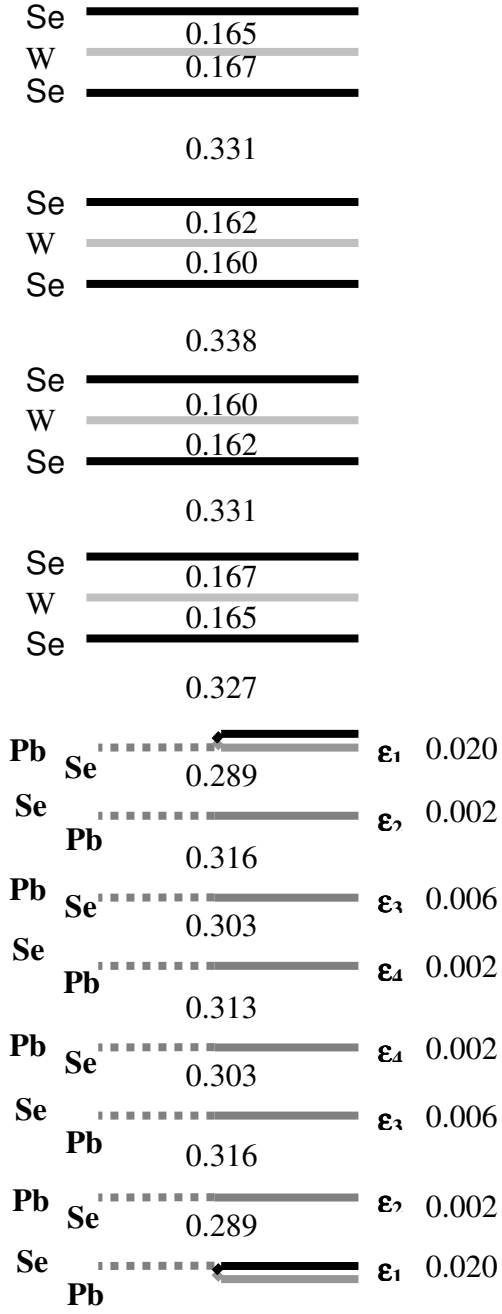

Figure 16: Line diagram of $[(PbSe)_{0.99}]_4[WSe_2]_4$ refinement.

Table 12: Refinement summary for the $[(PbSe)_{0.99}]_4[WSe_2]_4$ sample. There are four contributing models presented. The error values for the overall refinement are located above the table.

		Lebail Fitted w_{rp} = 0.1743	Lebail Fitted rp = 0.1336	Lebail Background w_{rp} = 0.1589	Lebail Background rp = 0.1289	Lebail Dwd = 0.052	Lebail χ^2 = 9.154
c = 50.9219(24)		Fitted wrp = 0.1988	Fitted rp = 0.1510	Background wrp = 0.1806	Background rp = 0.1446	Dwd = 0.043	χ^2 = 11.99
Name	A	B	C	G	Average	layer to layer (nm)	
Se	0.03186(11)	0.03185(11)	0.0333(29)	0.03187(11)	0.03315(10)	0.1688(2)	
W	0.0646(60)	0.06467(60)	0.064701(29)	0.0646(60)	0.0646(5)	0.1602(0)	
Se	0.09857(13)	0.09847(13)	0.0962(29)	0.09859(13)	0.09648(28)	0.1623(6)	
Se	0.16132(15)	0.16143(15)	0.163001(29)	0.16142(15)	0.16149(4)	0.3310(5)	
W	0.19403(60)	0.19408(60)	0.1944(29)	0.19407(60)	0.19427(60)	0.1669(5)	
Se	0.22659(11)	0.22666(12)	0.225801(29)	0.22666(11)	0.22657(5)	0.16449(54)	
Pb	0.28972(90)	0.28869(90)	0.28793(90)	0.28901(90)	0.28884(52)	0.31707(54)	
Se	0.29108(20)	0.29335(21)	0.29414(22)	0.29266(21)	0.29284(12)	0.33747(50)	
Pb	0.34718(90)	0.34824(90)	0.34807(90)	0.34774(90)	0.34781(63)	0.2799(6)	
Se	0.34858(21)	0.34628(21)	0.34775(22)	0.34724(21)	0.34747(15)	0.29855(55)	
Pb	0.41045(80)	0.41023(80)	0.41006(80)	0.41064(80)	0.41034(66)	0.32019(56)	
Se	0.4089(20)	0.40964(20)	0.41089(21)	0.40859(20)	0.40909(83)	0.31208(63)	
Pb	0.46917(80)	0.46902(80)	0.46988(80)	0.46974(80)	0.46945(75)	0.30736(64)	
Se	0.46898(19)	0.4694(20)	0.46785(20)	0.46755(18)	0.46912(95)	0.29929(64)	
Uiso	0.0389(14)	0.0375(15)	0.0714(16)	0.0373(15)	0.0468(1)		

samples in this study; however the variation in the W-Se layer to layer distances is outside the error in this refinement. The effect seems to be stronger at the interface like the effect seen in the $[(PbSe)_{0.99}]_3[WSe_2]_3$ refinement. This suggests one of two things, that there really is an interface effect for odd layered samples or that the Cu refinement has a systematic error that is associated with this type of unequal bonding in a dichalcogenide. Uneven bonding was also observed in $[(Bi_2Te_3)_{1.36}]_m[TiTe_2]_n$ system with Cu refinements,[54] which suggests that if this is an interface effect it likely has nothing to do with charge transfer as there is no known charge transfer between the layers of the $[(Bi_2Te_3)_{1.36}]_m[TiTe_2]_n$ system. It is more likely that this is a systemic error introduced in Cu refinements.

4.10: General Trends

There are some general trends in these refinements as a function of increasing layer thickness. The puckering of the rock salt at the interface does not continue in all of the rock salt layers as shown in Table 14. The puckering disappears in the m = 4 and 5 cases within one layer removed from the interface. Even the m = 2 sample, an outlier in this group of samples, shows decreasing puckering as a function of distance from the interface. The m = 3 sample does not show a similar trend but that may be an effect of the high error of that system obscuring the effect. There does not seem to be a trend in the magnitude of the interfacial rock salt puckering as an effect of the number of layers based on these data.

There is another trend in these data that is based on the unique rock salt layer pairing. Figure 18 shows this trend graphically. The magnitude of the rock salt

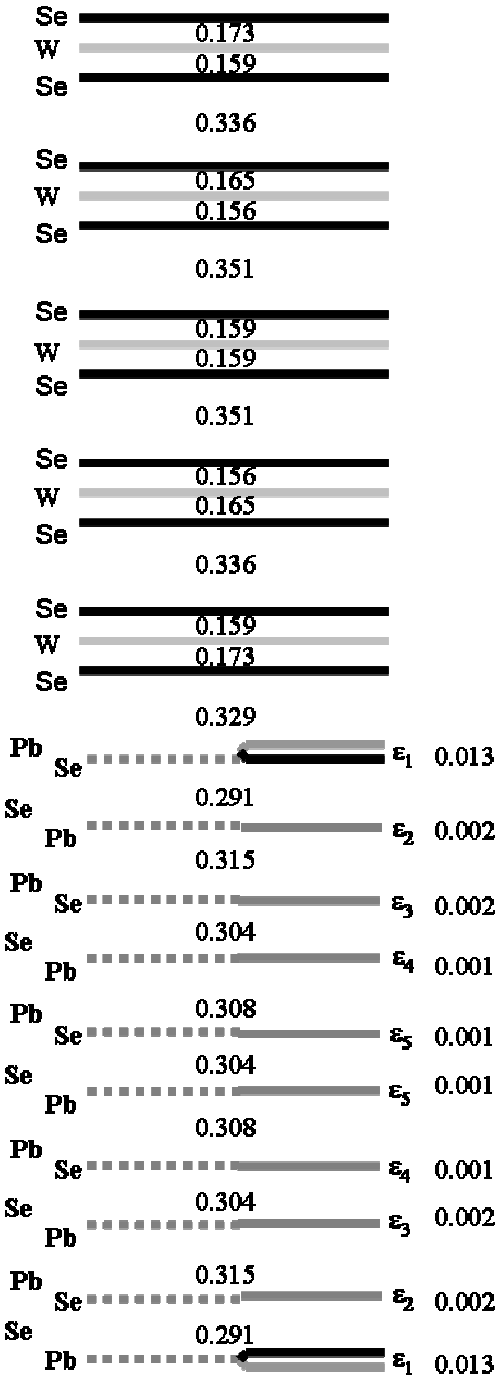

Figure 17: Line diagram of $[(PbSe)_{0.99}]_5[WSe_2]_5$ refinement

Table 13: Refinement summary for the $[(PbSe)_{0.99}]_5[WSe_2]_5$ sample. There are five contributing models presented. The error values for the overall refinement are located above the table.

c = 63.9389(7)		Lebail Fitted w_{rp} = 0.1884 Fitted wrp = 0.2447	Lebail Fitted rp = 0.0721 Fitted rp = 0.1604	Lebail Background w_{rp} = 0.1224 Background wrp = 0.3431	Lebail Background rp = 0.0720 Background rp = 0.1704	Lebail Dwd = 0.312 Dwd = 0.076	Lebail χ^2 = 6.658 χ^2 = 28.44
Name	A	B	C	D	F	Average	Layer to Layer (nm)
W1	0(0)	0(0)	0(0)	0(0)	0(0)	0(0)	0(0)
Se1	0.0244(80)	0.02634(80)	0.02525(90)	0.02621(80)	0.02621(80)	0.02486(20)	0.15896(13)
Se2	0.08047(70)	0.07942(70)	0.08028(70)	0.07951(70)	0.07944(70)	0.07982(12)	0.35143(2)
W2	0.104376(38)	0.104105(38)	0.104556(41)	0.104138(39)	0.10411(39)	0.10416(4)	0.1556(11)
Se3	0.13038(70)	0.12957(70)	0.13042(70)	0.12965(70)	0.12964(70)	0.12993(20)	0.1648(16)
Se4	0.18192(60)	0.18288(70)	0.18204(70)	0.18279(70)	0.18283(70)	0.18251(28)	0.33617(31)
W3	0.207324(33)	0.207421(34)	0.207195(33)	0.207357(34)	0.207431(34)	0.207347(16)	0.15881(28)
Se5	0.2345(70)	0.23403(70)	0.23435(80)	0.23396(80)	0.23402(70)	0.23438(168)	0.17284(1)
Pb1	0.28385(60)	0.28524(50)	0.28519(60)	0.28515(50)	0.28488(60)	0.28484(36)	0.32264(1)
Se6	0.28859(12)	0.28623(11)	0.28545(11)	0.28647(11)	0.28712(11)	0.2868(7)	0.3352(11)
Pb2	0.33291(50)	0.33126(50)	0.33225(50)	0.3308(50)	0.3313(50)	0.3312(24)	0.2838(16)
Se7	0.32903(12)	0.33208(12)	0.33076(12)	0.33327(12)	0.33203(12)	0.33143(9)	0.29793(3)
Pb3	0.38039(12)	0.38044(50)	0.38042(60)	0.3804(50)	0.38053(50)	0.38041(193)	0.31317(13)
Se8	0.38111(13)	0.38088(13)	0.38025(13)	0.38093(13)	0.38071(13)	0.38078(11)	0.31703(2)
Pb4	0.42857(50)	0.42801(50)	0.42827(60)	0.42742(13)	0.42799(50)	0.42817(45)	0.30301(4)
Se9	0.42798(13)	0.42813(13)	0.42851(14)	0.42742(13)	0.42815(13)	0.42805(13)	0.30455(1)
Pb5	0.47589(60)	0.47657(60)	0.47619(70)	0.47544(70)	0.47659(60)	0.47612(68)	0.30736(5)
Se10	0.47613(14)	0.47658(14)	0.47626(15)	0.47627(15)	0.47649(14)	0.47634(15)	0.30804(39)
Uiso	0.0278(70)	0.0305(70)	0.03(1)	0.0307(70)	0.0305(60)	0.0299(4)	

Table 14: Puckering as a function of distance from the interface based on the refinements in this study. The puckering nearly disappears in the m = 4 and 5 samples at just one layer removed from the interface. The m = 3 sample has a high error value that is obscuring this effect.

M	ε_1 (pm)	ε_2 (pm)	ε_3 (pm)	ε_4 (pm)	ε_5 (pm)
1	21(2)				
2	91 (2)	80(2)			
3	9(5)	9(5)	9(5)		
4	20(4)	2(4)	6(4)	2(4)	
5	13(5)	2(5)	2(5)	1(5)	1(5)

distortion is slowly decreasing as a function of the number of layers. This trend and its implications will be discussed further in the next chapter.

4.11: Conclusion

It is possible to refine the positions of the 00*l* planes in isomeric samples using Rietveld refinement. Surprising structural data can be obtained using this technique as evidenced by the discovery of a rock salt distortion in samples with m > 1 and the change in the magnitude of the rock salt puckering as a function of distance from the rock salt/dichalcogenide interface. The fact that the pairwise rock salt distortion was found from a variety of starting models gives weight to the claim that such an unusual feature is real. This discovery will be discussed in detail in Chapter V. The change in the magnitude of the puckering can be interpreted as confirming our initial hypothesis about the energetic cost of puckering in interior layers being quite high.

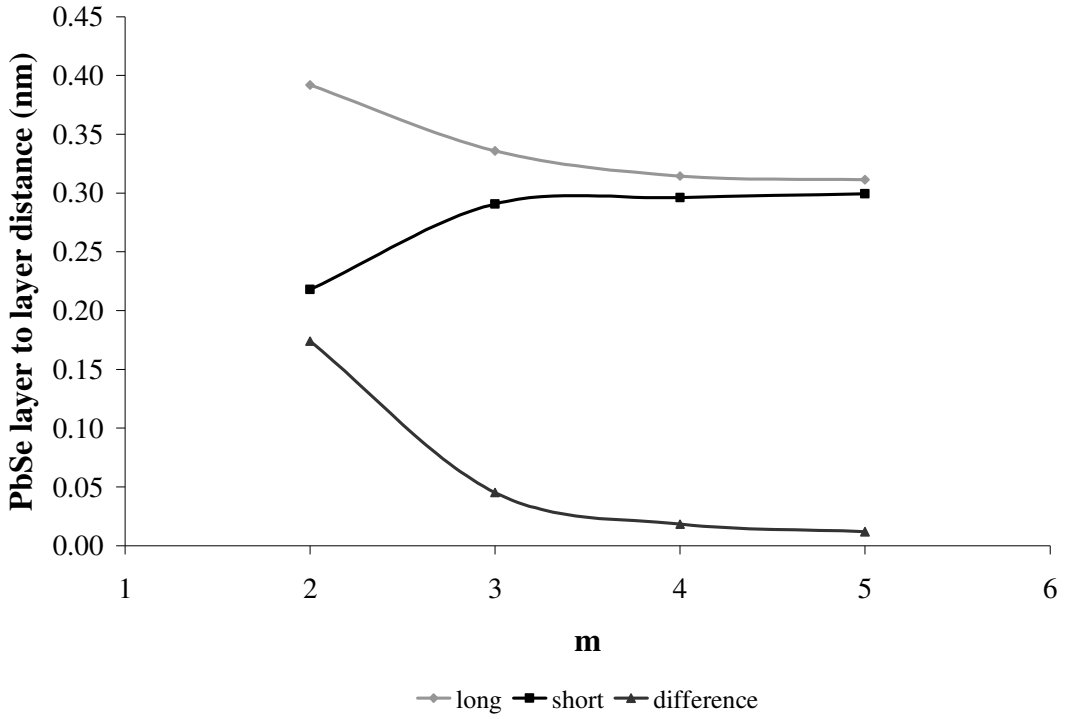

Figure 18: Graph of the trend in the rock salt distortion as a function of the number of rock salt layers. The distortion is decreasing with the increasing number of rock salt layers

CHAPTER V

SIZE-DEPENDENT STRUCTURAL DISTORTIONS IN ONE DIMENTIONAL NANOSTRUCTURES

Samples in this study were made by Dr. Qiyin Lin with the assistance of Benjamin Silver, Logan LaRossa, Paul Hansen, and Johnathan Hanni. X-ray diffraction data taken at the advanced photon source were done in collaboration with Dr. Paul Zschack and Dr. Evguenia Karapetrova who administer beamlines 33 and 34. The samples were run by myself, Dr. Colby Heideman, Dr. Qiyin Lin, Dr. Ngoc Nguyen, Raimar Rostek, and Dr. Clay Mortenson. The space group used for the 00*l* refinements was first used for this purpose by Dr. Arwyn Smalley and Fred Harris for $[(Bi_2Te_3)_{1.36}]_x[TiTe_2]_y$ superlattice samples. Dr. Angus Wilkinson helped them to develop this method of refining 00*l* data. The use of LeBail fits was suggested by Dr. Brian H. Toby. STEM images were taken by Michael D. Anderson in collaboration with Ian M. Anderson at NIST. Robert Kykyneshi performed the molecular dynamical modeling with the assistance of Dr. Douglas Kezsler. I contributed all of the Rietveld refinement data to this chapter. This chapter was written initially by Michael D. Anderson but edited by myself, David C. Johnson, Ian Anderson, Qiyin Lin, and Robert Kykyneshi for details concerning our individual contributions. It is as yet unpublished but will be submitted to *Science*.

5.1: Introduction

Nanoscale materials have been intensely studied since the discovery that the optical properties of semiconductor nanoparticles are size dependent because the spatial

extent of the localized wave functions of the electron-hole exciton pair is confined by the size of the nanoparticle.[1-3] This and subsequent research has demonstrated that the physical properties of particles become a function of size when the size becomes comparable to a characteristic length scale of an underlying physical property. Examples of relevant length scales include the de Broglie wavelength and the mean free path of electrons, phonons, and elementary excitations, which typically range from one to a few hundred nanometers. The ability to tune a wide variety of properties with size has spurred the development of a number of different chemistries that enable the preparation of nanostuctured elements and compounds with control of size, shape and ligand shell.[4-8]

5.2: Results

As the size of nanocrystals decrease, the number of atoms in the interior relative to the number of atoms at the surface decreases. This increases the importance of surface free energy relative to the free energy of the bulk structure and distortions from bulk structures might be expected as nanoparticle size decreases. Unfortunately, while researchers have demonstrated the ability to prepare ordered lattices of nanoparticles,[9-14] isolating crystals with long range atomic periodicity is rare,[11,13,15] in part because common synthetic approaches produce a distribution of nanoparticle sizes. Thus, detailed atomic structures and size-structure-property relationships of most nanoparticle systems have not been determined.[15-17]

We recently reported the preparation of families of new compounds with the general formula $[(MSe)_{1+y}]_m(TSe_2)_n$, where M=Pb, Bi and Ce; T=W, Nb, and Ta.[18-19] The values of *m* and *n*, respectively, represent the number of MX and TX_2 structural units of the unit cell of the superstructure. The misfit parameter, *y*, describes the difference

between the densities of metal cations in the two structural units. Each TSe_2 structural unit consists of a hexagonal layer of metal cations T sandwiched between hexagonal close-packed planes of selenium anions, with the cations located in either the octahedral (stacking sequence ACB) or trigonal prismatic (ABA) interstices of the anion sublattice. Each MSe structural unit contains two distorted *00l* planes of the rock salt structure. The rock salt structured layers are incommensurate with the close-packed selenium planes of the TSe_2 structural unit. As reported herein, the long range structural order along the modulation direction permits us to determine the atomic structure of these precisely defined one-dimensional (1D) nanostructures as a function of layer thickness using both scanning transmission electron microscopy (STEM) high-angle annular dark field (HAADF) imaging and x-ray diffraction.

The STEM-HAADF images of the first five $[(PbSe)_{1.00}]_m(MoSe_2)_m$ compounds are shown in Figure 19. All have a regular periodic structure along the modulated axis with well-defined layers of PbSe and $MoSe_2$. Compositional profiles acquired by STEM x-ray energy- dispersive spectroscopy (XEDS) are consistent with the nominal PbSe and $MoSe_2$ stoichiometries. The STEM images show ordered domains of PbSe with characteristic dimensions of a single structural unit along the layering direction and tens of nanometers perpendicular to the layering direction, with random in-plane rotational variants both within a layer and between layers. The orientations of the $MoSe_2$ domains are more difficult to discern from the STEM images, but rotational variants have been observed between individual $MoSe_2$ structural units. Close examination of the STEM-HAADF images reveals a distortion of the PbSe layers, with the atomic planes grouped into pairs rather than being evenly spaced as expected for an undistorted rock salt

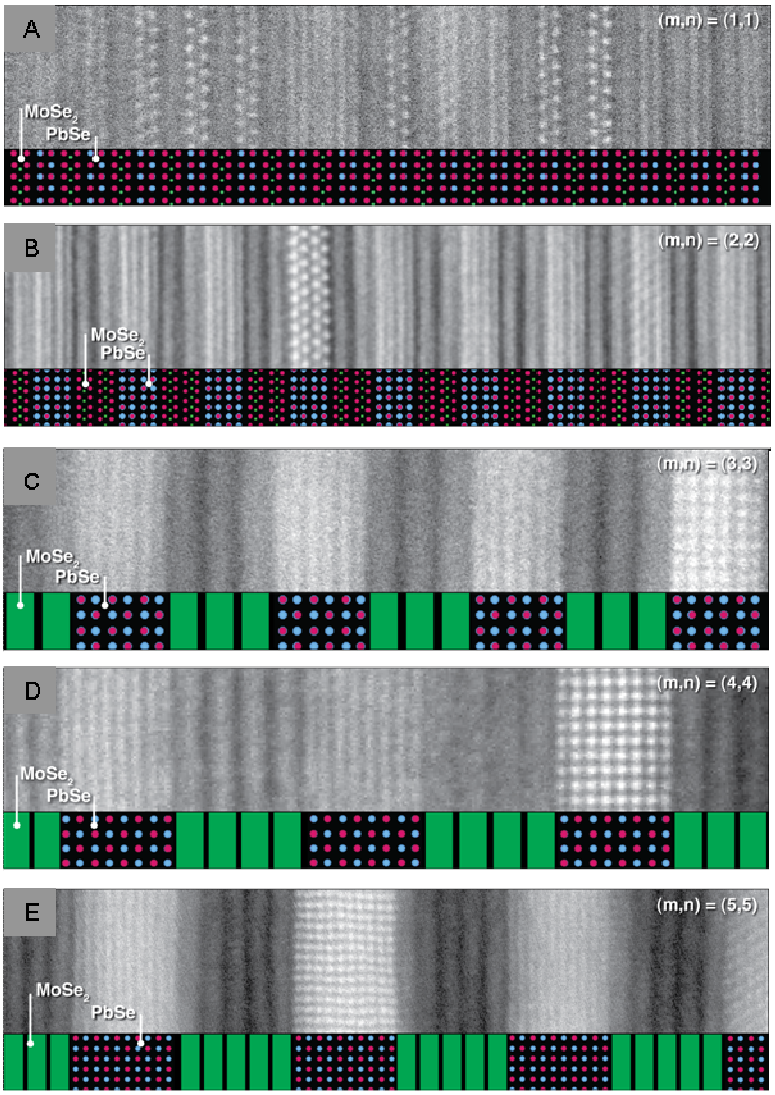

Figure 19: High resolution STEM-HAADF images of $[(PbSe)_{1.00}]_m[MoSe_2]_m$ compounds showing the change in the pairing distortion in the PbSe layers as a function of the number of *00l* PbSe planes. The rock-salt-structured domains exhibit numerous rotational variants within the (001)-oriented growth plane, with selected grains aligned along the <100>- and <110>-type zone axes.

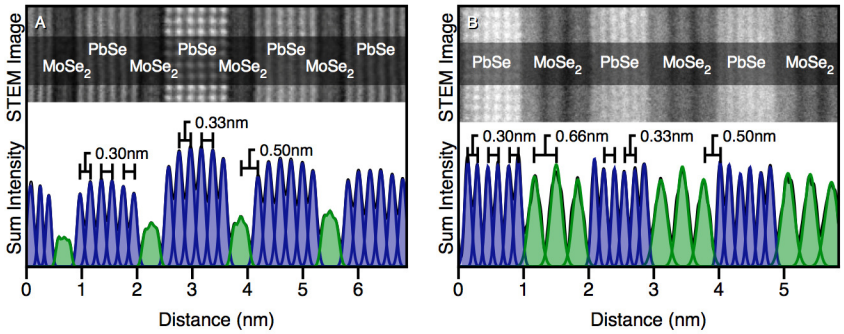

Figure 20: High resolution STEM-HAADF images of $[(PbSe)_{0.99}]_3[MoSe_2]_1$ and $[(PbSe)_{0.99}]_3[MoSe_2]_3$ with aggregate intensity plots. The distances noted are for the PbSe intra- and inter-pair distance as well as the distances between the last PbSe layer and the central maxima of the $MoSe_2$ region and the distance between consecutive $MoSe_2$ regions.

structure. The distortion is largest in $[(PbSe)_{1.00}]_2(MoSe_2)_2$ and decreases until it can not be observed for *n* greater than 5, suggesting that this is the transition to a bulk structure.

The extended registry of atomic planes along the modulation axis results in X-ray diffraction patterns (Figure 21A) containing many *00l* diffraction maxima, which can be used to determine the position of atomic planes along the c axis and the magnitude of the structural distortions observed in the STEM-HAADF data. The lattice parameters of the superstructure in the c-axis direction exhibit discrete changes of $\Delta c_m = 0.607 \pm 0.007$ nm and $\Delta c_n = 0.657 \pm 0.005$ nm as the number *m* or *n* of the PbSe or $MoSe_2$ structural units, respectively, is incremented. In-plane x-ray diffraction scans (Figure 21A) contain Bragg diffraction maxima that can all be indexed based on independent crystal structures for the PbSe ($a = b = 0.618 \pm 0.001$ nm) and $MoSe_2$ ($a = 0.331 \pm 0.001$ nm) layers. The line widths of the reflections *hk0* of the PbSe and $MoSe_2$ structural units differ, reflecting different in-plane domain sizes of 9 ± 1 nm for PbSe and 4 ± 1 nm for $MoSe_2$. There is no trend in the lattice parameters or in-plane domain sizes as *n* and *m* increase and the films also remain flat when removed from the sample substrate, suggesting that there is little strain between the layers despite the lattice mismatch between the layers. The random rotational variants observed in the PbSe between layers precludes the observation of coherent diffraction between layers along mixed index *hkl* ($h,k \neq 0$; $l \neq 0$) directions. As shown Figure 21C however, weak subsidiary maxima are observed along mixed index reflections of the PbSe constituent. These maxima result from the finite size of the crystallites in these directions, as can be observed by the identical patterns observed for both $(PbSe)_3(MoSe_2)_1$ and $(PbSe)_3(MoSe_2)_3$. The diffraction data in Figure 21 strongly suggest that the lattices of PbSe and $MoSe_2$ are not constrained by epitaxy at the

interfaces, that the rock salt structured layers are crystallographically decoupled from one another, and that the layer thickness of one component does not affect the structure of the other. Rietveld refinements of the 00l diffraction pattern of a $[(PbSe)_{0.99}]_1(WSe_2)_1$ compound are consistent with that previously reported for similar m=1, n=1 compounds.[20] The refinements reveal that Pb and Se planes in the distorted rock salt structured layer are separated by 22 pm, with the Pb containing layers within the rock salt structural unit displaced closer to the selenium of the dichalcogenide. This interfacial distortion or layer puckering is within the range (2 pm to 80 pm) previously reported.[20]

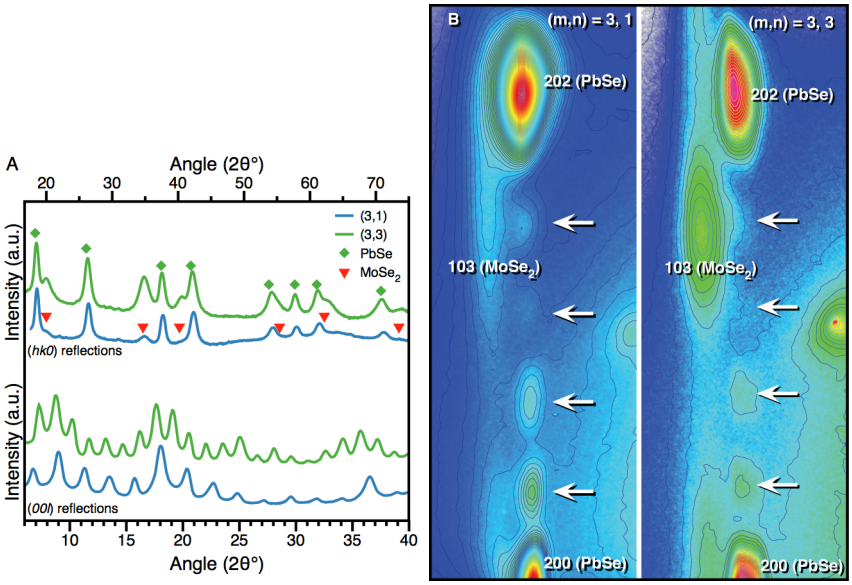

Figure 21: X-ray diffraction patterns acquired from $[(PbSe)_{0.99}]_3[MoSe_2]_1$ and $[(PbSe)_{0.99}]_3[MoSe_2]_3$. A. Bragg-Brentano patterns acquired using Cu Kα radiation (λ = 154 pm) with the bottom patterns collected perpendicular to the films and the top two patterns collected in the plane of the films. B. Two-dimensional in-plane patterns acquired using synchrotron radiation (λ = 92.53 pm). All peaks can be indexed based on independent crystal structures for PbSe and $MoSe_2$. The four weak reflections corresponding to non-integer indices along 20l of PbSe, indicated with arrows, are discussed in the text.

Refinements of the first five $[(PbSe)_{0.99}]_m(WSe_2)_m$ compounds all reveal puckering of the surface Pb-Se layer that decreases moving into the interior Pb-Se planes. The refinements also reveal that the PbSe planes are paired, as observed in STEM-

HAARD data, and the average difference between the intra pair and inter pair distances decreases as the number of PbSe planes increases.

To model the observed distortions, density functional theory (DFT) simulations were performed for isolated sheets of rock salt PbSe with layer thickness along the c axis ranging from 1 to 5 unit cells. Idealized PbSe structures of thickness $m \times c$ (m = 1 to 5; c = 0.306 nm) were allowed to relax to minimum-energy configurations. In the case of a single unit cell (m = 1), a strong reduction to c = 0.283 nm is observed, while the a-lattice parameter remains unchanged. The experimentally observed pairing distortion for $m > 1$ is also observed; as m increases, the average c parameter approaches the bulk value. In the case of n = 5, the bulk PbSe structure is largely restored with only small distortions in the terminal units. These results provide additional evidence that the distortions are size

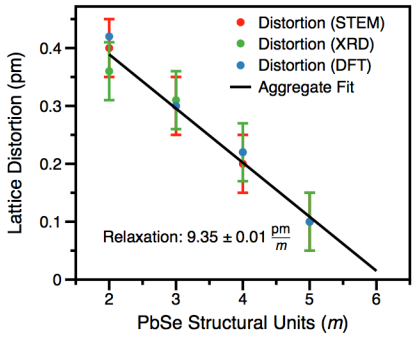

Figure 22: The difference between the long and short PbSe interplane distance distortion as a function of increasing then number of PbSe structural units.

dependent and decoupled from the dichalcogenide layers. Only a slight puckering (≈ 6 pm for $n < 5$; ≈ 3 pm for n = 5) is observed for the surfaces of the relaxed PbSe layers, which is significantly smaller than the experimentally observed value of 22 pm. The puckering, however, increases to 15 pm in the presence of the dichalcogenide layer in a model $(PbSe)_1(WSe_2)_1$ structure, likely resulting from Pb completing its coordination

through bonding with the Se of WSe_2 and charge transfer from the WSe_2 to PbSe structural units.

Figure 22 contains a graph of the magnitude of the pairing distortion as a function of the number of PbSe structural units calculated from the DFT simulations, determined from the STEM images, and obtained from the refinement of the x-ray diffraction data. The magnitude of the distortion decreases in a linear fashion as the number of planes of PbSe is increased. Conceptually the distortion of the rock salt structure can be broken into two distinct contributions: a surface distortion of the outer plane to optimize the interaction between the PbSe and $MoSe_2$ regions; and a volume distortion of the structure to minimize the total energy. The systematic structural distortions observed in PbSe as the number of planes is decreased has significant implications, perhaps explaining the synthetic difficulties in isolating very small cluster sizes of extended structures. The observed structural distortions also suggest a possible root cause for the size dependency of physical properties, and that discontinuities in physical properties with size should be expected for nanostructures as a consequence of structural distortions.

5.3: Bridge

This chapter has detailed the trends observed in the structure of the m = 1 to 5 isomer series. Three techniques were used to explain the structural trends observed in order to confirm the unusual results. In order to get further insight into these materials a set of non-isomer samples was inspected. The samples used are chosen to look at the effects of varying m and n as much as possible.

CHAPTER VI

$[(PbSe)_{0.99})]_m[WSe_2]_n$; m = 1 OR 2, n = 1 OR 2 REFINEMENTS

The samples in this chapter were synthesized and annealed by Dr. Qiyin Lin. X-ray diffraction data taken at the advanced photon source were done in collaboration with Dr. Paul Zschack and Dr. Evguenia Karapetrova who administer beamlines 33 and 34. The samples were run by myself, Dr. Colby Heideman, Dr. Qiyin Lin, Dr. Ngoc Nguyen, and Dr. Clay Mortenson. The space group used for the 00*l* refinements was first used for this purpose by Dr. Arwyn Smalley and Fred Harris for $[(Bi_2Te_3)_{1.36}]_x[TiTe_2]_y$ superlattice samples. Dr. Angus Wilkinson helped them to develop this method of refining 00*l* data. The use of LeBail fits was suggested by Dr. Brian H. Toby. I completed all of the Rietveld refinements found in this chapter as well as the subsequent data analysis. I am primary author of this chapter and eventually it will be published as a paper but has not been touched by any other than David Johnson as yet.

6.1: Introduction

Misfit layered compounds have primarily been studied in their m = n = 1 form, structurally, electronically, and magnetically.[1, 2] There are three theories on why MLCs are stable despite it being the combination of two very different compounds; charge transfer occurring from the rock salt to the dichalcogenide layer,[3-9] cationic coupling based on the oxidation states of the materials,[10] or covalent bonding at the interface.[11, 12] Various experiments have shown that charge transfer is occurring based on XPS and Raman measurements[3-5, 13, 14] however, there are also contradictory reports that claim the opposite.[11, 15] The cationic coupling argument was based on EPMA measurements

combined with valence bonding calculations. As for covalent bonding, the first reference is an XPS study which posited covalent bonding instead of charge transfer as an explanation for their data and the second is based on valence bonding calculations for incommensurate layered structures (the crystal group to which MLCs apply).

A study of samples with a large change in the ratio of rock salt to dichalcogenide layers could elucidate which mechanism is the most likely. In the scenario that there is charge transfer from the rock salt to the dichalcogenide there would be a large difference in the amount of puckering in the rock salt at the interface as well as a probable change in the structure of the dichalcogenide layer. In the case of covalent bonding the magnitude of the puckering should not alter and there should be no change to the dichalcogenide layer. The cationic coupling theory applied here would predict a change in the magnitude of the puckering and the structure of the dichalcogenide. This study will use the structure of $[(PbSe)_{0.99}]_m[WSe_2]_n$ where m and n = 1 or 2 in all combinations.

6.2: Experimental

All samples in this study were prepared using a custom high vacuum deposition chamber (~10^{-7} Torr) which is described elsewhere.[16] Lead and tungsten were deposited using electron beam guns and Se was deposited with a Knudsen evaporation cell. Precursors were prepared by sequentially depositing each element to prepare a repeating unit with a composition profile similar to the desired final product and then this sequence of elemental layers was repeated to obtain the desired total thickness of the film. The relative thickness of the pair of elements to form each binary constituent was calibrated to obtain the composition that corresponds to the stoichiometry of the desired constituent. The thickness of each elemental pair was adjusted to yield layers with the number of

atoms required to form a discrete crystalline PbSe bilayer or a WSe_2 trilayer respectively. The deposition produces a mostly amorphous precursor, which is then gently annealed to form the desired product. This process is described in detail elsewhere.[17] Samples were annealed at 400°C in a nitrogen atmosphere for an hour.

X-ray diffraction patterns of $[(PbSe)_{0.99}]_1[WSe_2]_1$, $[(PbSe)_{0.99}]_1[WSe_2]_2$, $[(PbSe)_{0.99}]_2[WSe_2]_1$, and $[(PbSe)_{0.99}]_2[WSe_2]_2$ were measured in the high resolution 33ID beam line at the Advanced Photon Source (APS) at Argonne National Laboratory (ANL). Due to the strong texturing of these systems, only *00l* peaks are present in Bragg-Brentano scans (cross-plane) and only *hk0* peaks are present in grazing incidence 2-theta scans (in-plane). Anomalous scattering experiments measured the cross plane scattering of each sample in the Bragg-Brentano optical geometry. The anomalous scans of $[(PbSe)_{0.99}]_1[WSe_2]_1$ and $[(PbSe)_{0.99}]_2[WSe_2]_2$ were done above and below the Pb L_3 absorption line with wavelengths of 95.78 pm and 94.29 pm. Points were taken every 0.005˚ with a count time of 1 second from 12˚ to 50˚ (2θ). The anomalous scattering scans of $[(PbSe)_{0.99}]_1[WSe_2]_2$ were taken at 98.99 pm, below the Se K_β absorption line, and 93.08 pm, above the Pb L_3 absorption line. For the 98.99pm scan points were taken every 0.05˚ with a count time of 1 second from 4˚ to 24˚ (2θ). The 93.08 pm scan was taken from 4˚ to 26˚ (2θ) with a step size of 0.02˚ and a count time of 1 second. The scans of $[(PbSe)_{0.99}]_2[WSe_2]_1$ were taken at 93.79 and 93.09 pm both above the Pb L_3 absorption line.

Rietveld refinement was completed using the General Structural Analysis System (GSAS)[18] with EXPGUI.[19] The 00*l* scans contain Kiessig fringes, interference patterns between the front and back of the sample, which overlap the Bragg reflections out to as

high as 30˚ 2θ in some samples. GSAS does not include algorithms to model this phenomenon. LeBail fits were performed on each scan and used as a starting point for the model refinement in order to help reduce the error due to correlation caused by overlapping peaks and to refine profile parameters, background, unit cell size and zero offset corrections. The LeBail fit represents the best possible refinement for a given set of experimental data and was compared to each Rietveld model refinement in order to judge the quality of the fit which, because of the presence of Kiessig fringes has abnormally high error values. The anomalous diffraction data collected along the c-axis was used to refine the z coordinates of the atomic planes using all energies simultaneously. Initial models that extended beyond the known range of distortions in misfit-layered compounds were used to explore parameter space to try to make sure the refinement did not converge to local minima.

6.3: Results

The $[(PbSe)_{0.99}]_1[WSe_2]_1$ refinement has already been discussed in chapter III and in chapter IV, however to be clear in this section the data will be reiterated here. Figure 23 is the Rietveld refinement result for the system. The refinement summary is in Table 15. The final result is the combination of six separate refinements. The error reported in the summary table is the estimated standard deviation of the values as calculated by the refinement program, the e.s.d. on the average has been propagated from the component refinements. The actual deviation of this system is believed to be 2 pm. The wrp and rp values are higher than they would be otherwise for this fit because there is Kiessig fringing in this scan going to ~30˚ 2θ.

Notably this refinement has similar attributes to similar structures found in the literature. The dichalcogenide layer to layer distance is greater than the binary value from literature, which is seen in several other MLC systems. The magnitude of the puckering of the rock salt at the interface is well within the range of values in the literature. Finally the size of the sub-units and the full MLC unit follow the same trends seen in other m = n = 1 compounds.

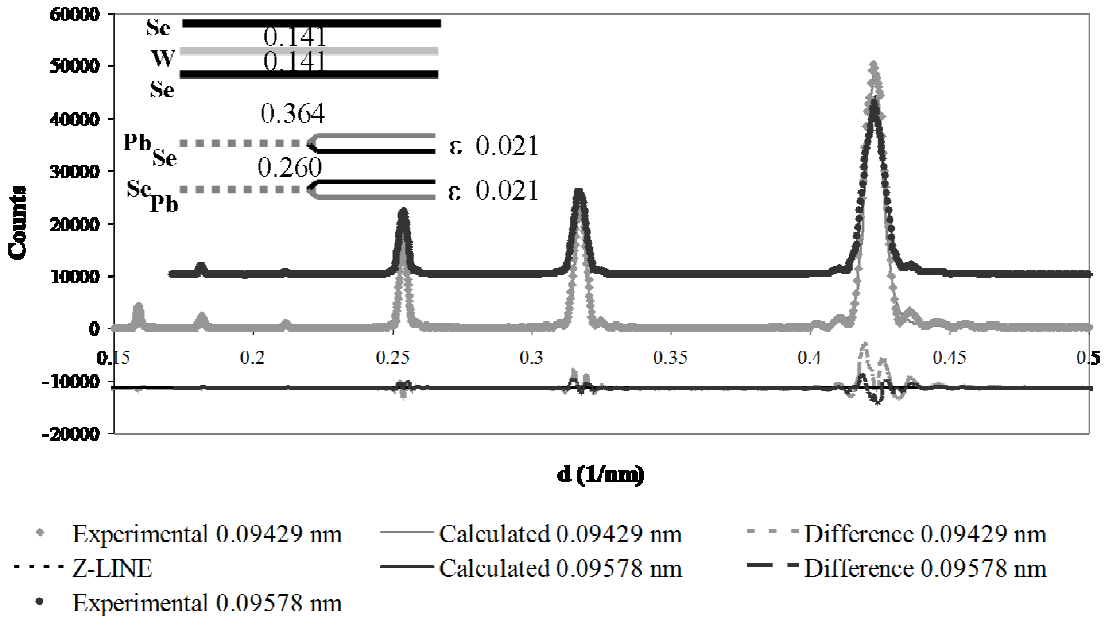

Figure 23: Rietveld refinement of $[(PbSe)_{0.99}]_1[WSe_2]_1$ above and below the Pb L_3 absorption line.

The $[(PbSe)_{0.99}]_1[WSe_2]_2$ refinement is summarized in Table 16. The final result is the combination of six separate refinements. Figure 23 Rietveld refinement result for the system. The estimated error actual deviation of this system is believed to be 2 pm. The sample is not nearly as smooth as the $[(PbSe)_{0.99}]_1[WSe_2]_1$ sample, so Kiessig fringing only continues to ~20˚ 2θ.

Notably this refinement has similar attributes to similar structures found in the literature. The dichalcogenide layer to layer distance is greater than the binary value

Table 15: Rietveld refinement summary of $[(PbSe)_{0.99}]_1[WSe_2]_1$.

		Lebail Fitted w_{rp} = 0.1801	Lebail Fitted rp = 0.1187	Lebail Background w_{rp} = 0.1599	Lebail Background rp = 0.1098	Lebail Dwd = 0.084	Lebail χ^2 = 34.88	
	c = 12.6968(3)	Fitted w_{rp} = 0.1799	Fitted rp = 0.1187	Background w_{rp} = 0.1600	Background rp = 0.1084	Dwd = 0.084	χ^2 = 34.82	
Atom	A	B	C	D	E	F	Average	Layer to Layer (nm)
W1	0(0)	0(0)	0(0)	0(0)	0(0)	0(0)	0(0)	0(0)
Se1	0.11097(16)	0.11097(16)	0.11097(16)	0.11097(16)	0.11097(16)	0.11097(16)	0.11097(4)	0.14089(3)
Pb1	0.3892(40)	0.3892(40)	0.3892(40)	0.3892(40)	0.3892(40)	0.3892(40)	0.3892(27)	0.3533(3)
Se2	0.4057(14)	0.40571(14)	0.4057(14)	0.40572(14)	0.4057(14)	0.4057(14)	0.4057(8)	0.3742(1)
Uiso	0.0788(11)	0.0788(11)	0.0788(11)	0.07967(110)	0.0788(11)	0.0788(11)	0.0789(2)	

Table 16: Rietveld refinement summary of $[(PbSe)_{0.99}]_1[WSe_2]_2$.

	Lebail Fitted w_{rp} = 0.1167	Lebail Fitted rp = 0.0808	Lebail Background w_{rp} = 0.1025	Lebail Background rp = 0.0735	Lebail Dwd = 0.237	Lebail χ^2 = 12.66	
c = 19.1758(5)	Fitted w_{rp} = 0.1426	Fitted rp = 0.1092	Background w_{rp} = 0.1328	Background rp = 0.1050	Dwd = 0.161	χ2 = 19.00	
Name	A	B	C	D	E	Average	Layer to layer
SE1	0.09353(24)	0.09354(24)	0.09353(24)	0.09353(24)	0.09355(24)	0.0935(1)	1.7936(5)
W1	0.17519(10)	0.17519(10)	0.17505(10)	0.17519(10)	0.17517(10)	0.1752(0)	1.5651(5)
SE2	0.26449(18)	0.26449(18)	0.26395(18)	0.26449(18)	0.2644(180)	0.2644(0)	1.7110(6)
PB1	0.41826(14)	0.41806(14)	0.41554(14)	0.4183(14)	0.4171(1)	0.4180(1)	2.9455(6)
SE3	0.41892(31)	0.41944(31)	0.42626(34)	0.4189(31)	0.4219(3)	0.4197(1)	2.9789(7)
Uiso	0.0582(15)	0.0582(15)	0.0595(15)	0.0582(15)	0.0584(15)	0.059(0)	

from literature, which is seen in several other MLC systems. The magnitude of the puckering of the rock salt at the interface is well within the range of values in the literature. Finally the size of the sub-units and the full MLC unit follow the same trends seen in other m =1, n = 2 compounds[20-23] and is similar to incommensurate refinement done on one of the systems.[24]

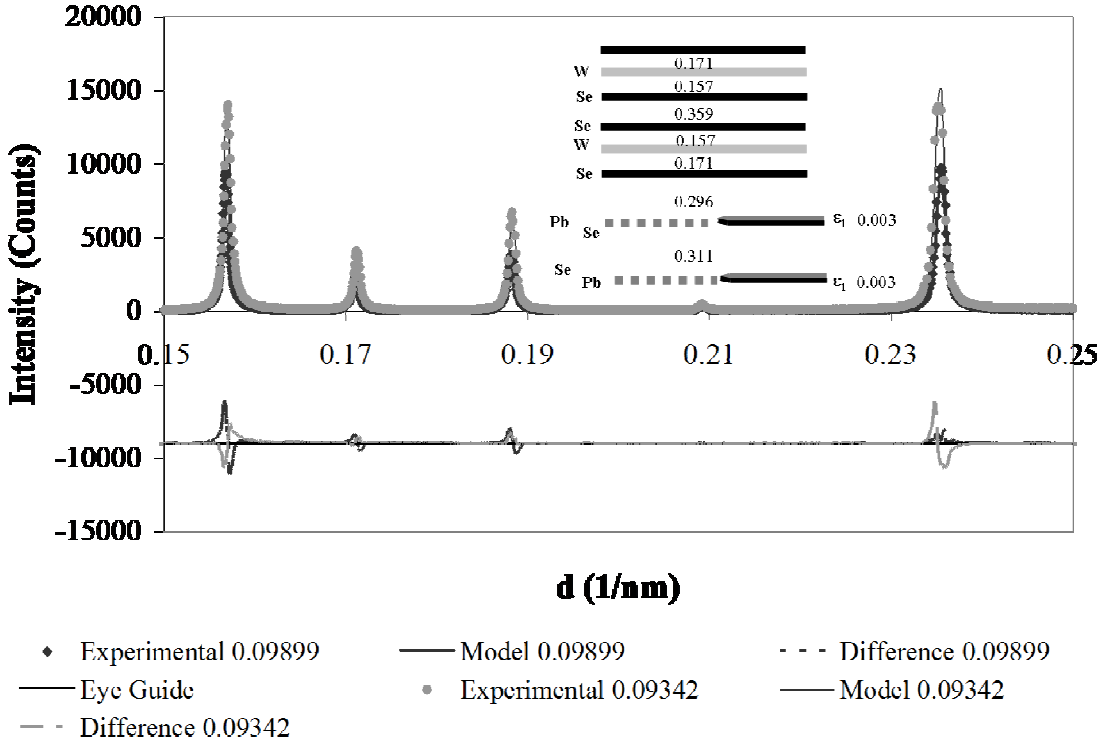

Figure 24: Rietveld refinement of $[(PbSe)_{0.99}]_1[WSe_2]_2$ with line diagram illustrating refinement results.

The $[(PbSe)_{0.99}]_2[WSe_2]_2$ refinement has also been discussed in chapter III and in chapter IV, but will be reiterated here. Figure 25 is the Rietveld refinement result for the system and the refinement summary is in Table 17. The reported refinement is the combination of five refinements. The actual deviation of this system is believed to be 2 pm. There is Kiessig fringing in this scan going to ~20˚ 2θ.

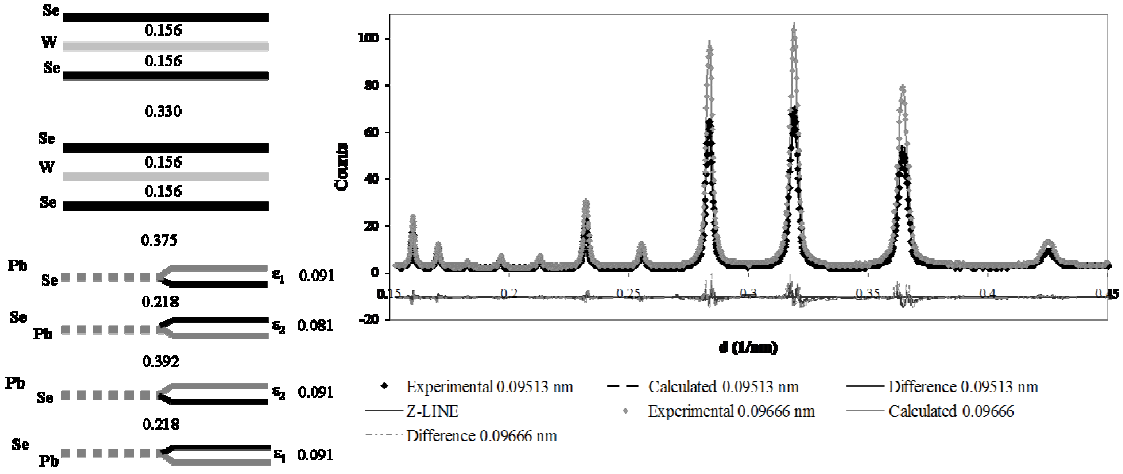

Figure 25: Rietveld refinement of $[(PbSe)_{0.99}]_2[WSe_2]_2$ above and below the Pb L_3 line with line diagram illustrating refinement results.

The m = n = 2 sample type had not been studied before in the literature so there is no precedent for how the bonding should look. The distortion of the rock salt layers has been discussed in chapter V and is believed to be real. The puckering at the interface and in the interior rock salt layers is quite large, outside the normal range and could be a real effect or this refinement could be the result of a very strong local minima.

The $[(PbSe)_{0.99}]_2[WSe_2]_1$ refinement is summarized in Table 18. The final result is the combination of six separate refinements. Figure 26 is the Rietveld refinement result for the system. The estimated error actual deviation of this system is believed to be ~4 pm, because the scans were done on the same side of the Se K_β line and there is not as much contrast in the scattering factor as in the other samples in this study. The sample is not nearly as smooth as the $[(PbSe)_{0.99}]_1[WSe_2]_1$ sample, so Kiessig fringing only continues to ~15˚ 2θ.

Notably this refinement has similar attributes to the other m = 1, n=1 sample found in the literature.[25] The average dichalcogenide layer to layer distance is greater

Table 17: Rietveld refinement summary of $[(PbSe)_{0.99}]_2[WSe_2]_2$.

Refinement	c = 25.52856(4)	Lebail Fitted w_{rp} = 0.1384 Fitted w_{rp} = 0.1051	Lebail Fitted rp = 0.0808 Fitted rp = 0.1000	Lebail Background w_{rp} = 0.1118 Backround w_{rp} = 0.1181	Lebail Background rp = 0.0918 Backround rp = 0.0901	Lebail Dwd = 0.328 Dwd = 0.141	Lebail χ^2 = 3.726 $\chi 2$ = 7.212
Atom	A	C	D	E	F	Average	Layer to layer
SE1	0.06716(10)	0.06717(10)	0.06971(60)	0.06717(10)	0.06774(90)	0.06886(4)	1.758(0)
W2	0.12971(40)	0.12971(40)	0.129165(28)	0.12971(40)	0.12971(40)	0.12970(9)	1.5530(5)
SE3	0.1913(80)	0.1913(80)	0.1888(50)	0.1913(80)	0.19807(8)	0.19087(3)	1.561(3)
PB4	0.31993(70)	0.31993(70)	0.32248(14)	0.31993(70)	0.32059(70)	0.3201(4)	3.299(4)
SE5	0.35236(21)	0.35237(21)	0.35875(70)	0.35238(21)	0.35443(20)	0.3557(3)	4.209(3)
PB6	0.44026(70)	0.44026(70)	0.43534(70)	0.44026(70)	0.4398(700)	0.4390(1)	2.126(0)
SE7	0.41139(20)	0.41138(20)	0.39287(16)	0.41137(20)	0.40928(19)	0.4075(2)	2.231(1)
Uiso	0.0946(60)	0.1370(9)	0.1654(13)	0.1008(11)	0.1008(11)	0.122(1)	

Table 18: Rietveld refinement summary of $[(PbSe)_{0.99}]_2[WSe_2]_1$.

c = 18.8369(4)	Lebail Fitted w_{rp} = 0.2115 Fitted w_{rp} = 0.2096	Lebail Fitted rp = 0.1542 Fitted rp = 0.1614	Lebail Background w_{rp} = 0.2086 Background w_{rp} = 0.2036	Lebail Background rp = 0.1524 Background rp = 0.1590	Lebail Dwd = 0.063 Dwd = 0.063	Lebail χ^2 = 22.49 χ^2 = 22.12	
Name	A	B	C	D	E	Average	layer to layer
W1	0(0)	0(0)	0(0)	0(0)	0(0)	0(0)	0(0)
SE1	0.08199(13)	0.08565(13)	0.085(16)	0.085(16)	0.085(0)	0.0850(2)	1.600(6)
PB1	0.25592(10)	0.26095(26)	0.25949(19)	0.25949(19)	0.25949(19)	0.2595(1)	3.287(10)
SE2	0.2791(1)	0.26698(64)	0.27135(47)	0.27135(47)	0.27135(47)	0.2704(3)	3.493(10)
PB2	0.40584(80)	0.41334(80)	0.41628(14)	0.41628(14)	0.41628(14)	0.4110(5)	2.647(2)
SE3	0.42994(25)	0.40936(19)	0.40176(39)	0.40176(39)	0.40176(39)	0.4070(3)	2.778(1)
Uiso	0.0786(90)	0.0787(90)	0.0749(90)	0.0749(90)	0.0749(90)	0.0764(2)	

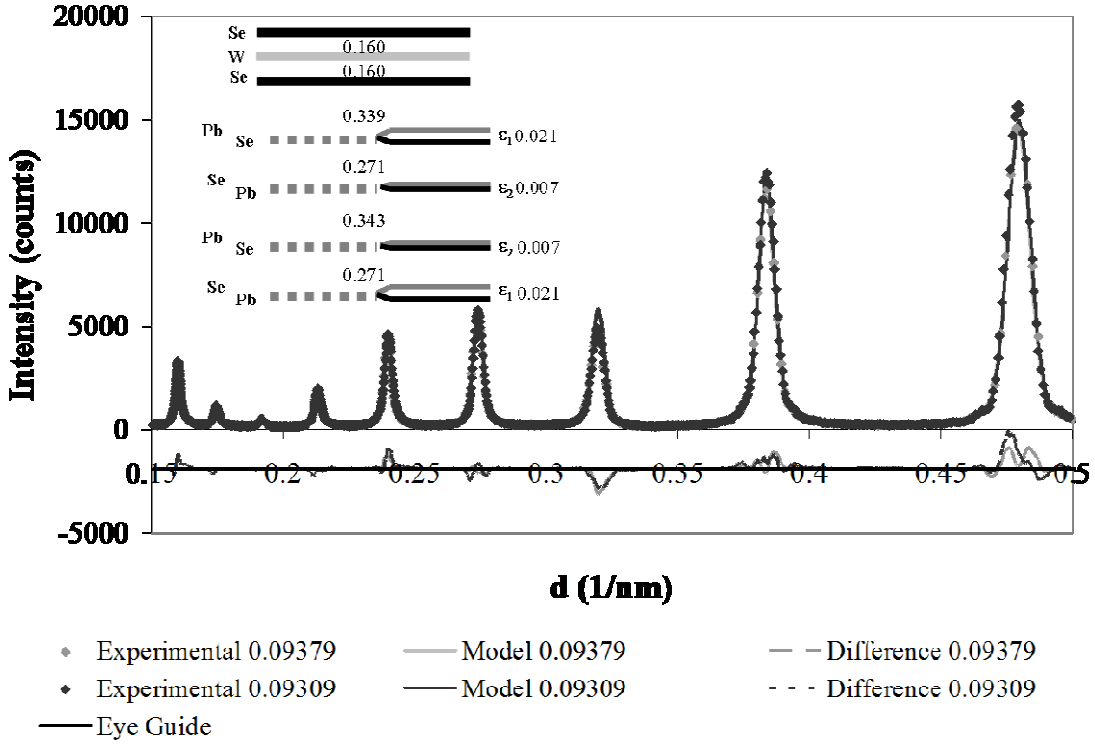

Figure 26: Rietveld refinement of $[(PbSe)_{0.99}]_2[WSe_2]_1$ with line diagram illustrating refinement results.

than the binary value from literature, which is seen in several the literature system. The strange thing about the value is that it is not the same on either side of the W-Se bond. This is not observed in other systems but combined with the small magnitude of the puckering of the rock salt at the interface it is believed that this may be indicative of cations in the van der Waal gap of the WSe_2. Cations in this location would increase the size of the van der Waal gap, cause the W-Se bonds to be unequal and would push the W insensitive to the refinement of the occupancy parameter, however, so this hypothesis cannot be confirmed. Finally the size of the sub-units and the full MLC unit follow the same trends seen in other m =2, n = 1 compound.

6.4: Discussion

The plane to plane distances for all of these refinements have been summarized in Table 19. There are several notable points in these values. First, the puckering of the $[(PbSe)_{0.99}]_1[WSe_2]_2$ and $[(PbSe)_{0.99}]_2[WSe_2]_1$ samples is drastically different, 3 and 21 pm respectively. This large difference would be expected in the case of charge transfer between the rock salt and dichalcogenide layers in the system. There is no great difference between the average W-Se plane to plane distance in these samples, however, which one might expect to be altered if charge transfer were present but might be untouched if there is covalent bonding in the system. These results are counter indicators and do not elucidate the stabilization mechanism of the system.

The unequal plane to plane distances of the $[(PbSe)_{0.99}]_1[WSe_2]_2$ sample add a second implication that charge transfer is not the primary stabilization method in these samples because a sample with more dichalcogenide layers would not be expected to have asymmetry in a charge transfer scenario, however if the hypothesis that there is cation in the interface is accurate this may not indicate anything other than an excess of material in the sample.

Table 19: Summary of important plane to plane distances for samples in the study.

m/n	Interface (nm)	van der Waal gap (nm)	PbSe interface pucker (nm)	PbSe interior pucker (nm)	PbSe long (nm)	PbSe short (nm)	W-Se average (nm)
1/1	0.364	-	0.021	-	-	0.260	0.140
1/2	0.296	0.359	0.003	-	-	0.296	0.164
2/1	0.339	-	0.021	0.007	0.343	0.271	0.160
2/2	0.387	0.357	0.093	0.089		0.215	0.151

The magnitude of the puckering in the m = n =1 and m = n = 2 samples is quite different though the samples have the same rock salt to dichalcogenide ratio. This result

does not make sense at all but if the m = n = 2 refinement is in a strong local equilibrium the refinement could potentially be very similar to the other samples.

6.5: Conclusion

The refinements presented here do not help elucidate the method of stabilization of MLCs. There are contradictory structural indicators in this regards. Further study using either Raman or XPS is needed to map the bands of these samples in order to determine what is really causing these samples to be kinetically stable.

CHAPTER VII

CONCLUSION

Samples of highly oriented thin film misfit layered compounds were structurally characterized using Rietveld refinement of x-ray diffraction of both the cross-plane and one case the in-plane direction, STEM-HAADF, and area detector scans. Because of the strong preferred orientation, the refinements were completed in a multi-step process. First LeBail fits were done to find the ideal possible fit for each sample. A series of starting models were developed for each sample based on the expected layering sequence, literature precedent where available, and some hypotheses concerning the stabilization mechanism of the structure when no available. The LeBail fit refined parameters were used for all of those refinements. The final values for each refinement were reported as a weighted average of the contributing refinements.

The results for the $[(MSe)_{1+\delta}]_1$ $[TSe_2]_1$ refinements were consistent with literature precedent for MLC samples. This was true both for the 00*l* and the *hk*0 refinements. The error of the refined parameters is higher than the propagated error based on the estimated standard deviation values produced by the refinement program. This is because differing values can be obtained by using a different LeBail fit, this variability is reflected in the values reported in the line diagrams of these materials.

Refinements of the isomeric series $[(PbSe)_{0.99}]_m$ $[WSe_2]_m$, m = 1 to 5 reveal a distortion in the rock salt portion of the MLC when it is composed of more than one rock salt bi-layer. The layers maintain volume but distort in pairs where on bi-layer plane of atoms is closer to itself than the next bi-layer of atoms. This distortion is reduced as

more rock salt layers are added. These results were reinforced using STEM pictures and a total energy simulation.

Samples with a large range of rock salt to dichalcogenide layer ratio were refined. There is a wide variability in layer to layer thicknesses in the samples. There do not seem to be any indicators of the stabilization mechanism in MLCs based on these structures in this study.

APPENDIX A

AVERAGE MODELS FROM REFINEMENTS IN CHAPTER III

A1: $[(PbSe)_{0.99}]_1[WSe_2]_1$ Refinement

APS anomalous		Pb edge	c = 12.697(3)Å
Atom	Z	Site Occupancy	Filling Fraction
W	0	1	0.993(6)
Se	0.1102(4)	2	1.000(6)
Pb	0.3884(5)	2	0.480(3)
Se	0.4084(2)	2	0.487(3)
Uiso	0.0785(4)		
Fitted		Background	
wrp	0.1801	wrp	0.1599
rp	0.1187	rp	0.1098
Dwd	0.084		
χ^2	34.88		

Lebail

Fitted		Background	
wrp	0.1776	wrp	0.156
rp	0.1151	rp	0.1058
Dwd	0.089		
χ^2	33.91		

A.2: $[(PbSe)_{1.00}]_1[MoSe_2]_1$ Refinement

APS anomalous		Pb edge	c = 12.658(2)Å
Atom	z	Site Occupancy	Filling Fraction
W/Pb	0	1	0.85(5)/0.17(5)
Se	0.1195(2)	2	1
Pb	0.3813(4)	2	0.49(5)
Se	0.4011(6)	2	0.49(5)
Uiso	0.125(2)		
Fitted		Background	
Wrp	0.1795	wrp	0.1556
Rp	0.1166	rp	0.1093
Dwd	0.059		
χ^2	7.435		

Lebail

Fitted		Background	
Wrp	0.1474	wrp	0.1226
Rp	0.0836	rp	0.0752
Dwd	0.078		
χ^2	7.141		

A.3: $[(SnSe)_{1.03}]_1[WSe_2]_1$ Refinement

APS anomalous		Pb edge	c = 12.425(6)Å
Atom	z	Site Occupancy	Filling Fraction
W	0	1	1.0(4)
Se	0.128(15)	2	1
Pb	0.379(28)	2	0.48(2)
Se	0.408(53)	2	0.49(2)
Uiso	0.14(2)		
Fitted		Background	
wrp	0.2633	wrp	0.2780
rp	0.1761	rp	0.1631
Dwd	0.084		
χ^2	34.88		

Lebail

Fitted		Background	
wrp	0.2367	wrp	0.2460
rp	0.1473	rp	0.1331
Dwd	0.220		
X	11.15		

APPENDIX B

STARTING MODELS

All of the tables in this appendix are organized as follows. First, the outcome of the starting model's refinements are presented, labeled using increasing letters (A, B, C, etc). If additional refinements were deemed necessary, they are then presented using increasing numbers (1, 2, 3, etc), after a brief explanation of their significance.

Each refinement is presented with the following columns:

spacing (Å)
cumm- Cummulative (Å)
frac – Fractional Coordinate
occ- Fractional Occupancy

B.1: $[(PbSe)_{1.00}]_1[MoSe_2]_1$ Refinement

A				
Name	**spacing**	**cumm**	**frac**	**occ**
Mo	0	0	0	1.0
Se	1.6	1.6	0.128789	1.0
Pb	3.2	4.8	0.386368	0.5
Se	3.4	5	0.402466	0.5

B				
Name	**spacing**	**cumm**	**frac**	**occ**
Mo	0	0	0	1.0
Se	1.6	1.6	0.128789	1.0
Pb	3.3	4.9	0.394417	0.5
Se	3.3	4.9	0.394417	0.5

C				
Name	**spacing**	**cumm**	**frac**	**occ**
Mo	0	0	0	1.0
Se	1.6	1.6	0.128789	1.0
Pb	3	4.6	0.370269	0.5
Se	3.6	5.2	0.418565	0.5

D				
Name	**spacing**	**cumm**	**frac**	**occ**
Mo	0	0	0	1.0
Se	1.5	1.5	0.12074	1.0
Pb	3.2	4.7	0.378318	0.5
Se	3.4	4.9	0.394417	0.5

E				
Name	**spacing**	**cumm**	**frac**	**occ**
Mo	0	0	0	1.0
Se	1.4	1.4	0.112691	1.0
Pb	3.2	4.6	0.370269	0.5
Se	3.4	4.8	0.386368	0.5

F				
Name	**spacing**	**cumm**	**frac**	**Occ**
Mo	0	0	0	1.0
Se	1.7	1.7	0.136839	1.0
Pb	3.2	4.9	0.394417	0.5
Se	3.4	5.1	0.410516	0.5

The following tables include the addition of occupancy parameter variations and of cation mixing to the $[(PbSe)_{1.00}]_1[MoSe_2]_1$ refinement

1				
Name	**spacing**	**cumm**	**frac**	**Occ**
Pb	0	0	0	0.05
Mo	0	0	0	0.95
Se	1.6	1.6	0.111188	1
Pb	3.2	4.8	0.37726	0.5
Se	3.4	5	0.391356	0.5

2				
Name	**spacing**	**cumm**	**frac**	**Occ**
Pb	0	0	0	0.1
Mo	0	0	0	0.9
Se	1.6	1.6	0.111188	1
Pb	3.3	4.9	0.37726	0.5
Se	3.3	4.9	0.391356	0.5

3				
Name	**spacing**	**cumm**	**frac**	**Occ**
Pb	0	0	0	0.15
Mo	0	0	0	0.85
Se	1.6	1.6	0.111188	1
Pb	3	4.6	0.37726	0.5
Se	3.6	5.2	0.391356	0.5

4				
Name	**spacing**	**cumm**	**frac**	**Occ**
Pb	0	0	0	0.2
Mo	0	0	0	0.8
Se	1.5	1.5	0.111188	1
Pb	3.2	4.7	0.37726	0.5
Se	3.4	4.9	0.391356	0.5

5				
Name	**spacing**	**cumm**	**frac**	**occ**
Pb	0	0	0	0.25
Mo	0	0	0	0.75
Se	1.5	1.5	0.111188	1
Pb	3.2	4.7	0.37726	0.5
Se	3.4	4.9	0.391356	0.5

6				
Name	**spacing**	**cumm**	**frac**	**occ**
Pb	0	0	0	0.15
Mo	0	0	0	0.85
Se	1.6	1.6	0.128789	1
Pb	3.2	4.8	0.386368	0.5
Se	3.4	5	0.402466	0.5

7				
Name	**spacing**	**cumm**	**frac**	**occ**
Pb	0	0	0	0.15
Mo	0	0	0	0.85
Se	1.6	1.6	0.128789	1
Pb	3.3	4.9	0.394417	0.5
Se	3.3	4.9	0.394417	0.5

8				
Name	**spacing**	**cumm**	**frac**	**occ**
Pb	0	0	0	0.15
Mo	0	0	0	0.85
Se	1.6	1.6	0.128789	1
Pb	3	4.6	0.370269	0.5
Se	3.6	5.2	0.418565	0.5

9				
Name	**spacing**	**cumm**	**frac**	**occ**
Pb	0	0	0	0.15
Mo	0	0	0	0.85
Se	1.5	1.5	0.12074	1
Pb	3.2	4.7	0.378318	0.5
Se	3.4	4.9	0.394417	0.5

10				
Name	**spacing**	**cumm**	**frac**	**occ**
Pb	0	0	0	0.15
Mo	0	0	0	0.85
Se	1.4	1.4	0.112691	1
Pb	3.2	4.6	0.370269	0.5
Se	3.4	4.8	0.386368	0.5

11				
Name	**spacing**	**cumm**	**frac**	**occ**
Pb	0	0	0	0.15
Mo	0	0	0	0.85
Se	1.7	1.7	0.136839	1
Pb	3.2	4.9	0.394417	0.5
Se	3.4	5.1	0.410516	0.5

12				
Name	**spacing**	**cumm**	**frac**	**occ**
Pb	0	0	0	0.15
Mo	0	0	0	0.85
Se	1.6	1.6	0.128789	1
Pb	3.2	4.8	0.386368	0.5
Se	3.4	5	0.402466	0.5

13				
Name	**spacing**	**cumm**	**frac**	**occ**
Pb	0	0	0	0.15
Mo	0	0	0	0.85
Se	1.6	1.6	0.128789	1
Pb	3.3	4.9	0.394417	0.5
Se	3.3	4.9	0.394417	0.5

14				
Name	**spacing**	**cumm**	**frac**	**occ**
Pb	0	0	0	0.15
Mo	0	0	0	0.85
Se	1.6	1.6	0.128789	1
Pb	3	4.6	0.370269	0.5
Se	3.6	5.2	0.418565	0.5

15				
Name	**spacing**	**cumm**	**frac**	**occ**
Pb	0	0	0	0.15
Mo	0	0	0	0.85
Se	1.5	1.5	0.12074	1
Pb	3.2	4.7	0.378318	0.5
Se	3.4	4.9	0.394417	0.5

16				
Name	**spacing**	**cumm**	**frac**	**occ**
Pb	0	0	0	0.15
Mo	0	0	0	0.85
Se	1.4	1.4	0.112691	1
Pb	3.2	4.6	0.370269	0.5
Se	3.4	4.8	0.386368	0.5

17				
Name	**spacing**	**cumm**	**frac**	**occ**
Pb	0	0	0	0.15
Mo	0	0	0	0.85
Se	1.7	1.7	0.136839	1
Pb	3.2	4.9	0.394417	0.5
Se	3.4	5.1	0.410516	0.5

B2: $[(SnSe)_{1.03}]_1[MoSe_2]_1$ Refinement

A				
Name	**spacing**	**cumm**	**frac**	**Occ**
Mo	0	0	0	1.0
Se	1.6	1.6	0.128789	1.0
Sn	3.2	4.8	0.386368	0.51
Se	3.4	5	0.402466	0.51

B				
Name	**spacing**	**cumm**	**frac**	**Occ**
Mo	0	0	0	1.0
Se	1.6	1.6	0.128789	1.0
Sn	3.3	4.9	0.394417	0.51
Se	3.3	4.9	0.394417	0.51

C				
Name	**spacing**	**cumm**	**frac**	**Occ**
Mo	0	0	0	1.0
Se	1.6	1.6	0.128789	1.0
Sn	3	4.6	0.370269	0.51
Se	3.6	5.2	0.418565	0.51

D				
Name	**spacing**	**cumm**	**frac**	**Occ**
Mo	0	0	0	1.0
Se	1.5	1.5	0.12074	1.0
Sn	3.2	4.7	0.378318	0.51
Se	3.4	4.9	0.394417	0.51

E				
Name	**spacing**	**cumm**	**frac**	**Occ**
Mo	0	0	0	1.0
Se	1.4	1.4	0.112691	1.0
Sn	3.2	4.6	0.370269	0.51
Se	3.4	4.8	0.386368	0.51

F				
Name	**spacing**	**cumm**	**frac**	**Occ**
Mo	0	0	0	1.0
Se	1.7	1.7	0.136839	1.0
Sn	3.2	4.9	0.394417	0.51
Se	3.4	5.1	0.410516	0.51

B.3: $[(PbSe)_{0.99}]_1[WSe_2]_1$ Refinement

A				
Name	**spacing**	**cumm**	**frac**	**occ**
W	0	0	0	1.0
Se	1.6	1.6	0.128789	1.0
Pb	3.2	4.8	0.386368	0.5
Se	3.4	5	0.402466	0.5

B				
Name	**spacing**	**cumm**	**frac**	**Occ**
W	0	0	0	1.0
Se	1.6	1.6	0.128789	1.0
Pb	3.3	4.9	0.394417	0.5
Se	3.3	4.9	0.394417	0.5

C				
Name	**spacing**	**cumm**	**frac**	**Occ**
W	0	0	0	1.0
Se	1.6	1.6	0.128789	1.0
Pb	3	4.6	0.370269	0.5
Se	3.6	5.2	0.418565	0.5

D				
Name	**spacing**	**cumm**	**frac**	**Occ**
W	0	0	0	1.0
Se	1.5	1.5	0.12074	1.0
Pb	3.2	4.7	0.378318	0.5
Se	3.4	4.9	0.394417	0.5

E				
Name	**spacing**	**cumm**	**frac**	**Occ**
W	0	0	0	1.0
Se	1.4	1.4	0.112691	1.0
Pb	3.2	4.6	0.370269	0.5
Se	3.4	4.8	0.386368	0.5

F				
Name	**spacing**	**cumm**	**frac**	**Occ**
W	0	0	0	1.0
Se	1.7	1.7	0.136839	1.0
Pb	3.2	4.9	0.394417	0.5
Se	3.4	5.1	0.410516	0.5

B.4: $[(PbSe)_{0.99}]_2[WSe_2]_2$ Refinement

A				
Name	**spacing**	**cumm**	**frac**	**occ**
Se	1.7	1.7	0.067589	1.0
W	1.6	3.3	0.131202	1.0
Se	1.6	4.9	0.194816	1.0
Pb	3.2	8.1	0.322042	0.5
Se	3.4	8.3	0.329994	0.5
Pb	3.3	11.6	0.461196	0.5
Se	3.3	11.4	0.453244	0.5

B				
Name	**spacing**	**cumm**	**frac**	**occ**
Se	1.7	1.7	0.067589	1.0
W	1.6	3.3	0.131202	1.0
Se	1.6	4.9	0.194816	1.0
P	3.3	8.2	0.326018	0.5
Se	3.3	8.2	0.326018	0.5
Pb	3.3	11.5	0.45722	0.5
Se	3.3	11.5	0.45722	0.5

C				
Name	**spacing**	**cumm**	**frac**	**occ**
Se	1.7	1.7	0.067589	1.0
W	1.6	3.3	0.131202	1.0
Se	1.6	4.9	0.194816	1.0
Pb	3.1	8	0.318066	0.5
Se	3.5	8.4	0.333969	0.5
Pb	3.3	11.7	0.465172	0.5
Se	3.6	11.6	0.461196	0.5

D				
Name	**spacing**	**cumm**	**frac**	**occ**
Se	1.7	1.7	0.067589	1.0
W	1.5	3.2	0.127226	1.0
Se	1.5	4.7	0.186864	1.0
Pb	3.2	7.9	0.31409	0.5
Se	3.4	8.1	0.322042	0.5
Pb	3.3	11.4	0.453244	0.5
Se	3.3	11.2	0.445293	0.5

E				
Name	**spacing**	**cumm**	**frac**	**occ**
Se	1.7	1.7	0.067589	1.0
W	1.5	3.2	0.127226	1.0
Se	1.4	4.6	0.182888	1.0
Pb	3.3	7.9	0.31409	0.5
Se	3.3	7.9	0.31409	0.5
Pb	3.3	11.2	0.445293	0.5
Se	3.3	11.2	0.445293	0.5

F				
Name	**spacing**	**cumm**	**frac**	**occ**
Se	1.7	1.7	0.067589	1.0
W	1.5	3.2	0.127226	1.0
Se	1.7	4.9	0.194816	1.0
P	3.1	8	0.318066	0.5
Se	3.5	8.4	0.333969	0.5
Pb	3	11.4	0.453244	0.5
Se	3.6	11.6	0.461196	0.5

The next table is the average with fade for the $[(PbSe)_{0.99}]_2[WSe_2]_2$ refinement

G				
Name	**spacing**	**cumm**	**frac**	**occ**
Se	1.7	1.7	0.067589	1.0
W	1.5	3.2	0.127226	1.0
Se	1.7	4.9	0.194816	1.0
p	3.2	8.1	0.322042	0.5
Se	3.5	8.4	0.333969	0.5
Pb	3.2	11.6	0.461196	0.5
Se	3.5	11.6	0.461196	0.5

B.5: $[(PbSe)_{0.99}]_3[WSe_2]_3$ Refinement

A				
Name	**spacing**	**cumm**	**Frac**	**Occ**
W	0	0	0	1.0
Se	1.6	1.6	0.041908	1.0
Se	3.4	5	0.130962	1.0
W	1.6	6.6	0.17287	1.0
Se	1.6	8.2	0.214778	1.0
Pb	3.2	11.4	0.298593	0.5
Se	3.4	11.6	0.303832	0.5
Pb	3.3	14.9	0.390267	0.5
Se	3.3	14.7	0.385028	0.5
Pb	3.3	18	0.471463	0.5
Se	3.3	18.2	0.476702	0.5

B				
Name	**spacing**	**cumm**	**Frac**	**Occ**
W	0	0	0	1.0
Se	1.6	1.6	0.041908	1.0
Se	3.4	5	0.130962	1.0
W	1.6	6.6	0.17287	1.0
Se	1.6	8.2	0.214778	1.0
Pb	3.3	11.5	0.301213	0.5
Se	3.3	11.5	0.301213	0.5
Pb	3.3	14.8	0.387648	0.5
Se	3.3	14.8	0.387648	0.5
Pb	3.3	18.1	0.474083	0.5
Se	3.3	18.1	0.474083	0.5

C				
Name	**spacing**	**cumm**	**frac**	**Occ**
W	0	0	0	1.0
Se	1.6	1.6	0.041908	1.0
Se	3.4	5	0.130962	1.0
W	1.6	6.6	0.17287	1.0
Se	1.6	8.2	0.214778	1.0
Pb	3.1	11.3	0.295974	0.5
Se	3.5	11.7	0.306451	0.5
Pb	3.1	14.8	0.387648	0.5
Se	3.4	14.7	0.385028	0.5
Pb	3.3	18	0.471463	0.5
Se	3.2	18	0.471463	0.5

D				
Name	**spacing**	**cumm**	**frac**	**Occ**
W	1.5	1.5	0.039289	1.0
Se	1.5	3	0.078577	1.0
Se	3.4	6.4	0.167631	1.0
W	1.5	7.9	0.20692	1.0
Se	1.5	9.4	0.246209	1.0
Pb	3.2	12.6	0.330024	0.5
Se	3.4	12.8	0.335263	0.5
Pb	3.3	16.1	0.421698	0.5
Se	3.3	15.9	0.416459	0.5
Pb	3.3	19.2	0.502894	0.5
Se	3.3	19.4	0.508133	0.5

E				
Name	**spacing**	**cumm**	**frac**	**Occ**
W	1.5	1.5	0.039289	1.0
Se	1.5	3	0.078577	1.0
Se	3.4	6.4	0.167631	1.0
W	1.5	7.9	0.20692	1.0
Se	1.5	9.4	0.246209	1.0
Pb	3.3	12.7	0.332644	0.5
Se	3.3	12.7	0.332644	0.5
Pb	3.3	16	0.419079	0.5
Se	3.3	16	0.419079	0.5
Pb	3.3	19.3	0.505514	0.5
Se	3.3	19.3	0.505514	0.5

F				
Name	**spacing**	**cumm**	**frac**	**Occ**
W	1.5	1.5	0.039289	1.0
Se	1.5	3	0.078577	1.0
Se	3.4	6.4	0.167631	1.0
W	1.5	7.9	0.20692	1.0
Se	1.5	9.4	0.246209	1.0
Pb	3.1	12.5	0.327405	0.5
Se	3.5	12.9	0.337882	0.5
Pb	3.1	16	0.419079	0.5
Se	3.4	15.9	0.416459	0.5
Pb	3.3	19.2	0.502894	0.5
Se	3.2	19.2	0.502894	0.5

G				
Name	**spacing**	**cumm**	**frac**	**occ.**
W	1.6	1.6	0.04191	1.0
Se	1.6	3.2	0.08382	1.0
Se	3.4	6.6	0.17287	1.0
W	1.6	8.2	0.21478	1.0
Se	1.6	9.8	0.25669	1.0
Pb	3.3	13.1	0.34312	0.5
Se	3.4	13.2	0.34574	0.5
Pb	2.9	16.1	0.42170	0.5
Se	2.9	16	0.41908	0.5
Pb	3.2	19.2	0.50289	0.5
Se	3.2	19.3	0.50551	0.5

The next table is the average for the $[(PbSe)_{0.99}]_3[WSe_2]_3$ refinement

H				
Name	**spacing**	**cumm**	**frac**	**occ.**
W	1.6	1.6	0.04191	1.0
Se	1.6	3.2	0.08382	1.0
Se	3.4	6.6	0.17287	1.0
W	1.6	8.2	0.21478	1.0
Se	1.5	9.7	0.25407	1.0
Pb	3.1	12.8	0.33526	0.5
Se	3.5	13.2	0.34574	0.5
Pb	3.1	16.3	0.42694	0.5
Se	3.4	16.2	0.42432	0.5
Pb	3.3	19.5	0.51075	0.5
Se	3.2	19.5	0.51075	0.5

B.6: $[(PbSe)_{0.99}]_4[WSe_2]_4$ Refinement

		A		
Name	**spacing**	**cumm**	**Frac**	**Occ**
Se	1.7	1.7	0.033203	1.0
W	1.6	3.3	0.064453	1.0
Se	1.6	4.9	0.095703	1.0
Se	3.4	8.3	0.162109	1.0
W	1.6	9.9	0.193359	1.0
Se	1.6	11.5	0.224609	1.0
Pb	3.2	14.7	0.287109	0.5
Se	3.4	14.9	0.291016	0.5
Pb	3.3	18.2	0.355469	0.5
Se	3.3	18	0.351563	0.5
Pb	3.3	21.3	0.416016	0.5
Se	3.3	21.5	0.419922	0.5
Pb	3.3	24.8	0.484375	0.5
Se	3.3	24.6	0.480469	0.5

		B		
Name	**spacing**	**cumm**	**frac**	**Occ**
Se	1.7	1.7	0.033203	1.0
W	1.6	3.3	0.064453	1.0
Se	1.6	4.9	0.095703	1.0
Se	3.4	8.3	0.162109	1.0
W	1.6	9.9	0.193359	1.0
Se	1.6	11.5	0.224609	1.0
Pb	3.3	14.8	0.289063	0.5
Se	3.3	14.8	0.289063	0.5
Pb	3.3	18.1	0.353516	0.5
Se	3.3	18.1	0.353516	0.5
Pb	3.3	21.4	0.417969	0.5
Se	3.3	21.4	0.417969	0.5
Pb	3.3	24.7	0.482422	0.5
Se	3.3	24.7	0.482422	0.5

Name	spacing	C cumm	frac	Occ
Se	1.7	1.7	0.033203	1.0
W	1.6	3.3	0.064453	1.0
Se	1.6	4.9	0.095703	1.0
Se	3.4	8.3	0.162109	1.0
W	1.6	9.9	0.193359	1.0
Se	1.6	11.5	0.224609	1.0
Pb	3.1	14.6	0.285156	0.5
Se	3.4	14.9	0.291016	0.5
Pb	3.2	18.1	0.353516	0.5
Se	3.4	18	0.351563	0.5
Pb	3.3	21.3	0.416016	0.5
Se	3.2	21.3	0.416016	0.5
Pb	3.3	24.6	0.480469	0.5
Se	3.3	24.6	0.480469	0.5

Name	spacing	D cumm	frac	Occ
Se	1.7	1.7	0.033203	1.0
W	1.5	3.2	0.0625	1.0
Se	1.5	4.7	0.091797	1.0
Se	3.4	8.1	0.158203	1.0
W	1.5	9.6	0.1875	1.0
Se	1.5	11.1	0.216797	1.0
Pb	3.2	14.3	0.279297	0.5
Se	3.4	14.5	0.283203	0.5
Pb	3.3	17.8	0.347656	0.5
Se	3.3	17.6	0.34375	0.5
Pb	3.3	20.9	0.408203	0.5
Se	3.3	21.1	0.412109	0.5
Pb	3.3	24.4	0.476563	0.5
Se	3.3	24.2	0.472656	0.5

E

Name	spacing	cumm	frac	Occ
Se	1.7	1.7	0.033203	1.0
W	1.5	3.2	0.0625	1.0
Se	1.5	4.7	0.091797	1.0
Se	3.4	8.1	0.158203	1.0
W	1.5	9.6	0.1875	1.0
Se	1.5	11.1	0.216797	1.0
Pb	3.3	14.4	0.28125	0.5
Se	3.3	14.4	0.28125	0.5
Pb	3.3	17.7	0.345703	0.5
Se	3.3	17.7	0.345703	0.5
Pb	3.3	21	0.410156	0.5
Se	3.3	21	0.410156	0.5
Pb	3.3	24.3	0.474609	0.5
Se	3.3	24.3	0.474609	0.5

F

Name	spacing	cumm	frac	Occ
Se	1.7	1.7	0.033203	1.0
W	1.5	3.2	0.0625	1.0
Se	1.5	4.7	0.091797	1.0
Se	3.4	8.1	0.158203	1.0
W	1.5	9.6	0.1875	1.0
Se	1.5	11.1	0.216797	1.0
Pb	3.1	14.2	0.277344	0.5
Se	3.4	14.5	0.283203	0.5
Pb	3.2	17.7	0.345703	0.5
Se	3.4	17.6	0.34375	0.5
Pb	3.3	20.9	0.408203	0.5
Se	3.2	20.9	0.408203	0.5
Pb	3.3	24.2	0.472656	0.5
Se	3.3	24.2	0.472656	0.5

B.7: $[(PbSe)_{0.99}]_5[WSe_2]_5$ Refinement

		A		
Name	**Spacing**	**cumm**	**frac**	**Occ**
W	0	0	0	1.0
Se	1.6	1.6	0.025024	1.0
Se	3.4	5	0.0782	1.0
W	1.6	6.6	0.103223	1.0
Se	1.6	8.2	0.128247	1.0
Se	3.4	11.6	0.181423	1.0
W	1.6	13.2	0.206447	1.0
Se	1.6	14.8	0.231471	1.0
Pb	3.2	18	0.281518	0.5
Se	3.4	18.2	0.284646	0.5
Pb	3.3	21.5	0.336258	0.5
Se	3.3	21.3	0.33313	0.5
Pb	3.3	24.6	0.384742	0.5
Se	3.3	24.8	0.38787	0.5
Pb	3.3	28.1	0.439481	0.5
Se	3.3	27.9	0.436353	0.5
Pb	3.3	31.2	0.487965	0.5
Se	3.3	31.4	0.491093	0.5

		B		
Name	**spacing**	**cumm**	**frac**	**Occ**
W	0	0	0	1.0
Se	1.6	1.6	0.025024	1.0
Se	3.4	5	0.0782	1.0
W	1.6	6.6	0.103223	1.0
Se	1.6	8.2	0.128247	1.0
Se	3.4	11.6	0.181423	1.0
W	1.6	13.2	0.206447	1.0
Se	1.6	14.8	0.231471	1.0
Pb	3.3	18.1	0.283082	0.5
Se	3.3	18.1	0.283082	0.5
Pb	3.3	21.4	0.334694	0.5
Se	3.3	21.4	0.334694	0.5
Pb	3.3	24.7	0.386306	0.5
Se	3.3	24.7	0.386306	0.5
Pb	3.3	28	0.437917	0.5
Se	3.3	28	0.437917	0.5
Pb	3.3	31.3	0.489529	0.5
Se	3.3	31.3	0.489529	0.5

C

Name	spacing	cumm	frac	Occ
W	0	0	0	1.0
Se	1.6	1.6	0.025024	1.0
Se	3.4	5	0.0782	1.0
W	1.6	6.6	0.103223	1.0
Se	1.6	8.2	0.128247	1.0
Se	3.4	11.6	0.181423	1.0
W	1.6	13.2	0.206447	1.0
Se	1.6	14.8	0.231471	1.0
Pb	3.1	17.9	0.279954	0.5
Se	3.5	18.3	0.28621	0.5
Pb	3.2	21.5	0.336258	0.5
Se	3.4	21.3	0.33313	0.5
Pb	3.4	24.7	0.386306	0.5
Se	3.2	24.7	0.386306	0.5
Pb	3.3	28	0.437917	0.5
Se	3.3	28	0.437917	0.5
Pb	3.3	31.3	0.489529	0.5
Se	3.3	31.3	0.489529	0.5

D

Name	spacing	cumm	frac	Occ
W	0	0	0	1.0
Se	1.5	1.5	0.02346	1.0
Se	3.4	4.9	0.076636	1.0
W	1.5	6.4	0.100095	1.0
Se	1.5	7.9	0.123555	1.0
Se	3.4	11.3	0.176731	1.0
W	1.5	12.8	0.200191	1.0
Se	1.5	14.3	0.223651	1.0
Pb	3.2	17.5	0.273698	0.5
Se	3.4	17.7	0.276826	0.5
Pb	3.3	21	0.328438	0.5
Se	3.3	20.8	0.32531	0.5
Pb	3.3	24.1	0.376922	0.5
Se	3.3	24.3	0.38005	0.5
Pb	3.3	27.6	0.431661	0.5
Se	3.3	27.4	0.428533	0.5
Pb	3.3	30.7	0.480145	0.5
Se	3.3	30.9	0.483273	0.5

		E		
Name	**spacing**	**cumm**	**frac**	**Occ**
W	0	0	0	1.0
Se	1.5	1.5	0.02346	1.0
Se	3.4	4.9	0.076636	1.0
W	1.5	6.4	0.100095	1.0
Se	1.5	7.9	0.123555	1.0
Se	3.4	11.3	0.176731	1.0
W	1.5	12.8	0.200191	1.0
Se	1.5	14.3	0.223651	1.0
Pb	3.3	17.6	0.275262	0.5
Se	3.3	17.6	0.275262	0.5
Pb	3.3	20.9	0.326874	0.5
Se	3.3	20.9	0.326874	0.5
Pb	3.3	24.2	0.378486	0.5
Se	3.3	24.2	0.378486	0.5
Pb	3.3	27.5	0.430097	0.5
Se	3.3	27.5	0.430097	0.5
Pb	3.3	30.8	0.481709	0.5
Se	3.3	30.8	0.481709	0.5

		F		
Name	**spacing**	**cumm**	**frac**	**Occ**
W	0	0	0	1.0
Se	1.5	1.5	0.02346	1.0
Se	3.4	4.9	0.076636	1.0
W	1.5	6.4	0.100095	1.0
Se	1.5	7.9	0.123555	1.0
Se	3.4	11.3	0.176731	1.0
W	1.5	12.8	0.200191	1.0
Se	1.5	14.3	0.223651	1.0
Pb	3.1	17.4	0.272134	0.5
Se	3.5	17.8	0.27839	0.5
Pb	3.2	21	0.328438	0.5
Se	3.4	20.8	0.32531	0.5
Pb	3.4	24.2	0.378486	0.5
Se	3.2	24.2	0.378486	0.5
Pb	3.3	27.5	0.430097	0.5
Se	3.3	27.5	0.430097	0.5
Pb	3.3	30.8	0.481709	0.5
Se	3.3	30.8	0.481709	0.5

B.8: $[(PbSe)_{0.99}]_1[WSe_2]_2$ Refinement

A

Name	spacing	cumm	frac
Se	1.7	1.7	0.0886534
W	1.5	3.2	0.166877
Se	1.5	4.7	0.2451006
Pb	3.2	7.9	0.4119776
Se	3.2	7.9	0.4119776

B

Name	spacing	cumm	frac
Se	1.7	1.7	0.0886534
W	1.5	3.2	0.166877
Se	1.5	4.7	0.2451006
Pb	3.2	7.9	0.4119776
Se	3.4	8.1	0.4224074

C

Name	spacing	cumm	frac
Se	1.7	1.7	0.0886534
W	1.5	3.2	0.166877
Se	1.5	4.7	0.2451006
Pb	3	7.7	0.4015478
Se	3.6	8.3	0.4328372

D

Name	spacing	cumm	frac
Se	1.7	1.7	0.0886534
W	1.6	3.3	0.1720919
Se	1.6	4.9	0.2555304
Pb	3.2	8.1	0.4224074
Se	3.2	8.1	0.4224074

E

Name	spacing	cumm	frac
Se	1.7	1.7	0.0886534
W	1.6	3.3	0.1720919
Se	1.6	4.9	0.2555304
Pb	3.2	8.1	0.4224074
Se	3.4	8.3	0.4328372

F

Name	spacing	cumm	frac
Se	1.7	1.7	0.0886534
W	1.6	3.3	0.1720919
Se	1.6	4.9	0.2555304
Pb	3	7.9	0.4119776
Se	3.6	8.5	0.443267

1

Name	spacing	cumm	frac	occ
Se	1.7936276	1.7936276	0.093536	1
W	1.5651288	3.3587564	0.175156	1
Se	1.7110143	5.0697708	0.2643838	1
Pb	2.9713557	8.0411264	0.4193372	0.5
Se	2.9734178	8.0431886	0.4194447	0.5
Pb	0	0	0	0.05

2

Name	spacing	cumm	frac	occ
Se	1.7936276	1.7936276	0.093536	1
W	1.5651288	3.3587564	0.175156	1
Se	1.7110143	5.0697708	0.2643838	1
Pb	2.9713557	8.0411264	0.4193372	0.5
Se	2.9734178	8.0431886	0.4194447	0.5
Pb	0	0	0	0.1

3

Name	spacing	cumm	frac	occ
Se	1.7936276	1.7936276	0.093536	1
W	1.5651288	3.3587564	0.175156	1
Se	1.7110143	5.0697708	0.2643838	1
Pb	2.9713557	8.0411264	0.4193372	0.5
Se	2.9734178	8.0431886	0.4194447	0.5
Pb	0	0	0	0.2

4

Name	spacing	cumm	frac	occ
Se	1.7936276	1.7936276	0.093536	1
W	1.5651288	3.3587564	0.175156	1
Se	1.7110143	5.0697708	0.2643838	1
Pb	2.9713557	8.0411264	0.4193372	0.5
Se	2.9734178	8.0431886	0.4194447	0.5
Pb	0	0	0	0.3

5

Name	spacing	cumm	frac	occ
Se	1.7936276	1.7936276	0.093536	1
W	1.5651288	3.3587564	0.175156	1
Se	1.7110143	5.0697708	0.2643838	1
Pb	2.9713557	8.0411264	0.4193372	0.5
Se	2.9734178	8.0431886	0.4194447	0.5
Pb	0	0	0	0.4

6

Name	spacing	cumm	frac	occ
Se	1.7936276	1.7936276	0.093536	1
W	1.5651288	3.3587564	0.175156	1
Se	1.7110143	5.0697708	0.2643838	1
Pb	2.9713557	8.0411264	0.4193372	0.5
Se	2.9734178	8.0431886	0.4194447	0.5
Pb	0	0	0	0.5

7

Name	spacing	cumm	frac	occ
Se	1.7936276	1.7936276	0.093536	1
W	1.5651288	3.3587564	0.175156	1
Se	1.7110143	5.0697708	0.2643838	1
Pb	2.9713557	8.0411264	0.4193372	0.5
Se	2.9734178	8.0431886	0.4194447	0.5
W	0	0	0	0.05

8

Name	spacing	cumm	frac	occ
Se	1.7936276	1.7936276	0.093536	1
W	1.5651288	3.3587564	0.175156	1
Se	1.7110143	5.0697708	0.2643838	1
Pb	2.9713557	8.0411264	0.4193372	0.5
Se	2.9734178	8.0431886	0.4194447	0.5
W	0	0	0	0.1

9

Name	spacing	cumm	frac	occ
Se	1.7936276	1.7936276	0.093536	1
W	1.5651288	3.3587564	0.175156	1
Se	1.7110143	5.0697708	0.2643838	1
Pb	2.9713557	8.0411264	0.4193372	0.5
Se	2.9734178	8.0431886	0.4194447	0.5
W	0	0	0	0.2

10

Name	spacing	cumm	frac	occ
Se	1.7936276	1.7936276	0.093536	1
W	1.5651288	3.3587564	0.175156	1
Se	1.7110143	5.0697708	0.2643838	1
Pb	2.9713557	8.0411264	0.4193372	0.5
Se	2.9734178	8.0431886	0.4194447	0.5
W	0	0	0	0.3

11

Name	spacing	cumm	frac	occ
Se	1.7936276	1.7936276	0.093536	1
W	1.5651288	3.3587564	0.175156	1
Se	1.7110143	5.0697708	0.2643838	1
Pb	2.9713557	8.0411264	0.4193372	0.5
Se	2.9734178	8.0431886	0.4194447	0.5
W	0	0	0	0.4

12

Name	spacing	cumm	frac	occ
Se	1.7936276	1.7936276	0.093536	1
W	1.5651288	3.3587564	0.175156	1
Se	1.7110143	5.0697708	0.2643838	1
Pb	2.9713557	8.0411264	0.4193372	0.5
Se	2.9734178	8.0431886	0.4194447	0.5
W	0	0	0	0.5

B.9: $[(PbSe)_{0.99}]_2[WSe_2]_1$ Refinement

A

Name	spacing	cumm	Frac
W	0	0	0
Se	1.5	1.5	0.0796309
Pb	3.2	4.7	0.2495103
Se	3.4	4.9	0.2601277
Pb	3.2	8.1	0.4300071
Se	3.2	7.9	0.4193896

B

Name	spacing	cumm	Frac
W	0	0	0
Se	1.5	1.5	0.0796309
Pb	3.2	4.7	0.2495103
Se	3.2	4.7	0.2495103
Pb	3.2	7.9	0.4193896
Se	3.2	7.9	0.4193896

C

Name	spacing	cumm	frac
W	0	0	0
Se	1.5	1.5	0.0796309
Pb	3	4.5	0.2388928
Se	3.6	5.1	0.2707452
Pb	3.2	8.3	0.4406245
Se	3.2	7.7	0.4087721

D

Name	spacing	cumm	frac
W	0	0	0
Se	1.6	1.6	0.0849397
Pb	3.2	4.8	0.254819
Se	3.4	5	0.2654365
Pb	3.2	8.2	0.4353158
Se	3.2	8	0.4246983

E

Name	spacing	cumm	frac
W	0	0	0
Se	1.6	1.6	0.0849397
Pb	3.2	4.8	0.254819
Se	3.2	4.8	0.254819
Pb	3.2	8	0.4246983
Se	3.2	8	0.4246983

F

Name	spacing	cumm	frac
W	0	0	0
Se	1.6	1.6	0.0849397
Pb	3	4.6	0.2442015
Se	3.6	5.2	0.2760539
Pb	3.2	8.4	0.4459332
Se	3.2	7.8	0.4140809

REFERENCES CITED

Chapter I

1. Mackovicky, E.; Hyde, B. G. In *Incommensurate Sandwiched Layered Compounds*; Meerschaut, A., Ed.; Trans Tech Publications: Bern, Switzerland, **1992**; Vol. 100 & 101, p 18-100.

2. Rouxel, J.; Meerschaut, A. *Molecular Crystals and Liquid Crystals* **1994**, *244*, 343-354.

3. Reefman, D.; Baak, J.; Brom, H. B.; Wiegers, G. A. *Solid State Communications* **1990**, *75*, 47-51.

4. Gotoh, Y.; Onoda, M.; Akimoto, J.; Oosawa, Y. *Japanese Journal of Applied Physics* **1991**, *30*, L1039-L1041.

5. Roesky, R.; Meerschaut, A.; Rouxel, J.; Chen, J. *Zeitschrift fur anorganische und allgemeine Chemie* **1993**, *619*, 117-122.

6. Oosawa, Y.; Gotoh, Y.; Akimoto, J.; Tsunoda, T.; Sohma, M.; Onoda, M. *Japanese Journal of Applied Physics* **1992**, *31*, L 1096- L 1099.

7. Nader, A.; Briggs, A.; Gotoh, Y. *Solid State Communications* **1997**, *101*, 149-153.

8. Nader, A.; Lafond, A.; Briggs, A.; Meerschaut, A. *Physica Scripta* **1998**, *57*, 310-312.

9. Chiritescu, C.; Cahill, D. G.; Heideman, C.; Lin, Q.; Mortensen, C.; Nguyen, N. T.; Johnson, D.; Rostek, R.; Bottner, H. *Journal of Applied Physics* **2008**, *104*, 033533-033533-5.

10. Wiegers, G. A. *Progress in Solid State Chemistry* **1996**, *24*, 1-139.

11. Palewski, T. *Wiadomosci Chemiczne* **2003**, *57*, 827-854.

12. Wiegers, G. A.; Meerschaut, A. In *Incommensurate Sandwiched Layered Compounds*; Meerschaut, A., Ed.; Trans Tech Publications: Bern, Switzerland, **1992**; Vol. 100 &101, p 101-172.

13. Contera, S. A.; Yoshinobu, T.; Iwasaki, H.; Kisoda, K. *Surface Science* **1999**, *441*, 384-390.

14. Morales, J.; Santos, J.; Baas, J.; Wiegers, G. A.; Martinez, J. L. *Chemistry of Materials* **1999**, *11*, 2737-2742.

15. Meerschaut, A.; Deudon, C. *Materials Research Bulletin* **2001**, *36*, 1721-1727.

16. Brandt, J.; Kipp, L.; Skibowski, M.; Krasovskii, E. E.; Schattke, W.; Spiecker, E.; Dieker, C.; Jager, W. *Surface Science* **2003**, *532*, 705-710.

17. Gotoh, Y.; Onoda, M.; Akimoto, J.; Goto, M.; Oosawa, Y. *Japanese Journal of Applied Physics* **1992**, *31*, 3946-3950.

18. Wiegers, G. A.; Meetsma, A.; van Smaalen, S.; Haange, R. J.; Wulff, J.; Zeinstr, T.; de Boer, J. L.; Kuypers, S.; Van Tendeloo, G.; van Landuyt, J.; Amelinckx, S.; Meerschaut, A.; Rabu, P.; Rouxel, J. *Solid State Communications* **1989**, *70*, 409-413.

19. Wiegers, G. A.; Meetsma, A.; Haange, R. J.; van Smaalen, S.; De Boer, J. L.; Meerschaut, A.; Rabu, P.; Rouxel, J. *Acta Crystallographica, Section B: Structural Science* **1990**, *46*, 324-332.

20. Wiegers, G. A.; Zhou, W. Y. *Materials Research Bulliten* **1991**, *26*, 879-885.

21. Ren, Y.; Baas, J.; Meetsma, A.; de Boer, J. L.; Wiegers, G. A. *Acta Crystallographica, Section B: Structural Science* **1996**, *B52*, 398-405.

22. Meerschaut, A. *Current Opinion in Solid State & Materials Science* **1996**, *1*, 250-259.

23. Gardner, R. A.; Vlasse, M.; Wold, A. *Acta Crystallographica, Section B: Structural Science* **1969**, *25*, 781-786.

24. Suzuki, K.; Enoki, T.; Imaeda, K. *Solid State Communications* **1991**, *78*, 73-77.

25. Kuypers, S.; van Landuyt, J.; Amelinckx, S. *Journal of Solid State Chemistry* **1990**, *86*, 212-232.

26. Wiegers, G. A.; Haange, R. J. *European Journal of Solid State and Inorganic Chemistry* **1991**, *28*, 1071-1078.

27. Wiegers, G. A.; Meetsma, A.; Van Smaalen, S.; Haange, R. J.; De Boer, J. L. *Solid State Communications* **1990**, *75*, 689-92.

28. Wiegers, G. A.; Meetsma, A.; Haange, R. J.; de Boer, J. L. *Materials Research Bulliten* **1988**, *23*, 1551-1559.

29. Gotoh, Y.; Goto, M.; Kawaguchi, K.; Oosawa, Y.; Onoda, M. *Materials Research Bulliten* **1990**, *25*, 307-314.

30. Takahashi, T.; Osaka, S.; Yamada, O. *Journal of Physical Chemistry of Solids* **1973**, *34*, 1131.1135.

31. Gorochov, O.; McKinzie, H. *Journal of Solid State Chemistry* **1973**, *7*, 400-407.

32. Donohue, P. C. *Journal of Solid State Chemistry* **1975**, *12*, 80-83.

33. Guemas, L.; Rabu, P.; Meerschaut, A.; Rouxel, J. *Materials Research Bulliten* **1988**, *23*, 1064-1069.

34. Lelieveld, R.; Ijdo, W. *Acta Crystallographica, Section B: Structural Science* **1980**, *36*, 2223-2226.

35. Wiegers, G. A.; Meetsma, A.; De Boer, J. L.; Van Smaalen, S.; Haange, R. J. *Journal of Physics: Condensed Matter* **1991**, *3*, 2603-12.

36. Engelsman, F. M. R.; Wiegers, G. A.; Jellinek, F.; Laar, B. V. *Journal of Solid State Chemistry* **1973**, *6*, 574-582.

37. Lelieveld, R.; Ijdo, D. J. W. *Acta Crystallographica B: Structural Science* **1978**, *34*, 3348-3349.

38. Gressier, P.; Meerschaut, A.; Rouxel, J. *Materials Research Bulletin* **1987**, *22*, 1573-1580.

39. Oviedo, L. N. S.; Herrero, A. G.; Canovas, A. R. L. L.; Otero-Diaz, L. C. *Electron Microscopy 1998, Proceedings of the International Congress on Electron Microscopy, 14th, Cancun, Mex., Aug. 31-Sept. 4, 1998* **1998**, *3*, 59-60.

40. Oosawa, Y.; Gotoh, Y.; Onoda, M. *Chemistry Letters* 1989, 523-524.

41. Gotoh, Y.; Akimoto, J.; Sakurai, A.; Kiyozumi, Y.; Suzuki, K.; Oosawa, Y. *Chemistry Letters* **1990**, 2057-2060.

42. Wiegers, G. A.; Meetsma, A.; Haange, R. J.; de Boer, J. L. *Journal of Solid State Chemistry* **1990**, *89*, 328-339.

43. Lafond, A.; Nader, A.; Moeelo, Y.; Meerschaut, A.; Briggs, A.; Perrin, S.; Monceau, P.; Rouxel, J. *Journal of Alloys and Compounds* **1997**, *261*, 114-122.

44. Meetsma, A.; Wiegers, G. A.; Haange, R. J.; de Boer, J. L. *Acta Crystallographica* **1989**, *A*, 285-291.

45. Meerschaut, A.; Guemas, L.; Auriel, C.; Rouxel, J. *European Journal of Solid State and Inorganic Chemistry* **1990**, *27*, 557-570.

46. De Boer, J. L.; Meetsma, A.; Zeinstra, T. J.; Haange, R. J.; Wiegers, G. A. *Acta Crystallographica Section C: Crystal Structure Communications* **1991**, *47*, 924-930.

47. van Smaalen, S.; Meetsma, A.; Wiegers, G. A.; De Boer, J. L. *Acta Crystallographica B: Structural Science* **1991**, *47*, 314-325.

48. Onoda, M.; Kato, K. *Acta Crystallographica Section B: Structural Science* **1990**, *46*, 487-492.

49. Wulff, J.; Meetsma, A.; Haange, R. J.; De Boer, J. L.; Wiegers, G. A. *Synthetic Metals* **1990**, *39*, 1-12.

50. Ren, Y.; Meetsma, A.; Wiegers, G. A.; van Smaalen, S. *Acta Crystallographica, Section B: Structural Science* **1996**, *B52*, 389-397.

51. van Smaalen, S. *Incommensurate Crystallography*; Oxford University Press: Oxford, **2007**.

52. Kisoda, K.; Hangyo, M.; Nakashima, S.; Terashima, T.; Kojima, N. *Physica B: Condensed Matter (Amsterdam)* **1996**, *219&220*, 565-567.

53. Hangyo, M.; Kisoda, K.; Nakashima, S.; Meerschaut, A.; Rouxel, J. *Physica B: Condensed Matter (Amsterdam)* **1996**, *219&220*, 481-483.

54. Suzuki, K.; Enoki, T.; Tajima, H. *Physical Review B: Condensed Matter* **1995**, *52*, 16400-9.

55. Socabim *PDFMaint.*; Bruker AXS, **2001**; Vol. 7.0.108.4 Dongle.

56. Socabim *PDFMaint.*; Bruker AXS, **2001**; Vol. 7.0.108.4 Dongle.

57. Socabim *PDFMaint.*; Bruker AXS, **2001**; Vol. 7.0.108.4 Dongle.

58. Socabim *PDFMaint.*; Bruker AXS, **2001**; Vol. 7.0.108.4 Dongle.

59. Socabim *PDFMaint.*; Bruker AXS, **2001**; Vol. 7.0.108.4 Dongle.

60. Socabim *PDFMaint*; Bruker AXS, **2001**; Vol. 7.0.108.4 Dongle.

61. Socabim *PDFMaint.*; Bruker AXS, **2001**; Vol. 7.0.108.4 Dongle.

62. Socabim *PDFMaint.*; Bruker AXS, **2001**; Vol. 7.0.108.4 Dongle.

63. Socabim *PDFMaint.*; Bruker AXS, **2001**; Vol. 7.0.108.4 Dongle.

64. Socabim *PDFMaint.*; Bruker AXS, **2001**; Vol. 7.0.108.4 Dongle.

65. Socabim *PDFMaint.*; Bruker AXS, **2001**; Vol. 7.0.108.4 Dongle.

66. Socabim *PDFMaint.*; Bruker AXS, **2001**; Vol. 7.0.108.4 Dongle.

67. De Boer, J. L.; Meetsma, A.; Zeinstra, T. J.; Haange, R. J.; Wiegers, G. A. A*cta Crystallographica Section C: Crystal Structure Communications* **1991**, *47*, 924-930.
68. Meerschaut, A.; Auriel, C.; Rouxel, J. *Journal of Alloys and Compounds* **1992**, *183*, 129-37.

69. Auriel, C.; Meerschaut, A.; Rouxel, J. *Materials Research Bulletin* **1993**, *28*, 675-684.

70. Lafond, A.; Deudon, C.; Meerschaut, A.; Palvadeau, P.; Moelo, Y.; Briggs, A. *Journal of Solid State Chemistry* **1999**, *142*, 461-469.

71. Leynaud, O.; Lafond, A.; Moelo, Y.; Palvadeau, P.; Meerschaut, A. *Journal of Solid State Chemistry* **2002**, *168*, 41-51.

72. Moelo, Y.; Meerschaut, A.; Rouxel, J.; Auriel, C. *Chemistry of Materials* **1995**, *7*, 1759-1771.

73. Johnson, D. C.; Nguyen, N.; (University of Oregon, USA). Application: WO, **2007**, p 28 pp.

74. Lin, Q.; Smeller, M.; Heideman, C. L.; Zschack, P.; Koyano, M.; Anderson, M. D.; Kykyneshi, R.; Keszler, D. A.; Anderson, I. M.; Johnson, D. C. *Chemistry of Materials* **2010**, *22*, 1002-1009.

75. Harris, F. R.; Standridge, S.; Feik, C.; Johnson, D. C. *Angewandte de Chemie International Edition* **2003**, *42*, 5295-5299.

76. Chiritescu, C.; Cahill, D. G.; Nguyen, N.; Johnson, D.; Bodapati, A.; Keblinski, P.; Zschack, P. *Science* **2007**, *315*, 351-353.

77. Heideman, C., University of Oregon, **2010**.

78. Lin, Q., University of Oregon, **2009**.

Chapter II

1. Zschack, P.; Heideman, C.; Mortensen, C.; Nguyen, N.; Smeller, M.; Lin, Q.; Johnson, D. C. *Journal of Electronic Materials* **2009**, 38, 1402-1406.

2. Kaiser, D. L.; Watters Jr., R.; Commerce, D. o., Ed.; National Institute of Standards & Technology: **2010**.

3. Hammersly, A. P.; 12.012 ed.; ESRF: Grenoble, **2010**; Vol. 2010, p Technical reference Manual for FIT2D software.

4. Rietveld, H. M. *Acta Crystallographica* **1967**, *22*, 151-152.

5. Rietveld, H. M. *Journal of Allied Crystallography* **1969**, *2*, 65-71.

6. Larson, A. C.; Von Dreele, R. B.; Los Alamos National Laboratory Report: Los Alamos, **2004**, p 122.

7. Balzar, D.; Audebrand, N.; Daymond, M. R.; Fitch, A.; Hewat, A.; Langford, J. I.; Le Bail, A.; Louër, D.; Masson, O.; McCowan, C. N.; Popa, N. C.; Stephens, P. W.; Toby, B. H. *Journal of Allied Crystallography* **2004**, *37*, 911-924.

8. Toraya, H.; Hayashi, S.; Nakayasu, T. *Journal of Allied Crystallography* **1999**, *32*, 716-729.

9. Hill, R. J.; Cranswick, L. M. D. *Journal of Allied Crystallography* **1994**, *27*, 802-844.

10. Scarlett, N. V. Y.; Madsen, I. C.; Cranswick, L. M. D.; Lwin, T.; Groleau, E.; Stephenson, G.; Aylmor, M.; Agron-Olshina, N. *Journal of Allied Crystallography* **2002**, *35*, 383-400.

11. Madsen, I. C.; Scarlett, N. V. Y.; Cranswick, L. M. D.; Lwin, T. *Journal of Allied Crystallography* **2001**, *34*, 409-426.

12. Leon-Reina, L.; de la Torre, A. G.; Porras-Vazquez, J. M.; Cruz, L. M.; Ordonez, L. M.; Alcobe, X.; Gispert-Guirado, F.; Larranaga-Varga, A.; Paul, M.; Fuellmann, T.; Schmidt, R.; Aranda, M. A. G. *Journal of Allied Crystallography* **2009**, *42*, 906-916.

13. Gualteri, A.; Norby, P.; Hanson, J.; Hriljac, J. *Journal of Allied Crystallography* **1996**, *29*, 707-713.

14. McCusker, L. B.; Von Dreele, R. B.; Cox, D. E.; Louer, D.; Scardi, P. *Journal of Allied Crystallography* **1999**, *32*, 36-50.

15. Schwarzenbach, D.; Abrahams, S. C.; Flack, H. D.; Gonschorek, W.; Hahn, T.; Huml, K.; Marsh, R. E.; Prince, E.; Robertson, B. E.; Rollett, J. S.; Wilson, A. J. C. *Acta Crystallographica, Section A: Foundations of Crystallography* **1989**, *45*, 63-75.

16. Toby, B. In *Rietveld Refinement*; Toby, B., Ed.; Argonne National Labs: **2006**.

17. Larson, A. C.; von Dreele, R. B.; LAUR 86-748 ed.; Los Alamos National Labs: **2004**, p Rietveld refinement program suitable to simultaneous refinement. Contains alogrithms for neutron diffraction, x-ray diffraction, and synchrotron radiation.

18. Toby, B. H. *Journal of Allied Crystallography* **2001**, *34*, 210-213.

19. Toby, B. H.; Department of Energy: Argonne, IL, **2010**; Vol. 2010.

20. De Boer, J. L.; Meetsma, A.; Zeinstra, T. J.; Haange, R. J.; Wiegers, G. A. *Acta Crystallographica Section C: Crystal Structure Communications* **1991**, *47*, 924-930.

21. Gotoh, Y.; Onoda, M.; Akimoto, J.; Goto, M.; Oosawa, Y. *Japanese Journal of Applied Physics* **1992**, *31*, 3946-3950.

22. van Smaalen, S.; Meetsma, A.; Wiegers, G. A.; De Boer, J. L. *Acta Crystallographica B: Structural Science* **1991**, *47*, 314-325.

23. Wiegers, G. A.; Meetsma, A.; Haange, R. J.; van Smaalen, S.; De Boer, J. L.; Meerschaut, A.; Rabu, P.; Rouxel, J. *Acta Crystallographica, Section B: Structural Science* **1990**, *46*, 324-332.

24. Wiegers, G. A.; Meetsma, A.; van Smaalen, S.; Haange, R. J.; Wulff, J.; Zeinstr, T.; de Boer, J. L.; Kuypers, S.; Van Tendeloo, G.; van Landuyt, J.; Amelinckx, S.; Meerschaut, A.; Rabu, P.; Rouxel, J. *Solid State Communications* **1989**, *70*, 409-413.

25. Wiegers, G. A.; Zhou, W. Y. *Materials Research Bulliten* **1991**, *26*, 879-885.

26. Wiegers, G. A.; Meetsma, A.; De Boer, J. L.; Van Smaalen, S.; Haange, R. J. *Journal of Physics: Condensed Matter* **1991**, *3*, 2603-12.

27. Wiegers, G. A. *Progress in Solid State Chemistry* **1996**, *24*, 1-139.

28. Palewski, T. *Wiadomosci Chemiczne* **2003**, *57*, 827-854.

29. Brandt, J.; Kipp, L.; Skibowski, M.; Krasovskii, E. E.; Schattke, W.; Spiecker, E.; Dieker, C.; Jager, W. *Surface Science* **2003**, *532*, 705-710.

30. Kisoda, K.; Hangyo, M.; Nakashima, S.; Terashima, T.; Kojima, N. *Physica B: Condensed Matter (Amsterdam)* **1996**, *219&220*, 565-567.

31. Hangyo, M.; Kisoda, K.; Nakashima, S.; Meerschaut, A.; Rouxel, J. *Physica B: Condensed Matter (Amsterdam)* **1996**, *219&220*, 481-483.

32. Suzuki, K.; Enoki, T.; Tajima, H. *Physical Review B: Condensed Matter* **1995**, *52*, 16400-9.

33. De Boer, J. L.; Meetsma, A.; Zeinstra, T. J.; Haange, R. J.; Wiegers, G. A. *Acta Crystallographica Section C: Crystal Structure Communications* **1991**, *47*, 924-930.

34. Ohno, Y.; Yamaguchi, T. *Journal of Alloys and Compounds* **2008**, *455*, 10-16.

35. Evain, M.; Petricek, V.; Moelo, Y.; Maurel, C. *Acta crystallographica. Section B, Structural science* **2006**, *62*, 775-789.

36. Moelo, Y.; Meerschaut, A.; Rouxel, J.; Auriel, C. *Chemistry of Materials* **1995**, *7*, 1759-1771.

37. Larson, A. C.; von Dreele, R. B.; Los Alamos National Laboratory Report: Los Alamos, **2004**, p 167.

38. Durbin, J.; Watson, G. *Biometrica* **1951**, *38*, 159-179.

39. Hill, R. J.; Flack, H. D. *Journal of Allied Crystallography* **1987**, *20*, 356-361.

Chapter III

1. Wang, S.; Kuo, K. H. *Acta Crystallographica, Section A: Foundations of Crystallography* **1991**, *47*, 381-392.

2. Mackovicky, E.; Hyde, B. G. In *Incommensurate Sandwiched Layered Compounds*; Meerschaut, A., Ed.; Trans Tech Publications: Bern, Switzerland, **1992**; Vol. 100 & 101, p 18-100.

3. Kakos, G. A.; Turney, T. W.; Williams, T. B. *Journal of Solid State Chemistry* **1994**, *108*, 102-111.

4. Rouxel, J.; Moelo, Y.; Lafond, A.; Disalvo, F. J.; Meerschaut, A.; Roesky, R. *Inorganic Chemistry* **1994**, *33*, 3358-3363.

5. Ohno, Y.; Shimokawa, S. *Journal of Solid State Chemistry* **2004**, *177*, 2818-2826.

6. Ren, Y.; Baas, J.; Meetsma, A.; de Boer, J. L.; Wiegers, G. A. *Acta Crystallographica, Section B: Structural Science* **1996**, *B52*, 398-405.

7. Takahashi, T.; Osaka, S.; Yamada, O. *Journal of Physical Chemistry of Solids* **1973**, *34*, 1131.1135.

8. Gotoh, Y.; Onoda, M.; Akimoto, J.; Oosawa, Y. *Japanese Journal of Applied Physics* **1991**, *30*, L1039-L1041.

9. Guemas, L.; Rabu, P.; Meerschaut, A.; Rouxel, J. *Materials Research Bulliten* **1988**, *23*, 1064-1069.

10. Wegers, G. A.; Meetsma, A.; Haange, R. J.; de Boer, J. L. *Journal of Solid State Chemistry* **1990**, *89*, 328-339.

11. Wiegers, G. A.; Meetsma, A.; van Smaalen, S.; Haange, R. J.; Wulff, J.; Zeinstr, T.; de Boer, J. L.; Kuypers, S.; Van Tendeloo, G.; van Landuyt, J.; Amelinckx, S.; Meerschaut, A.; Rabu, P.; Rouxel, J. *Solid State Communications* **1989**, *70*, 409-413.

12. Wiegers, G. A.; Zhou, W. Y. *Materials Research Bulliten* **1991**, *26*, 879-885.

13. Wulff, J.; Meetsma, A.; van Smaalen, S.; Haange, R. J.; de Boer, J. L.; Wiegers, G. A. *Journal of Solid State Chemistry* **1990**, *84*, 118-129.

14. Rouxel, J.; Meerschaut, A. *Molecular Crystals and Liquid Crystals Science and Technology Section a-Molecular Crystals and Liquid Crystals* **1994**, *244*, 343-354.

15. Reefman, D.; Baak, J.; Brom, H. B.; Wiegers, G. A. *Solid State Communications* **1990**, *75*, 47-51.

16. Roesky, R.; Meerschaut, A.; Rouxel, J.; Chen, J. *Zeitschrift fur anorganische und allgemeine Chemie* **1993**, *619*, 117-122.

17. Oosawa, Y.; Gotoh, Y.; Akimoto, J.; Tsunoda, T.; Sohma, M.; Onoda, M. *Japanese Journal of Applied Physics* **1992**, *31*, L 1096- L 1099.

18. Oosawa, Y.; Gotoh, Y.; Akimoto, J.; Tsunoda, T.; Sohma, M.; Onoda, M. *Japanese Journal of Applied Physics* **1992**, *31*, L1096-L1099.

19. Chiritescu, C.; Cahill, D. G.; Heideman, C.; Lin, Q.; Mortensen, C.; Nguyen, N. T.; Johnson, D.; Rostek, R.; Bottner, H. *Journal of Applied Physics* **2008**, *104*, 033533-033533-5.

20. Nader, A.; Lafond, A.; Briggs, A.; Meerschaut, A. *Physica Scripta* **1998**, *57*, 310-312.

21. Nader, A.; Briggs, A.; Gotoh, Y. *Solid State Communications* **1997**, *101*, 149-153.

22. Brandt, J.; Kipp, L.; Skibowski, M.; Krasovskii, E. E.; Schattke, W.; Spiecker, E.; Dieker, C.; Jager, W. *Surface Science* **2003**, *532*, 705-710.

23. Kisoda, K.; Hangyo, M.; Nakashima, S.; Terashima, T.; Kojima, N. *Physica B: Condensed Matter (Amsterdam)* **1996**, *219&220*, 565-567.

24. Hangyo, M.; Kisoda, K.; Nakashima, S.; Meerschaut, A.; Rouxel, J. *Physica B: Condensed Matter (Amsterdam)* **1996**, *219&220*, 481-483.

25. Suzuki, K.; Enoki, T.; Tajima, H. *Physical Review B: Condensed Matter* **1995**, *52*, 16400-9.

26. De Boer, J. L.; Meetsma, A.; Zeinstra, T. J.; Haange, R. J.; Wiegers, G. A. *Acta Crystallographica Section C: Crystal Structure Communications* **1991**, *47*, 924-930.

27. Evain, M.; Petricek, V.; Moelo, Y.; Maurel, C. *Acta crystallographica. Section B, Structural science* **2006**, *62*, 775-789.

28. Ohno, Y.; Yamaguchi, T. *Journal of Alloys and Compounds* **2008**, *455*, 10-16.

29. Wiegers, G. A. *Progress in Solid State Chemistry* **1996**, *24*, 1-139.

30. De Boer, J. L.; Meetsma, A.; Zeinstra, T. J.; Haange, R. J.; Wiegers, G. A. *Acta Crystallographica Section C: Crystal Structure Communications* **1991**, *47*, 924-930.

31. Gotoh, Y.; Onoda, M.; Akimoto, J.; Goto, M.; Oosawa, Y. *Japanese Journal of Applied Physics* **1992**, *31*, 3946-3950.

32. van Smaalen, S.; Meetsma, A.; Wiegers, G. A.; De Boer, J. L. *Acta Crystallographica B: Structural Science* **1991**, *47*, 314-325.

33. Wiegers, G. A.; Meetsma, A.; De Boer, J. L.; Van Smaalen, S.; Haange, R. J. *Journal of Physics: Condensed Matter* **1991**, *3*, 2603-12.

34. Wiegers, G. A.; Meetsma, A.; Haange, R. J.; van Smaalen, S.; De Boer, J. L.; Meerschaut, A.; Rabu, P.; Rouxel, J. *Acta Crystallographica, Section B: Structural Science* **1990**, *46*, 324-332.

35. Wiegers, G. A.; Meetsma, A.; Van Smaalen, S.; Haange, R. J.; De Boer, J. L. *Solid State Communications* **1990**, *75*, 689-92.

36. Meerschaut, A.; Guemas, L.; Auriel, C.; Rouxel, J. *European Journal of Solid State and Inorganic Chemistry* **1990**, *27*, 557-570.

37. Gotoh, Y.; Goto, M.; Kawaguchi, K.; Oosawa, Y.; Onoda, M. *Materials Research Bulliten* **1990**, *25*, 307-314.

38. Wiegers, G. A. *Japanese Journal of Applied Physics, Part 1: Regular Papers, Short Notes & Review Papers* **1993**, *32*, 705-10.

39. Wiegers, G. A.; Haange, R. J. *European Journal of Solid State and Inorganic Chemistry* **1991**, *28*, 1071-1078.

40. Wiegers, G. A.; Meetsma, A.; Haange, R. J.; de Boer, J. L. *Materials Research Bulliten* **1988**, *23*, 1551-1559.

41. Wulff, J.; Meetsma, A.; Haange, R. J.; De Boer, J. L.; Wiegers, G. A. *Synthetic Metals* **1990**, *39*, 1-12.

42. Yarmoshenko, Y. M.; Trofimova, V. A.; Shamin, S. N.; Solovyev, I. V.; Kurmaev, E. Z.; Ettema, A. R. H. F.; Haas, C. *Journal of Physics: Condensed Matter* **1994**, *6*, 3993-8.

43. Meerschaut, A. *Current Opinion in Solid State & Materials Science* **1996**, *1*, 250-259.

44. Meerschaut, A.; Auriel, C.; Rouxel, J. *Journal of Alloys and Compounds* **1992**, *183*, 129-37.

45. Meerschaut, A.; Deudon, C. *Materials Research Bulletin* **2001**, *36*, 1721-1727.

46. Meerschaut, A.; Roesky, R.; Lafond, A.; Deudon, C.; Rouxel, J. *Journal of Alloys and Compounds* **1995**, *219*, 157-160.

47. Meetsma, A.; Wiegers, G. A.; Haange, R. J.; de Boer, J. L. *Acta Crystallographica Section A: Foundations of Crystallography* **1989**, *45*, 285-291.

48. Onoda, M.; Kato, K. *Acta Crystallographica Section B: Structural Science* **1990**, *46*, 487-492.

49. Lin, Q.; Heideman, C. L.; Nguyen, N.; Zschack, P.; Chiritescu, C.; Cahill, D. G.; Johnson, D. C. *European Journal of Inorganic Chemistry* **2008**, 2382-2385.

50. Chiritescu, C.; Cahill, D. G.; Nguyen, N.; Johnson, D.; Bodapati, A.; Keblinski, P.; Zschack, P. *Science* **2006**, *315*, 351-353.

51. Fister, L., Xiao-Mei Li, John McConnell, Thomas Novet, and David C. Johnson *Journal of Vacuum Science Technology A* **1993**, *11*, 3014-3019.

52. Yang, B.; Liu, J.; Wang, K.; Chen, G. *International Conference on Thermoelectrics* **2001**, *20th*, 344-347.

53. Larson, A. C.; von Dreele, R. B.; LAUR 86-748 ed.; Los Alamos National Labs: **2004**, p Rietveld refinement program suitable to simultaneous refinement. Contains alogrithms for neutron diffraction, x-ray diffraction, and synchrotron radiation.

54. Toby, B. H. *Journal of Allied Crystallography* **2001**, *34*, 210-213.

55. Moelo, Y.; Meerschaut, A.; Rouxel, J.; Auriel, C. *Chemistry of Materials* **1995**, *7*, 1759-1771.

56. Walck, S. D.; McCaffrey, J. P. *Thin Solid Films* **1997**, *Vol 308-309*, 399-405.

57. Rasband W.S., I. *National Institutes of Health, Bethesda, Maryland, USA, http://rsb.info.nih.gov/ij/,* **1997-2004**.

58. Thévenaz, P.; Ruttimann, U. E.; Unser, M. *IEEE Transactions on Image Processing*. **1998**, *vol. 7, no. 1*, 27-41.

59. Daams, J. L. C.; Villars, P.; van Vucht, J. H. N. *Atlas of Crystal Structure Types for Intermetallic Phases*; ASM International: Materials Park, OH, **1991**.

60. Socabim *PDF Maint.*; Bruker AXS, **2001**.

61. Schutte, W. J.; De Boer, J. L.; Jellinek, F. *Journal of Solid State Chemistry* **1987**, *70*, 207-209.

62. James, P. B.; Lavik, M. T. *Acta Crystallographica* **1963**, *16*, 1183.

63. Ufer, K.; Roth, G.; Kleeberg, r.; Stanjek, H.; Dohrmann, r.; Bergmann, J. *Zeitshcrift fur Kristallographie* **2004**, *219*, 519-527.

Chapter IV

1. Fauchais, P.; Montavon, G.; Lima, R. S.; Marple, B. R. *Journal of Physics: D Applied Physics* **2011**, *44*, 093001-0930054.

2. Robertson, J. *Applied Surface Science* **2002**, *190*, 2-10.

3. Bottner, H. *Thermoelectrics, 2005. ICT 2005. 24th International Conference on Thermoelectrics* **2005**.

4. Venkatasubramanian, R. *Physical Review B: Condensed Matter* **2000**, *61*, 3091-3097.

5. Shakouri, A.; Bowers, J. E. *Applied Physics Letters* **1997**, *71*, 1234-1236.

6. Wiegers, G. A. *Progress in Solid State Chemistry* **1996**, *24*, 1-139.

7. Palewski, T. *Wiadomosci Chemiczne* **2003**, *57*, 827-854.
8. Wiegers, G. A.; Meerschaut, A. In *Incommensurate Sandwiched Layered Compounds*; Meerschaut, A., Ed.; Trans Tech Publications: Bern, Switzerland, 1992; Vol. 100 &101, p 101-172.

9. Morales, J.; Santos, J.; Baas, J.; Wiegers, G. A.; Martinez, J. L. *Chemistry of Materials* **1999**, *11*, 2737-2742.

10. Nader, A.; Lafond, A.; Briggs, A.; Meerschaut, A. *Physica Scripta* **1998**, *57*, 310-312.

11. Lafond, A.; Nader, A.; Moeelo, Y.; Meerschaut, A.; Briggs, A.; Perrin, S.; Monceau, P.; Rouxel, J. *Journal of Alloys and Compounds* **1997**, *261*, 114-122.

12. Rouxel, J.; Meerschaut, A.; Wiegers, G. A. *Journal of Alloys and Compounds* **1995**, *229*, 144-57.

13. Leynaud, O.; Lafond, A.; Moelo, Y.; Palvadeau, P.; Meerschaut, A. *Journal of Solid State Chemistry* **2002**, *168*, 41-51.

14. Lin, Q.; Smeller, M.; Heideman, C. L.; Zschack, P.; Koyano, M.; Anderson, M. D.; Kykyneshi, R.; Keszler, D. A.; Anderson, I. M.; Johnson, D. C. *Chemistry of Materials* **2010**, *22*, 1002-1009.

15. Chiritescu, C.; Cahill, D. G.; Heideman, C.; Lin, Q.; Mortensen, C.; Nguyen, N. T.; Johnson, D.; Rostek, R.; Bottner, H. *Journal of Applied Physics* **2008**, *104*, 033533-033533-5.

16. De Boer, J. L.; Meetsma, A.; Zeinstra, T. J.; Haange, R. J.; Wiegers, G. A. *Acta Crystallographica Section C: Crystal Structure Communications* **1991**, *47*, 924-930.

17. Gotoh, Y.; Onoda, M.; Akimoto, J.; Goto, M.; Oosawa, Y. *Japanese Journal of Applied Physics* **1992**, *31*, 3946-3950.

18. van Smaalen, S.; Meetsma, A.; Wiegers, G. A.; De Boer, J. L. *Acta Crystallographica B: Structural Science* **1991**, *47*, 314-325.

19. Wiegers, G. A.; Haange, R. J. *European Journal of Solid State and Inorganic Chemistry* **1991**, *28*, 1071-1078.

20. Wiegers, G. A.; Meetsma, A.; Haange, R. J.; van Smaalen, S.; De Boer, J. L.; Meerschaut, A.; Rabu, P.; Rouxel, J. *Acta Crystallographica, Section B: Structural Science* **1990**, *46*, 324-332.

21. Wiegers, G. A.; Meetsma, A.; van Smaalen, S.; Haange, R. J.; Wulff, J.; Zeinstr, T.; de Boer, J. L.; Kuypers, S.; Van Tendeloo, G.; van Landuyt, J.; Amelinckx, S.; Meerschaut, A.; Rabu, P.; Rouxel, J. *Solid State Communications* **1989**, *70*, 409-413.

22. Wiegers, G. A.; Zhou, W. Y. *Materials Research Bulliten* **1991**, *26*, 879-885.

23. Lin, Q.; Heideman, C.; Nguyen, N.; Zschack, P.; Chiritescu, C.; Cahill, D. G.; Johnson, D. *European Journal of Inorganic Chemistry* **2008**, *2008*, 2382-2385.

24. Heideman, C., University of Oregon, **2010**.

25. Lin, Q., University of Oregon, **2009**.

26. Heideman, C.; Nyugen, N.; Hanni, J.; Lin, Q.; Duncombe, S.; Johnson, D. C.; Zschack, P. *Journal of Solid State Chemistry* **2008**, *181*, 1701-1706.

27. Zschack, P.; Heideman, C.; Mortensen, C.; Nguyen, N.; Smeller, M.; Lin, Q.; Johnson, D. C. *Journal of Electronic Materials* **2009**, *38*, 1402-1406.

28. Toby, B. H. *Journal of Allied Crystallography* **2001**, *34*, 210-213.

29. Larson, A. C.; von Dreele, R. B.; LAUR 86-748 ed.; Los Alamos National Labs: **2004**, p Rietveld refinement program suitable to simultaneous refinement.

Contains alogrithms for neutron diffraction, x-ray diffraction, and synchrotron radiation.

30. Toby, B. In *Rietveld Refinement*; Toby, B., Ed.; Argonne National Labs: **2006**.

31. Socabim *PDF Maint.*; Bruker AXS, **2001**; Vol. 7.0.108.4 Dongle.

32. Socabim *PDF Maint.*; Bruker AXS, **2001**; Vol. 7.0.108.4 Dongle.

33. De Boer, J. L.; Meetsma, A.; Zeinstra, T. J.; Haange, R. J.; Wiegers, G. A. *Acta Crystallographica Section C: Crystal Structure Communications* **1991**, *47*, 924-930.

34. Wiegers, G. A.; Meetsma, A.; De Boer, J. L.; Van Smaalen, S.; Haange, R. J. *Journal of Physics: Condensed Matter* **1991**, *3*, 2603-12.

35. Brandt, J.; Kipp, L.; Skibowski, M.; Krasovskii, E. E.; Schattke, W.; Spiecker, E.; Dieker, C.; Jager, W. *Surface Science* **2003**, *532*, 705-710.

36. Kisoda, K.; Hangyo, M.; Nakashima, S.; Terashima, T.; Kojima, N. *Physica B: Condensed Matter (Amsterdam)* **1996**, *219&220*, 565-567.

37. Hangyo, M.; Kisoda, K.; Nakashima, S.; Meerschaut, A.; Rouxel, J. *Physica B: Condensed Matter (Amsterdam)* **1996**, *219&220*, 481-483.

38. Suzuki, K.; Enoki, T.; Tajima, H. *Physical Review B: Condensed Matter* **1995**, *52*, 16400-16409.

39. Ohno, Y.; Yamaguchi, T. *Journal of Alloys and Compounds* **2008**, *455*, 10-16.

40. Evain, M.; Petricek, V.; Moelo, Y.; Maurel, C. *Acta crystallographica. Section B, Structural science* **2006**, *62*, 775-789.

41. Oosawa, Y.; Gotoh, Y.; Akimoto, J.; Tsunoda, T.; Sohma, M.; Onoda, M. *Japanese Journal of Applied Physics* **1992**, *31*, L 1096- L 1099.

42. Ren, Y.; Meetsma, A.; Wiegers, G. A.; van Smaalen, S. *Acta Crystallographica, Section B: Structural Science* **1996**, *B52*, 389-397.

43. Hill, R. J.; Cranswick, L. M. D. *Journal of Allied Crystallography* **1994**, *27*, 802-844.

44. Socabim *PDFMaint.*; Bruker AXS, **2001**; Vol. 7.0.108.4 Dongle.

45. Wiegers, G. A.; Meetsma, A.; Van Smaalen, S.; Haange, R. J.; De Boer, J. L. *Solid State Communications* **1990**, *75*, 689-92.

46. Socabim *PDFMaint.*; Bruker AXS, **2001**; Vol. 7.0.108.4 Dongle.

47. Suzuki, K.; Enoki, T.; Imaeda, K. *Solid State Communications* **1991**, *78*, 73-77.

48. Socabim *PDFMaint.*; Bruker AXS, **2001**; Vol. 7.0.108.4 Dongle.

49. Socabim *PDFMaint.*; Bruker AXS, **2001**; Vol. 7.0.108.4 Dongle.

50. Socabim *PDFMaint*; Bruker AXS, **2001**; Vol. 7.0.108.4 Dongle.

51. Onoda, M.; Kato, K. *Acta Crystallographica Section B: Structural Science* **1990**, *46*, 487-492.

52. Socabim *PDFMaint.*; Bruker AXS, **2001**; Vol. 7.0.108.4 Dongle.

53. Kuypers, S.; van Landuyt, J.; Amelinckx, S. *Journal of Solid State Chemistry* **1990**, *86*, 212-232.

54. Harris, F. R. Journal Style, University of Oregon, **2004**.

Chapter V

1. El-Sayed, M. A. *Accounts of Chemical Research* **2004**, *37*, 326-333.

2. Sapra, S.; Nanda, J.; Sarma, D. D. *Electronic Structure of Semiconductor Nanoparticles* **2004**, *3*, 181-192.

3. Rao, C.; Kulkarni, G.; Thomas, P.; Edwards, P. *Chemistry* **2002**, *8*, 28-35.

4. Sun, Y.; Xia, Y. *Science* **2002**, *298*, 2176-2179.

5. Mao, Y.; Park, T.-J.; Wong, S. S. *Chemical Communications* **2005**, *46*, 5721-5735.

6. Yacamán, M. J.; Ascencio, J. A.; Liu, H. B.; Gardea-Torresdey, J. *Journal of Vacuum Science & Technology B: Microelectronics and Nanometer Structures* **2001**, *19*, 1091-1104.

7. Yu, W. W.; Andrew Wang, Y.; Peng, X. *Chemistry of Materials* **2003**, *15*, 4300–4308.

8. Puntes, V. F.; Krishnan, K. M.; Alivisatos, P. A. *Science* **2001**, *291*, 2115-2117

9. Murray, C. B.; Kagan, C. R.; Bawendi, M. G. *Science* **1995**, *270*, 1335-1337.

10. Murray, C. B.; Kagan, C. R.; Bawendi, M. G. *Annual Review of Materials Science* **2000**, *30*, 545-610.

11. Shevchenko, E. V.; Talapin, D. V.; Kotov, N. A.; O'Brien, S.; Murray, C. B. *Nature* **2006**, *439*, 55-59.

12. Sun, S.; Murray, C. B.; Weller, D.; Folks, L.; Moser, A. *Science* **2000**, *287*, 1989-1992

13. Talapin, D. V.; Shevchenko, E. V.; Bodnarchuk, M. I.; Ye, X.; Chen, J.; Murray, C. B. *Nature* **2009**, *461*, 964-967.

14. Chen, J.; Ye, X.; Murray, C. B. *ACS Nano* **2010**, *4*, 2374-2381.

15. Brown, L. O.; Hutchison, J. E. *Journal of Physical Chemistry B* **2001**, *105*, 8911-8916.

16. Billinge, S. J. L.; Levin, I. *Science* **2007**, *316*, 561-565

17. Rogach, A. L.; Talapin, D. V.; Shevchenko, E. V.; Kornowski, A.; Haase, M.; Weller, H. *Advanced Functional Materials* **2002**, *12*, 653-664.

18. Lin, Q.; Smeller, M.; Heideman, C.; Zschack, P.; Koyano, M.; Anderson, M. D.; Kykyneshi, R.; Keszler, D.; Anderson, I. M.; Johnson, D. C. *Chemistry of Materials* **2010**, *22*, 1002-1009.

19. Heideman, C.; Nyugen, N.; Hanni, J.; Lin, Q.; Duncombe, S.; Johnson, D. C.; Zschack, P. *Journal of Solid State Chemistry* **2008**, *181*, 1701-1776.

20. Wiegers, G. A. *Progress in Solid State Chemistry* **1996**, *24*, 1-139.

Chapter VI

1. Wiegers, G. A. *Progress in Solid State Chemistry* **1996**, *24*, 1-139.

2. Palewski, T. *Wiadomosci Chemiczne* **2003**, *57*, 827-854.

3. Brandt, J.; Kipp, L.; Skibowski, M.; Krasovskii, E. E.; Schattke, W.; Spiecker, E.; Dieker, C.; Jager, W. *Surface Science* **2003**, *532*, 705-710.

4. Kisoda, K.; Hangyo, M.; Nakashima, S.; Terashima, T.; Kojima, N. *Physica B: Condensed Matter (Amsterdam)* **1996**, *219&220*, 565-567.

5. Hangyo, M.; Kisoda, K.; Nakashima, S.; Meerschaut, A.; Rouxel, J. *Physica B: Condensed Matter (Amsterdam)* **1996**, *219&220*, 481-483.

6. Suzuki, K.; Enoki, T.; Tajima, H. *Physical Review B: Condensed Matter* **1995**, *52*, 16400-9.

7. De Boer, J. L.; Meetsma, A.; Zeinstra, T. J.; Haange, R. J.; Wiegers, G. A. *Acta Crystallographica Section C: Crystal Structure Communications* **1991**, *47*, 924-930.

8. Ohno, Y.; Yamaguchi, T. *Journal of Alloys and Compounds* **2008**, *455*, 10-16.

9. Evain, M.; Petricek, V.; Moelo, Y.; Maurel, C. *Acta crystallographica. Section B, Structural science* **2006**, *62*, 775-789.

10. Moelo, Y.; Meerschaut, A.; Rouxel, J.; Auriel, C. *Chemistry of Materials* **1995**, *7*, 1759-1771.

11. Ettema, A. R. H. F.; Haas, C. *Journal of Physics: Condensed Matter* **1993**, *5*, 3817.

12. van Smaalen, S. *Acta Crystallographica, Section A: Foundations of Crystallography* **1992**, *48*, 408.

13. Ohno, Y.; Shimokawa, S. *Journal of Solid State Chemistry* **2004**, *177*, 2818-2826.

14. Sourisseau, C.; Cavagnat, R.; Fouassier, M.; Tirado, J. L.; Morales, J. *Journal of Molecular Structure* **1995**, *348*, 107-110.

15. Murugesan, T.; Ramesh, S.; Gopalakrishnan, J.; Rao, C. N. R. *Journal of Solid State Chemistry* **1981**, *36*, 165-172.

16. Fister, L., Xiao-Mei Li, John McConnell, Thomas Novet, and David C. Johnson *Journal of Vacuum Science Technology A* **1993**, *11*, 3014-3019.

17. Yang, B.; Liu, J.; Wang, K.; Chen, G. *International Conference on Thermoelectrics* **2001**, *20th*, 344-347.

18. Larson, A. C.; von Dreele, R. B.; LAUR 86-748 ed.; Los Alamos National Labs: **2004**, p Rietveld refinement program suitable to simultaneous refinement. Contains alogrithms for neutron diffraction, x-ray diffraction, and synchrotron radiation.

19. Toby, B. H. *Journal of Allied Crystallography* **2001**, *34*, 210-213.

20. Meerschaut, A.; Guemas, L.; Auriel, C.; Rouxel, J. *European Journal of Solid State and Inorganic Chemistry* **1990**, *27*, 557-570.

21. Roesky, R.; Meerschaut, A.; Rouxel, J.; Chen, J. *Zeitschrift fur anorganische und allgemeine Chemie* **1993**, *619*, 117-122.

22. Meerschaut, A.; Auriel, C.; Rouxel, J. *Journal of Alloys and Compounds* **1992**, *183*, 129-37.

23. Hernan, L.; Morales, J.; Santos, J.; Espinos, J. P.; Gonzalez-Elipe, A. R. *Journal of Materials Chemistry* **1998**, *8*, 2281-2286.

24. Ren, Y.; Meetsma, A.; Wiegers, G. A.; van Smaalen, S. *Acta Crystallographica, Section B: Structural Science* **1996**, *B52*, 389-397.

25. Bengel, H.; Jobic, S.; Moelo, Y.; Lafond, A.; Rouxel, J.; Seo, D. K.; Whangbo, M. H. *Journal of Solid State Chemistry* **2000**, *149*, 370-377.